High-order numerical methods for laser plasma modeling.

Jan Velechovsky

To cite this version:

Jan Velechovsky. High-order numerical methods for laser plasma modeling.. Astrophysics [astro-ph]. Université de Bordeaux; České vysoké učení technické (Prague), 2015. English. NNT : 2015BORD0098 . tel-01247677

HAL Id: tel-01247677

https://theses.hal.science/tel-01247677

Submitted on 4 Jan 2016

THÈSE EN COTUTELLE PRÉSENTÉE

POUR OBTENIR LE GRADE DE

DOCTEUR DE

L'UNIVERSITÉ DE BORDEAUX

ET DE L'UNIVERSITÉ TECHNIQUE TCHÈQUE

ÉCOLE DOCTORALE DES SCIENCES PHYSIQUES ET DE L'INGÉNIEUR

FACULTÉ DES SCIENCES NUCLÉAIRES ET DE GÉNIE PHYSIQUE

SPÉCIALITÉ ASTROPHYSIQUE, PLASMAS, NOYAUX

Par Jan VELECHOVSKÝ

HIGH–ORDER NUMERICAL METHODS FOR LASER PLASMA MODELING

Sous la direction de Vladimir TIKHONCHUK
et de Richard LISKA

Soutenue le 29. 6. 2015

Membres du jury :

M. RICHTER, Ivan	As. prof., Czech Tech. University	Président
M. BENEŠ, Michal	Prof., Czech Tech. University	Examinateur
M. BONNAUD, Guy	Prof., CEA	Examinateur
Mme BULGAKOVA, Nadezhda	Prof., HiLASE Czech Acad. Sci.	Examinateur
M. DRŠKA, Ladislav	Prof., Czech Tech. University	Examinateur
M. MAIRE, Pierre-Henri	Research Engineer, As. prof., CEA	Examinateur
M. NKONGA, Boniface	Prof., Univ. of Nice Sophia-Antipolis	Rapporteur
M. WEBER, Stefan	Doctor, ELI-Beamlines CAS	Rapporteur

Titre : MÉTHODES NUMÉRIQUES D'ORDRE ÉLEVÉ POUR LA MODÉLISATION DE PLASMA LASER

Résumé : Cette thèse présente le développement d’une méthode ALE pour la modélisation de l’interaction laser–plasma. La particularité de cette méthode est l’utilisation d’une étape de projection d’ordre élevé. Cette étape de projection consiste en une interpolation conservative des quantités conservatives du maillage Lagrangien sur un maillage régularisé. Afin d’éviter les oscillations numériques non-physiques, les flux numériques d’ordre élevé sont combinés avec des flux numériques d’ordre moins élevé. Ces flux numériques sont obtenu en considérant les quantités conservatives constantes par morceaux. Cette méthode pour la discrétisation cellule–centrée consiste à préserver les maximums locaux pour la densité, la vitesse et l’énergie interne. Aspects particuliers de la méthode sont appliquées pour la projection la quantité de mouvement pour la discrétisation ’staggered’. Nous l’utilisons ici dans le cadre de la projection sous la forme de la méthode Flux Correction Remapping (FCR). Dans cette thèse le volet applicatif concerne la modélisation de l’interaction d’un laser énergétique avec de plasma et des matériaux microstructures. Un intérêt particulier est porté à la modélisation de l’absorption du laser par une mousse de faible densité. L’absorption se fait à deux échelles spatiales simultanément. Ce modèle d’absorption laser à deux échelles est mis en œuvre dans le code PALE hydrodynamique. Les simulations numériques de la vitesse de pénétration du laser dans une mousse à faible densité sont en bon accord avec les données expérimentales.

Mots clés : laser-plasma, d'ordre élevé, ALE, absorption laser

---

Title : HIGH–ORDER NUMERICAL METHODS FOR LASER PLASMA MODELING

Abstract : This thesis presents the overview and the original contributions to a high–order Arbitrary Lagrangian–Eulerian (ALE) method applicable for the laser–generated plasma modeling with the focus to a remapping step of the ALE method. The remap is the conservative interpolation of the conservative quantities from a low–quality Lagrangian grid onto a better, smoothed one. To avoid non–physical numerical oscillations, the high–order numerical fluxes of the reconstruction are combined with the low–order (first–order) numerical fluxes produced by a standard donor remapping method. The proposed method for a cell–centered discretization preserves bounds for the density, velocity and specific internal energy by its construction. Particular symmetry–preserving aspects of the method are applied for a staggered momentum remap. The application part of the thesis is devoted to the laser radiation absorption modeling in plasmas and microstructures materials with the particular interest in the laser absorption in low–density foams. The absorption is modeled on two spatial scales simultaneously. This two–scale laser absorption model is implemented in the hydrodynamic code PALE. The numerical simulations of the velocity of laser penetration in a low–density foam are in a good agreement with the experimental data.

Keywords : laser plasma, high–order, ALE, laser absorption

Unité de recherche

Centre Lasers Intenses et Applications (UMR5107)

351, Cours de la Liberation, 33405 Talence cedex

Acknowledgements

At the first place, I would like to thank my advisers: Richard Liska for patient leading and many relevant suggestions and remarks, Vladimir Tikhonchuk for his comments concerning all viewpoints of the presented topic, Jérôme Breil for careful guiding and advices related to numerical methods and Jiří Limpouch for discussions of physics–related issues and many useful comments.

A substantial part of the presented work was done in collaboration with colleagues from Centre Lasers Intenses et Applications (CELIA) and the Los Alamos National Laboratory (LANL). Philippe Nicolai and Sergey Guskov from CELIA deserve my gratitude for discussions and comments concerning the laser propagation in microstructured targets. Special thanks belong to Mikhail Shashkov for his care, advices and presentation of challenging topics during my internship in LANL. I thank Milan Kuchařík for a particular numerical simulation in his staggered code as well as for his useful remarks and comments. I thank the CHLER's developers team in CELIA for providing me access to their cell–centered code. In addition to joint projects with these people, several scientific results have been achieved together with Pavel Váchal and Oldřich Renner.

I appreciate the goodwill of Czech Technical University in Prague, University of Bordeaux, Los Alamos National Laboratory, and the French Embassy in Czech Republic for providing me the necessary support during my study and research.

This research has been conducted during the years 2011 – 2015 and supported in parts by the Czech Technical University grants SGS10/299/OHK4/3T/14 and SGS13/220/OHK4/3T/14, the Czech Science Foundation projects P205/10/0814, P201/12/P554 and 14-21318S, Czech Ministry of Education grants MSM 684077002, and RVO: 68407700.

Parts of this work was performed under the auspices of the National Nuclear Security Administration of the US Department of Energy at Los Alamos National Laboratory under Contract No. DE-AC52-06NA25396. This work has been carried out within the framework of the EUROfusion Consortium and has received funding from the European Union's Horizon 2020 research and innovation programme under grant agreement number 633053.

Abstract

This thesis presents the overview and the original contributions to a high–order Arbitrary Lagrangian–Eulerian (ALE) method applicable for the laser–generated plasma modeling with the focus to a remapping step of the ALE method. The remap is the conservative interpolation of the conservative quantities from a low–quality Lagrangian grid onto a better, smoothed one. For the investigated Euler equations for the inviscid compressible fluid flow, these quantities are the mass, momentum components and the total energy. High–order accuracy remap is achieved thanks to the piecewise quadratic reconstruction of the volume densities of the conservative quantities over a computational mesh. To avoid non–physical numerical oscillations, the high–order numerical fluxes of the reconstruction are combined with the low–order (first–order) numerical fluxes produced by a standard donor remapping method. This combination is inspired by the Flux Corrected Transport (FCT) method. The proposed method for a cell–centered discretization preserves bounds for the density, velocity and specific internal energy by its construction. Particular symmetry–preserving aspects of the method are applied for a staggered momentum remap.

The application part of the thesis is devoted to the laser radiation absorption modeling in plasmas and microstructures materials with the particular interest in the laser absorption in low–density foams. The absorption is modeled on two spatial scales simultaneously. The microscale information about the local expansion of a thin solid layer in one spatial dimension is used to obtain the average propagation speed of the homogenization front in the macroscale hydrodynamic simulations. This two–scale laser absorption model is implemented in the hydrodynamic code PALE. The numerical simulations of the velocity of laser penetration in a low–density foam are in a good agreement with the experimental data.

Abstrakt

Tato práce představuje popis a původní příspěvky k Lagrangeovsko–Eulerovské (ALE) metodě vysokého řádu přesnosti aplikovatelné na hydrodynamické simulace laserem generovaného plasmatu se zaměřením na jednu část této metody, nazývanou remapování. Remapování je speciální případ interpolace, která je konzervativní, tj. zachovává celkové množství zachovávajících se veličin při jejich interpolaci z nekvalitní Lagrangeovské výpočetní sítě na lepší, vyhlazenou síť. Těmito veličinami jsou hmota, složky hybnosti a celková energie pro zkoumaný systém hydrodynamických Eulerových rovnic popisujících nevazkou stlačitelnou tekutinu. Vysokého řádu přesnosti remapování je dosaženo použitím po částech kvadratické rekonstrukce objemových hustot těchto zachovávajících se veličin v buňkách výpočetní sítě. Abychom předešli vzniku nefyzikálních numerických oscilací, kombinujeme numerické toky vysokého řádu přesnosti s toky nízkého řádu danými standardní remapovací metodou používající po částech konstantní rekonstrukci. Tato kombinace je inspirována metodou transportu opravou toků (FCT). Navrhovaná metoda pro tzv. „cell–centered“ diskretizaci v buňkách díky své konstrukci zachovává meze v hustotě, rychlosti a specifické vnitřní energii. Dílčí části této metody, zodpovědné za zachování symetrie, jsou použity pro remapování hybnosti při tzv. „staggered“ diskretizaci.

Část práce věnovaná aplikacím zasvěcuje do modelování absorpce laserového záření v plasmatu a materiálech se speciální mikrostrukturou se zvláštním zaměřením na absorpci laseru v řídkých pěnách. Tato absorpce je modelována současně pro dvě prostorová přiblížení. Mikroskopická informace o lokální expanzi slabých pevných vrstev uvažované v jednom prostorovém rozměru je použita k získání průměrné rychlosti postupu homogenizačního čela v hydrodynamických simulacích pěny jako celku. Tento dvouúrovňový model absorpce laseru je implementován do hydrodynamického kódu PALE. Numerické simulace rychlosti prostupu laseru řídkou pěnou jsou ve shodě s experimentálně měřenými daty.

Résumé

Cette thèse présente le développement d'une méthode ALE pour la modélisation de l'interaction laser–plasma. La particularité de cette méthode est l'utilisation d'une étape de projection d'ordre élevé. Cette étape de projection consiste en une interpolation conservative des quantités conservatives du maillage Lagrangien sur un maillage régularisé. Pour les équations d'Euler les quantités conservatives que l'on doit projeter sont la masse, la quantité de mouvement et l'énergie totale. La reconstruction d'ordre élevé est obtenu par une reconstruction quadratique par morceaux des quantités conservatives volumiques sur la grille de calcul. Afin d'éviter les oscillations numériques non-physiques, les flux numériques d'ordre élevé sont combinés avec des flux numériques d'ordre moins élevé. Ces flux numériques sont obtenu en considérant les quantités conservatives constantes par morceaux. Cette combinaison de flux est inspiré par la méthode Flux Correction Transport (FCT). Cette méthode pour la discrétisation cellule–centrée consiste à préserver les maximums locaux pour la densité, la vitesse et l'énergie interne. Aspects particuliers de la méthode sont appliquées pour la projection la quantité de mouvement pour la discrétisation 'staggered'. Nous l'utilisons ici dans le cadre de la projection sous la forme de la méthode Flux Correction Remapping (FCR).

Dans cette thèse le volet applicatif concerne la modélisation de l'interaction d'un laser énergétique avec de plasma et des matériaux microstructures. Un intérêt particulier est porté à la modélisation de l'absorption du laser par une mousse de faible densité. L'absorption se fait à deux échelles spatiales simultanément, l'expansion locale d'une couche solide mince dans une dimension de l'espace est utilisé pour fournir une vitesse moyenne homogénéisée qui permet la modélisation hydrodynamique macroscopique. Ce modèle d'absorption laser à deux échelles est mis en œuvre dans le code PALE hydrodynamique. Les simulations numériques de la vitesse de pénétration du laser dans une mousse à faible densité sont en bon accord avec les données expérimentales.

Contents

1. Introduction

Numerical methods, i.e. the procedures for solving mathematical problem in general, are successfully used for thousands of years. Probably the oldest known evidence of them is the Babylonian table showing an algorithm to calculate the square root of the number two [1]. Common numerical methods, which are taught at technical universities, are dated to the period from 17th to 19th century, the period of growth of the classical mechanics. Their names, e.g. the Newton method, Lagrange polynomial, Gaussian elimination or Euler method, are the clear evidence of that. However, the biggest development of the numerical methods started in 1940s, when the first computers became available. Incredibly fast and free–of–mistakes computers replaced the non–effective human factor in the procedures. The work of people was transferred from the execution to the development of novel methods. Numerical methods had become widely applied in the wide range of science and technology. Applicable range of the numerical methods was further broaden by the invention of the high–order class of the methods. Lower requirements of the computational time and memory of the high–order methods enable their application even for complex systems, such as the plasma produced by high–power laser facilities [2, 3, 4].

This work is dedicated to the numerical methods for laser–plasma interaction modeling. More precisely, the thesis deals with the plasma created by the interaction of an intense laser pulse with matter. Specifically, we develop the methods for solving the hydrodynamic equations, considering the plasma as a compressible fluid with additional physical processes like absorption of laser light or heat conduction. The hydrodynamic model compromises between a detailed physical description and a computational efficiency. The efficiency is crucial for the simulations of complex processes like the laser–matter interaction experiments. Applicability and limits of the hydrodynamic model are discussed later.

Laser plasma interaction experiments typically cover a wide range of physical parameters. The characteristic density ranges from a vacuum limit to a few times the solid state density and the temperature scales from thousands to hundred millions degrees Celsius or Kelvin. Research on such high energy density states of the matter has begun about 15 years before the discovery of a laser itself when a release of a huge amount of energy in the nuclear reactions of fission and later fusion has been achieved in explosions. Further down–scaling of the plasma experiments and a possible control of released energy ware enabled by the discovery of lasers as a high power energy source. The energy densities sufficient for strong material modifications and plasma production were achieved in 1960s. Since that, many practical applications of laser matter interaction have been proposed. The most challenging among them would be a release of the thermonuclear energy in a hydrogen target compressed by a powerful lasers. This is the goal for the world's top research laboratories.

1.1. Layout of the thesis

This thesis presents the work performed during my Ph.D. study under the dual supervision of Professors R. Liska and J. Limpouch at the Department of Physical Electronics of the Faculty of Nuclear Sciences and Physical Engineering of the Czech Technical University (CTU) in Prague jointly with Professors V. T. Tikhonchuk and J. Breil at the Center for Intense Lasers and Applications (CELIA) laboratory of the Bordeaux University. My mission in CTU was the development and implementation of new routines for modeling the laser light absorption in a plasma and in microstructured materials in the hydrodynamic code PALE [5], whereas I performed mainly the numerical analysis of the remapping methods during the time of my staying at CELIA. That is one reason why this thesis is divided into the two complementary parts. However, thanks to the deep scientific background of my supervisors and collaborators, both topics were discussed at both institutes.

The introduction and overview of the recent progress in the field of the laser–plasma modeling is presented in the second chapter, including the description of a hydrodynamic model, Lagrangian and Arbitrary Lagrangian–Eulerian (ALE) numerical methods, a high–order remap and the laser–matter interaction.

The third chapter is devoted to the description of the high–order remapping methods. The remap represents a conservative interpolation between two computational grids. After the one–dimensional description of the remapping methods and their high–order extensions, various aspects as the bounds– and symmetry–preservation of the remap are applied in a two-dimensional (2D) geometry both for a scalar and a vector variables. At the end of the chapter, a description of the complete remapping algorithm for the Euler equations of inviscid compressible flows is presented.

Absorption of the laser in plasma is described in the fourth chapter. Physical description of the electromagnetic radiation propagation in a continuous media is followed by a numerical method which model this process. The ray–tracing method is further generalized for its application in the 2D cylindrically symmetric hydrodynamic code PALE [5]. Special aspects of the interaction of the laser radiation with microstructures materials such as low–density foams are pointed out, and a new efficient method for modeling of the laser absorption in foams is developed.

The fifth chapter is devoted to the demonstration of the numerical properties of various remapping methods and to the particular simulation of the laser light interaction with the low density foams. These simulation results are compared to the experimental data obtained on the PALS [6] and GEKKO [4] laser facilities.

1.2. Aim of the thesis

The general aim of the thesis is to contribute to the state–of–art knowledge in the high–order ALE numerical methods, remapping in particular, for the Euler equations and application of the ALE methods for modeling of laser plasma interaction processes.

The numerical diffusion during the necessary remap stage of the ALE method is reduced by developed high–order remapping methods. The symmetry preservation of the methods for vectors limitation is investigated in detail in the case of radial flows. These issues are recently largely discussed by the computational fluid dynamics community.

As a particular application, an interaction of a laser radiation with a low-density foam target is investigated. Experiments with microstructured foams having the mean density of a few mg/cm^3 show a significant improvement of a laser beam quality and its smoothing after propagation through a foam. This smoothing is essential for the Inertial Confinement Fusion (ICF) applications as it permits to achieve a much better implosion quality. The exact physical mechanism of the foam ionization by the laser light is of a microscopic nature and standard hydrodynamic codes, which are considering the foam as a continuous media of an equivalent density, overestimate the speed of the laser penetration in foams. In this thesis, we propose a new model of foam ionization and a modification of a laser energy absorption method. It accounts the microscopic foam structure within the standard continuous hydrodynamic model. This new model matches the experimental results of the laser–foam interaction. These modifications were achieved by the implementation of a 3D ray-tracing algorithm in the 2D cylindrically symmetric code PALE [5].

2. State of the art

This chapter summarizes the common background knowledge required for hydrodynamic simulations of a laser–generated plasma. The hydrodynamic description of the plasma is presented and followed by appropriate numerical methods. The recent status of high–order hydrodynamic methods for the particular application is reviewed with a special focus on remapping methods. Finally, we introduce a laser absorption as an additional term to the hydrodynamic model and point out the specificity of the absorption in low–density foams.

2.1. Hydrodynamic model of a laser produced plasma

In general, the evolution of charged particles in a plasma is well described by the Vlasov–Fokker–Planck equations. These equations for the distribution functions $f_e(\vec{r}, \vec{v}, t)$ and $f_i(\vec{r}, \vec{v}, t)$ for electrons and ions in a six–dimensional phase space are completed by the Maxwell equations for the electric and magnetic field evolution. However, the direct solution of this system is computationally expensive and it is possible only for special configurations. Particle in cell (PIC) methods represent an example of numerical methods developed for a detail description of the plasma. PIC methods are widely used for modeling of the high–intensity laser–plasma interaction on short time and spatial scales [7], where these methods are more adapted to a collisionless plasma and only low densities can be simulated. On the contrary, due to a high computational cost, the PIC methods are not applicable for direct simulations of the interaction of a long laser pulse with a complex target.

Hydrodynamic equations, i.e. conservation laws for the mass, momentum and total energy, represent the moments of the Vlasov–Fokker–Planck equations. These hydrodynamic equations are closed by an expression for the pressure as a function of concerned variables. This expression is called an equation of state. For the plasma considered here, the integration of the Vlasov–Fokker–Planck equations over the velocity space brings hydrodynamic equations for two fluids assuming that the velocity distributions functions of electrons and ions are close to local Maxwellian thermal distributions.

If the plasma magnetization can be neglected and the electron and ion temperatures and densities are close to each other, a one–fluid compressible non–viscous hydrodynamics described by the Euler equations is sufficient to model the important physical phenomena in the system. In difference from the neutral gas dynamics, the plasma hydrodynamics includes additional terms describing a heat conductivity, an absorption model of the laser radiation and appropriate equations of state [8]. Further possible extensions are represented by a radiation transport, a transport of super–thermal particles or considering two different temperatures for the electrons and ions.

2.1.1. Euler equations in Lagrangian coordinates

The fundamental set of the hydrodynamic Euler equations for compressible non–viscous fluid in Lagrangian coordinates has the form

$$\frac{\mathrm{d}\rho}{\mathrm{d}t} + \rho \,\mathrm{div}\,\vec{u} = 0 \tag{2.1}$$

$$\rho\frac{\mathrm{d}\vec{u}}{\mathrm{d}t} + \mathrm{grad}\,p = 0 \tag{2.2}$$

$$\rho\frac{\mathrm{d}\epsilon}{\mathrm{d}t} + p \,\mathrm{div}\,\vec{u} = 0\,, \tag{2.3}$$

where ρ stands for the fluid density, $\vec{u}$ the velocity, p the pressure, $\epsilon = e/\rho - \vec{u}^2/2$ the specific internal energy (energy per unit mass) and e the total energy density (energy per unit volume). The material derivative $\frac{\mathrm{d}}{\mathrm{d}t}$ along the infinitesimal fluid element path is defined by

$$\frac{\mathrm{d}}{\mathrm{d}t} = \frac{\partial}{\partial t} + \vec{u}\cdot\mathrm{grad}\,,$$

any infinitesimal fluid element motion is described by an Ordinary Differential Equation (ODE)

$$\frac{\mathrm{d}\vec{x}}{\mathrm{d}t} = \vec{u}\,,$$

and the system is closed by the equation of state

$$p = p(\rho, \epsilon)\,.$$

A particular state of the modeled continuum is given by a set of three variables. For this set, more options are available. In the further text, we denote the mass M, the momentum $\vec{P} = M\vec{u}$ and the total energy E as the conservative variables with their volume densities[1] ρ, $\vec{\mu}$, e. Another set of the fluid density ρ, velocity $\vec{u}$ and pressure p is called the primitive variables.

2.2. Numerical methods

To be able to solve the hydrodynamic model of the plasma numerically, we need to divide the investigated space into smaller parts. This process is called discretization.

Generally, there are two approaches for the model of a continuum fluid. We can divide the investigated area into non–moving (spatially–fixed) parts (cells) and investigate a flow and an evolution of the fluid in these cells. This approach is called Eulerian and is advantageously used in many applications, e.g. for steady state airfoil flows.

In the second approach, the fluid itself is divided into pieces (cells) instead of the space. Now, we are interested in the temporal evolution of these fluid cells along the stream lines, which represent the motion of the fluid pieces. This Lagrangian description is more appropriate for the fluids with a moving boundary (both the boundary of the fluid itself or the boundary between materials). Another advantage of the Lagrangian description is its easy application for a large scale compression or expansion. All these situations are typical for the investigated laser–plasma interaction.

2.2.1. High–order Lagrangian methods

If the computational error in a given norm decreases faster than linearly during the grid refinement[2], we call the method to be of a high–order. In the Eulerian framework with a static computational grid, a very high–order of accuracy is typically achieved by recent numerical methods [9] in the smooth regions, while the accuracy on discontinuities is limited to the first order.

For the hydrodynamic Euler equations in Lagrangian coordinates, two types of the spatial discretization are applied, namely staggered and cell–centered.

In the cell–centered discretization, all variables are interpreted as the mean value over the computational cell. This concept originates from the class of finite volume methods. The hydrodynamic code CHLER [10] is based on the cell–centered numerical scheme

---

[1] which we call distributions

[2] doubling the number of computational cells in each spatial dimension

[11] with the acoustic Godunov solver. Thanks to the piecewise linear reconstruction of the primitive variables with the standard slope limiter [12] using the generalized Riemann problem terminology [13], a high–order extension of the scheme is proposed in [14]. The second–order numerical scheme is formulated for an unstructured polygonal two–dimensional computational grid. A cylindrical extension of the numerical scheme is presented in [15]. For a 3D discretization, examples of the cell–centered Godunov–type methods are presented in [16, 17].

Another method, based on the discontinuous Galerkin numerical scheme [18, 19], is able to achieve the third–order of accuracy. However, the deformation of the computational grid and the evolution of the specific variables are solved separately in this scheme. Due to the separation, the direct application of a computational mesh smoothing, which is necessary for the laser–plasma modeling, does not preserve the third–order of accuracy [20].

For the staggered discretization, scalar variables (ρ, p, ϵ, e) are represented by their mean values in the cells, whereas vector quantities ($\vec{u}$, $\vec{x}$) are located at nodes of a computational grid. PALE (Prague ALE) code [21] using 2D quadrilateral, logically orthogonal computational mesh is based on the computation of nodal forces resulting from pressure gradients. In the staggered codes, these forces, together with the artificial viscosity– [22] and other forces, are used for the velocity calculation and a subsequent mesh motion. In the PALE code, the compatible total energy–conserving algorithm [23] for Lagrangian hydrodynamics is extended by adding the terms modeling the laser-plasma coupling [8, 24]. With my PhD work I contributed to the development and implementation of laser absorption modules in the PALE code.

Computational grids with curvilinear coordinates are investigated to achieve higher order of accuracy in the two dimensional hydrodynamics [19, 25]. These methods represent possible future of the high–order laser plasma modeling. However, current production codes for the laser–prodiced plasma applications rely mainly on the second–order Lagrangian discretizations.

2.2.2. Arbitrary Lagrangian–Eulerian methods

Arbitrary Lagrangian–Eulerian (ALE) methods combine the Lagrangian approach with a moving computational grid with the Eulerian description. For the purpose of plasma–generated plasma modeling, these methods attract a widespread interest [10, 26, 27, 28, 29, 30, 31, 32, 33].

Following the original work [34], the ALE method consists of the three parts. Several time–steps of the Lagrangian calculation (1) are followed by a smoothing and/or untangling of the computational grid (2). The second step is called rezoning. Finally, a conservative interpolation of the conservative variables (3) from the old Lagrangian grid to the smoothed one is performed. The last step is called remapping or advection, and it represents the Eulerian part of the method.

Although there is no temporal evolution during the remapping step, an exchange of the conservative quantities can be expressed in terms of fluxes.

The main motivation for the ALE methods is to avoid a degeneration of the computational mesh quality. In the Lagrangian approach, the computational grid is attached to the fluid and has to follow its evolution. It is well adapted for a laminar flow, but a vortex or a shear flow appearing in the fluid are resulting in a severe degradation of the computational mesh. Non–convex, self–intersecting or inverted (negative directional–volume) cells are examples of the degradation. Smoothing and/or untangling of the computational grid are aiming on avoiding of all such situations. A detailed review of the recent rezoning methods is presented in [24].

2.3. High–order remapping methods

In the previous section, the remapping procedure was introduced as a last part of the ALE algorithm. For ALE transformation where the connectivity of the Lagrangian and rezoned meshes are the same, the conservation of the total mass $\sum_c M_c$, components of momentum $\sum_c P^x_c$,$\sum_c P^y_c$ and the total energy $\sum_c E_c$, is easily enforced by the flux form of the remapping method. For each of the conservative quantities in the Lagrangian cell $Q_c \in \{M_c, P^x_c, P^y_c, E_c\}$ and the remapped quantity $\tilde{Q}_c$ on the rezoned mesh, the flux form can be written as

$$\tilde{Q}_c = Q_c + \sum_{c' \in \mathcal{C}(c)} F^Q_{c'c}\,, \qquad\qquad F^Q_{c'c} = -F^Q_{cc'}\,, \tag{2.4}$$

Here $F^Q_{c'c}$ stands for the numerical flux through the cell interface (edge) (c', c). The set of all neighboring cells to the cell c is denoted by $\mathcal{C}(c)$.

A natural existence of discontinuous solutions for the Euler equations brings the next requirement. A remapping method should avoid the development of new local extrema or even numerical oscillations. This requirement is specific for high–order methods, because standard first order remapping methods produce a sufficient quantity of numerical diffusion to avoid these problems. A discrete maximum principle (DMP) is adapted in recent remapping methods. According to this principle, the remapped value is bounded by the extreme values in the surrounding cells of the old mesh. The DMP principle can be applied for the both primitive variables [35] and conservative variables [8, 36]. It has been proved analytically [9] that the strict DMP requirement limits the order of remapping methods to the second order, whereas the higher–order is preserved only in sufficiently smooth areas without local extrema. Modifications of the DMP necessary to avoid the loss of convergence around the extrema are described in [9, 37].

To meet all these requirements, the following general algorithm for the second–order remapping was described in [38]. The first step is a calculation of a piecewise linear reconstruction of conservative quantities distributions. Limiters [39] are applied to reduce slopes of the reconstruction near discontinuities. The second step is a quadrature of the reconstruction. The quadrature can be performed over the exact intersections of the Lagrangian and rezoned grid or over swept regions [40]. The latter option costs much less computational time because the swept regions are defined only by the grid movement, avoiding costly calculation of all cell intersections.

2.3.1. Slope limiters for a piecewise polynomial reconstruction

The aim of the limiters is to reduce a slope [39] of a piecewise linear reconstruction and of the higher–order term for a general polynomial reconstruction. A wide range of slope limiters even for a very high–order polynomial reconstruction is available for high–order Euler methods with a static, square computational mesh. The limitation is applied in a hierarchical order starting from the highest order terms of the reconstruction. In the remapping context for the ALE method, one needs to handle non–equidistant and non–orthogonal meshes, whereas the main theoretical background is limited to limiters for a second–order piecewise linear reconstruction.

For the piecewise linear reconstruction of a scalar quantity in the remapping context, the bounds preservation is typically enhanced by the classical Barth–Jespersen slope limiter [12, 41]. A comprehensive review and performance of selected slope limiters for a piecewise parabolic[3] reconstruction is provided in the first part of the third chapter.

---

[3] we use the term parabolic in a 1D context and the term quadratic for more spatial dimensions

2.3.2. Slope limiters for vectors

The traditional approach for vectors consists in a definition of bounds for the Cartesian vector components. However, it was recognized that such a definition is not coordinate invariant. In particular, the definition gives non–symmetric bounds (for example, different bounds for the radial velocity vector on an equiangular polar mesh for nodes with the same radius but different angles).

An interesting idea, which was suggested in the context of vector field reconstruction, defines the bounds by using the Vector Image Polygon (VIP) [42] constructed as the convex hull of vectors in the neighboring cells. The approach is further extended to the symmetric remapping context in the second part of the third chapter. The original VIP approach has been already applied to remapping in [43, 44].

In the framework of cell-centered Lagrangian discretization and vector field reconstruction inside the cell, it was suggested to use bounds related to the projection of the velocity vector to principal axes of a mesh deformation tensor [45, 46, 47], that is, to use directions related to the flow. Inspired by the idea, we applied the projection method for a Flux–Corrected Remapping method. The description of the method for a cell–centered discretization is provided in the last part of the third chapter.

2.3.3. Flux–Corrected Remapping

The original Flux–Corrected Transport (FCT) approach was proposed by Boris and Book [48] and further advanced by Zalesak [49]. The method is often used to solve advection problems and hyperbolic systems of partial differential equations. However, this method can be applied to more general problems. A comprehensive summary of FCT is presented in the book [50].

The concept of remapping conservative variables for fluid dynamics was suggested in [35, 51, 52], and following these papers we also adopt the term Flux–Corrected Remapping (FCR). A similar method, based on the direct optimization process for a high–order remap of a scalar quantity, in presented in [53, 54].

The basic idea of FCT/FCR is to avoid overshoots, undershoots and oscillations, which are typical for the high–order methods. It is achieved by a convex combination of some higher-order fluxes F^{H} with low-order fluxes F^{L}, so that the local bounds are preserved.

The FCR flux across the interface of two cells has the form

$$F^{\mathrm{FCR}} = CF^{\mathrm{H}} + (1 - C)F^{\mathrm{L}} = F^{\mathrm{L}} + C \underbrace{\left(F^{\mathrm{H}} - F^{\mathrm{L}}\right)}_{dF}, \tag{2.5}$$

where dF is referred to as the antidiffusive flux and the correction factor $0 \leq C \leq 1$ controls the amount of the high–order portion of the flux used. The FCR method finds the highest C, i.e. closest to the high–order fluxes, for which the FCR fluxes preserve local bounds. Using the worst case scenario, the global (mesh-wide) optimization problem is decoupled into a set of local problems, wherein the C is computed.

2.4. High–energy laser–matter interaction

Laser intensity of a few times 10^{14} W/cm^2 on a target can be maintained for the timescale from a few hundreds picoseconds to a few nanoseconds on the present days high–power laser facilities [4, 6]. For the investigated targets made of low–atomic number materials like plastic or Aluminum, such a laser intensity is sufficient to rapidly ionize the matter and transform it in a plasma. For simplicity in simulations presented in this thesis, a full ionization of the matter is assumed and an ideal gas equation of state is used. For the considered laser wavelengths of 350 nm or 438 nm, the electron and ion distribution functions are close to the Maxwell distribution, satisfying the requirement for the hydrodynamic model.

A deposition of the laser energy into the target is described through the new term [8] in (2.3)

$$\rho \frac{\mathrm{d}\epsilon}{\mathrm{d}t} + p \operatorname{div} \vec{u} = - \operatorname{div} \vec{I}. \tag{2.6}$$

This term, which express the divergence of the laser intensity $\vec{I}$, is calculated with a separate routine in a hydrodynamic code, taking into account different mechanisms of the laser absorption.

2.4.1. Propagation and absorption of laser radiation in plasma

According to the fundamental plasma theory, the laser radiation can propagate only in a plasma with the free electron density lower than the critical value. This critical electron plasma density n_e^{crit} depends only on the laser wavelength λ and the fundamental physical constants such as the speed of light c, the electron mass m_e and charge e

$$n_e^{\text{crit}} = \frac{m_e \pi c^2}{e^2 \lambda^2}\,. \tag{2.7}$$

According to this theory, basic numerical methods are tracking the laser beam propagation in the sub–critical plasma. Once the critical density is reached, some amount of the laser energy is absorbed in the target. In these oversimplified models, the amount of the absorbed energy is an adjustable parameter, typically ranging from 0.3 to 1.0.

More advanced models are based on the geometric optics theory. In this case, the laser beam is split in a set of rays each of them carrying a certain amount of energy, and a ray equation is solved for each ray separately. The total absorption in the ray–tracing algorithm is calculated as a sum of contributions of each ray, which are defined by the local plasma parameters. A general three–dimensional ray–tracing algorithm for a laser plasma is described in [55]. Taking the diffraction of the laser light into account, the recent article [56] presents another interesting method. In the thick ray approach, the laser beam is tracked and the evolution of a Gaussian beam wave front curvature along the beam is solved additionally.

Basic mechanism of the laser light energy deposition is the inverse bremsstrahlung absorption. In this case, the oscillation energy of an electron in the harmonic laser electric field is transformed in Coulomb collisions with ions into the chaotic movement thus increasing the plasma temperature. This process in dominant for the considered laser parameters.

Moreover, contrary to the non–collisional mechanisms, the inverse bremsstahlung absorption for the investigated laser intensity depends only on the electron density and temperature, which makes this process suitable for hydrodynamic modeling.

2.4.2. Low–density foam target specifics

Low–density foam targets could improve significantly the Inertial Confinement Fusion (ICF) target design. The original proposal [57] assumes smoothing of radiation inhomogeneities by the heat conductivity in the low–density layer encapsuling the inner target. A symmetric implosion of the inner capsule is achieved thanks to the smoothing the energy flux in the preheated foam. Another approach of laser beam smoothing in a subcritical foam was proposed in [58].

Foams are a complex microstructured material, which cannot be described within a conventional hydrodynamic model. A detailed information about the laser–foam interaction is needed for a reliable utilization of the low–density foam layer. The laser absorption, energy transfer and shock wave propagation in underdense[4] foams have been recently studied experimentally at nanosecond scale lasers PALS and GEKKO. The qualitative theory of the laser foam interaction introduces a fast homogenization stage, where empty spaces inside the foam pores are rapidly filled by the plasma expanding thin solid layers. Then the laser propagation in the ionized foam is described in the approximation of a homogeneous low–density plasma. However, such a model overestimates the shock wave amplitude and the ionization front propagation speed significantly [58].

The same overestimation of the ionization front speed was observed for hydrodynamic simulations of the foams considered as a homogeneous low–density media. A possibility of modeling the microscopic foam structure is investigated in [59]. This approach provides an appropriate propagation speed of the ionization front. However, its wider application is limited due to numerical difficulties with the structured mesh evolution and the method can not be generalized to 3D.

Another model, applicable for the 1D hydrodynamic simulations is suggested in [60]. By considering a microscopic model of the foam homogenization process, a time–dependent local absorption coefficient for the laser light is introduced. It opens a possibility to a quantitative account of the microscopic processes in the macroscopic hydrodynamics. A novel method, generalizing this idea of a time dependent laser absorption coefficient, is presented in the fourth chapter of this thesis.

---

[4] the foam with an average density lower than the plasma critical density

3. Remapping methods

As stated in the second chapter, remapping represents a special kind of an interpolation. To be conservative, this interpolation is written in the flux form (2.4). Moreover, numerical fluxes have the form of a definite integral of a reconstructed function over the overlapping region of the Lagrangian and rezoned meshes.

In one spatial dimension, this integral has a unique form and there are reliable methods to perform a piecewise polynomial reconstruction. Therefore, we start with the description of possible reconstructions for the remapping methods.

3.1. 1D reconstruction

In the one–dimensional case, we denote the nodal quantity, as the position of the node, by a half–step subscript and the cell–based quantity by an integer in a standard way, so that the cell i is surrounded by the nodes $i-1/2$, $i+1/2$. The positions of the old (Lagrangian) grid nodes are denoted by the set $\{x_{i-1/2}\}, i \in 1 \dots N+1$, where N stands for the total number of cells. The cell center is $x_i = (x_{i+1/2} + x_{i-1/2})/2$. The rezoned grid is indicated by the superscript n, e.g. its nodal position is $x^n_{i-1/2}$.

The mean value $\overline{u}_i$ is the volume density of a conservative quantity over cell. It may represent e.g. the cell density, momentum or total energy $u \in \{\rho, \mu, e\}$ for the Euler equation. We define the mean

$$\overline{u}_i = \frac{1}{\Delta x_i} \int_{x_{i-1/2}}^{x_{i+1/2}} u^R(x) \, \mathrm{d}x \, , \tag{3.1}$$

where $\Delta x_i = x_{i+1/2} - x_{i-1/2}$ is the cell volume (length in 1D) and $u^R(x)$ the reconstruction of the unknown function $u(x)$. This function is unknown after each Lagrangian time–step. One of the main remapping tasks is to find the appropriate reconstruction $u^R(x)$ of unknown function $u(x)$ from the mean values $\overline{u}_i$. The task is addressed in detail the 1D analysis presented in this subsection.

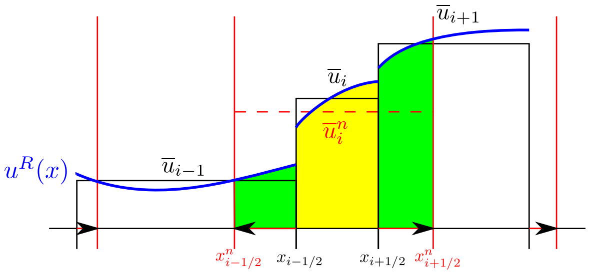

Figure 3.1.: Remapping in a single cell. Black nodes of the Lagrangian computational mesh, red nodes of the rezoned mesh and the blue reconstruction function $u^R(x)$ are illustrated. Numerical fluxes are represented by the green areas.

Knowing the reconstruction $u^R(x)$, a remapped (new) cell mean is simply given by

$$\overline{u}_i^n = \frac{1}{\Delta x_i^n} \int_{x^n_{i-1/2}}^{x^n_{i+1/2}} u^R(x)\,\mathrm{d}x\,, \tag{3.2}$$

where $\Delta x_i^n = x^n_{i+1/2} - x^n_{i-1/2}$ is the volume of the new cell, i.e. the cell after the rezone step. The definite integral on the right hand side can be further split, as indicated in Fig. 3.1. One part corresponds to the mean value of the old cell and the rest is a sum of numerical fluxes (2.4), i.e. quadrature of the appropriate reconstructions over the overlapping regions of the Lagrangian and rezoned mesh.

For a remapping method, a natural requirement is the conservation of the total amount of a conservative quantity in a form

$$\sum_{i=1}^{N} \overline{u}_i \Delta x_i = \sum_{i=1}^{N} \overline{u}_i^n \Delta x_i^n\,. \tag{3.3}$$

This requirement is fulfilled using the flux form (2.4) of the remap under the assumption of rigid boundary during the rezone, i.e $x_{1/2} = x^n_{1/2}$ and $x_{N+1/2} = x^n_{N+1/2}$. After conservation, another requirement is the preservation of local bounds. We start with a simple definition of the bounds given by the local values on the old mesh

$$\begin{aligned} u_i^{\min} &= \min\left\{\overline{u}_{i-1}, \overline{u}_i, \overline{u}_{i+1}\right\} \\ u_i^{\max} &= \max\left\{\overline{u}_{i-1}, \overline{u}_i, \overline{u}_{i+1}\right\}\,. \end{aligned} \tag{3.4}$$

The remapped mean value (and so the remap) is in bounds if $\forall i,\ u_i^{\min} \le \overline{u}_i^n \le u_i^{\max}$.

3.1.1. Piecewise constant reconstruction

The piecewise constant reconstruction has the form $u_i^R(x) = u_i^D$ for $x \in [x_{i-1/2}, x_{i+1/2}]$, where u_i^D is an unknown. According to the definition (3.1), we get

$$\overline{u}_i = \frac{1}{\Delta x_i} \int_{x_{i-1/2}}^{x_{i+1/2}} u_i^D \, \mathrm{d}x = u_i^D \frac{1}{\Delta x_i} \int_{x_{i-1/2}}^{x_{i+1/2}} \mathrm{d}x = u_i^D \text{ so, } u_i^D = \overline{u}_i \,. \tag{3.5}$$

This low–order reconstruction preserves bounds for the reconstruction as $\forall i, u_i^R(x) = u_i^D = \overline{u}_i$ for $x \in [x_{i-1/2}, x_{i+1/2}]$

$$u_i^R(x) \geq \min\left\{\overline{u}_{i-1}, \overline{u}_i, \overline{u}_{i+1}\right\}, \qquad u_i^R(x) \leq \max\left\{\overline{u}_{i-1}, \overline{u}_i, \overline{u}_{i+1}\right\}\,. \tag{3.6}$$

We denote the associated remapping method using this reconstruction as a donor–cell[1] or low–order remapping method. The low–order remapping method preserves the bounds (3.4).

3.1.2. Unlimited piecewise linear reconstruction

For the one spatial dimension, the reconstruction in the cell i, i.e. $x \in [x_{i-1/2}, x_{i+1/2}]$ has the general form

$$u_i^R(x) = u_i + u_i^x (x - x_i)\,, \tag{3.7}$$

originating from the Taylor series around the point x_i. The condition (3.2) leads to $u_i = \overline{u}_i$. The two point centered finite difference can by used to estimate the approximation of the first derivative (slope)

$$u_i^x = \frac{\overline{u}_{i+1} - \overline{u}_{i-1}}{x_{i+1} - x_{i-1}}\,. \tag{3.8}$$

In general, this reconstruction can violate the bounds (3.6) in the presence of a discontinuity or local extrema. The (unlimited) slope calculated by the central difference (3.8) provides an incorrect numerical flux. Regardless if the flux is too low or too high, if the reconstructed function is out of bounds (3.6), the remapped value may consequently exceed (3.4). To avoid such a situation, slope limiters are applied to the reconstruction. The goal of a slope limiter is to reduce $|u_i^x|$ such that the reconstruction stays in bounds. These

---

[1] or abbreviated donor

limiters are extensively employed in numerical methods for the resolution computational of conservation–laws [61].

3.1.3. Slope limiters for a piecewise linear reconstruction

Here, we present some examples of piecewise linear reconstructions with slope limiters.

Minmod (MM) limiter [61] is based on a combination of the different derivative approximations, such as the forward, central (3.8) and backward difference. The limited value ${}^{\mathrm{mm}}u_i^x$ replace the slope u_i^x in (3.7)

$$ {}^{\mathrm{mm}}u_i^x = \mathrm{minmod}\left(u_i^x, \beta\frac{\overline{u}_{i+1} - \overline{u}_i}{x_{i+1} - x_i}, \beta\frac{\overline{u}_i - \overline{u}_{i-1}}{x_i - x_{i-1}} \right) , \tag{3.9} $$

where $\beta \in (1, 2)$ is a parameter (the low values of β lead to stronger limitation, whereas the high values lead to better extrema preservation and convergence on smooth solution). The function minmod is defined as

$$ \mathrm{minmod}(a, b, c) = \begin{cases} \min(a, b, c) & \text{if } a, b \text{ and } c \text{ are positive} \\ 0 & \text{if } a, b \text{ and } c \text{ do not have equal sign} \\ -\min(|a|, |b|, |c|) & \text{if } a, b \text{ and } c \text{ are negative} \end{cases} \tag{3.10} $$

Barth–Jespersen (BJ) limiter [12] is constructed to preserve the bounds (3.4) by definition. The nodal min and max

$$ u_{i-1/2}^{\min} = \min\left(\overline{u}_{i-1}, \overline{u}_i\right) $$
$$ u_{i-1/2}^{\max} = \max\left(\overline{u}_{i-1}, \overline{u}_i\right) $$

are combined with the nodal extrapolated values

$$ u_{i,i-1/2}^u = u_i^u(x_{i-1/2}) = \overline{u}_i - u_i^x \Delta x_i/2 \tag{3.11} $$
$$ u_{i,i+1/2}^u = u_i^u(x_{i+1/2}) = \overline{u}_i + u_i^x \Delta x_i/2 \tag{3.12} $$

to get the value of the nodal slope limiter

$$\alpha_i^{i\pm1/2} = \begin{cases} \min\left(1, \frac{u^{\max}_{i\pm1/2}-\overline{u}_i}{u^u_{i,i\pm1/2}-\overline{u}_i}\right) & \text{for} \quad u^u_{i,i\pm1/2}-\overline{u}_i > 0 \\ 1 & \text{for} \quad u^u_{i,i\pm1/2}-\overline{u}_i = 0 \\ \min\left(1, \frac{u^{\min}_{i\pm1/2}-\overline{u}_i}{u^u_{i,i\pm1/2}-\overline{u}_i}\right) & \text{for} \quad u^u_{i,i\pm1/2}-\overline{u}_i < 0 \end{cases} \tag{3.13}$$

The final cell–based value of α_i in the cell i is the minimum of the both nodes values $\alpha_i = \min(\alpha_i^{i-1/2}, \alpha_i^{i+1/2})$. This widely–used BJ limited reconstruction has the final form

$$^{\mathrm{BJ}}u_i^R(x) = \overline{u}_i + \alpha_i u_i^x (x - x_i)\,. \tag{3.14}$$

Venkatakrishnan limiter [62, 63] is a smooth extension of the BJ limiter. Function $\min(1, y)$ in (3.13) is replaced by $\frac{y^2+2y}{y^2+y+2}$ and (3.13) is changed to

$$\phi_i^{i\pm1/2} = \begin{cases} \frac{1}{\Delta u_{i,i\pm1/2}} \left[\frac{\left((\Delta u_i^{\max})^2+\epsilon^2\right)\Delta u_{i,i\pm1/2} + 2\Delta u_{i,i\pm1/2}{}^2 \Delta u_i^{\max}}{(\Delta u_i^{\max})^2 + 2\Delta u_{i,i\pm1/2}{}^2 + \Delta u_i^{\max}\Delta u_{i,i\pm1/2} + \epsilon^2} \right] & \text{for} \quad \Delta u_{i,i\pm1/2} > 0 \\ \\ \frac{1}{\Delta u_{i,i\pm1/2}} \left[\frac{\left((\Delta u_i^{\min})^2+\epsilon^2\right)\Delta u_{i,i\pm1/2} + 2\Delta u_{i,i\pm1/2}{}^2 \Delta u_i^{\min}}{(\Delta u_i^{\min})^2 + 2\Delta u_{i,i\pm1/2}{}^2 + \Delta u_i^{\min}\Delta u_{i,i\pm1/2} + \epsilon^2} \right] & \text{for} \quad \Delta u_{i,i\pm1/2} < 0 \end{cases}, \tag{3.15}$$

where $u_i^{\min}$, $u_i^{\max}$ are given by (3.4)

$$\begin{aligned} \Delta u_i^{\max} &= u_i^{\max} - \overline{u}_i \\ \Delta u_i^{\min} &= u_i^{\min} - \overline{u}_i \\ \Delta u_{i,i\pm1/2} &= u^u_{i,i\pm1/2} - \overline{u}_i\,. \end{aligned}$$

The small parameter ϵ, which is of the order of machine precision, is suggested to avoid the division by zero. Again, the cell–based values ϕ_i are computed as $\phi_i = \min\left(\phi_i^{i-1/2}, \phi_i^{i+1/2}\right)$ giving the final reconstruction

$$^{\mathrm{Venk}}u_i^R(x) = \overline{u}_i + \phi_i u_i^x (x - x_i)\,. \tag{3.16}$$

Although there is a plenty of other possibilities for general purpose slope limiters, a particular application of the limiters for the scalar remapping methods is most often limited to the BJ limiter or its smooth extensions. This is mainly due to the limiter simplicity, preservation of the local bounds as well as the second order of accuracy on continuum functions and an easy extension for multidimensional problems.

3.1.4. Unlimited piecewise parabolic reconstruction

The piecewise parabolic reconstruction is a natural extension of the previous piecewise linear reconstruction

$$u_i^R(x) = u_i + u_i^x(x - x_i) + \frac{1}{2}u_i^{xx}(x - x_i)^2 \,. \tag{3.17}$$

Computation of the unknown coefficients u_i, u_i^x a u_i^{xx} is derived below. A least–square procedure together with the conservativity requirement are applied to obtain analytical formulas.

From the conservation of the mean value in a single cell, the first relation between the unknown coefficients is derived

$$\begin{aligned}
\int\limits_{x_{i-1/2}}^{x_{i+1/2}} u_i^R(x)\,\mathrm{d}x &= \int\limits_{x_{i-1/2}}^{x_{i+1/2}} u_i + u_i^x(x - x_i) + \frac{1}{2}u_i^{xx}(x - x_i)^2\,\mathrm{d}x \\
&= u_i\Big[x\Big]_{x_{i-1/2}}^{x_{i+1/2}} + u_i^x\left[\frac{1}{2}(x - x_i)^2\right]_{x_{i-1/2}}^{x_{i+1/2}} + \frac{1}{2}u_i^{xx}\left[\frac{1}{3}(x - x_i)^3\right]_{x_{i-1/2}}^{x_{i+1/2}} \\
&= u_i\underbrace{(x_{i-1/2} - x_{i+1/2})}_{\Delta x_i} + \frac{1}{2}u_i^x\Big[\underbrace{(x_{i+1/2} - x_i)}_{\frac{\Delta x_i}{2}}{}^2 - \underbrace{(x_{i-1/2} - x_i)}_{-\frac{\Delta x_i}{2}}{}^2\Big] + \\
&\quad + \frac{1}{6}u_i^{xx}\left[\left(\frac{\Delta x_i}{2}\right)^3 + \left(\frac{\Delta x_i}{2}\right)^3\right] \\
&= u_i\Delta x_i + \frac{1}{24}u_i^{xx}\Delta x_i^3 = \overline{u}_i\Delta x_i
\end{aligned}$$

$$u_i = \overline{u}_i - \frac{1}{24}u_i^{xx}\Delta x_i^2 \,. \tag{3.18}$$

The remaining coefficients are computed by the minimization of the least–square deviation functional $\phi(u_i, u_i^x, u_i^{xx})$ in the neighboring cells

$$\phi(u_i, u_i^x, u_i^{xx}) = \sum_{j\in\{i-1,i+1\}} \left(\overline{u}_j - \frac{1}{\Delta x_j}\int\limits_{x_{j-1/2}}^{x_{j+1/2}} u_i^R(x)\,\mathrm{d}x\right)^2 \,.$$

Taking (3.17) into account, the deviation functional $\phi(u_i, u_i^x, u_i^{xx})$ becomes

$$\left[\overline{u}_{i-1} - u_i - u_i^x \frac{(\Delta x_i/2)^2 - (\Delta x_{i-1} + \Delta x_i/2)^2}{2\Delta x_{i-1}} - u_i^{xx} \frac{-(\Delta x_i/2)^3 + (\Delta x_{i-1} + \Delta x_i/2)^3}{6\Delta x_{i-1}}\right]^2 + \\ + \left[\overline{u}_{i+1} - u_i - u_i^x \frac{(\Delta x_{i+1} + \Delta x_i/2)^2 - (\Delta x_i/2)^2}{2\Delta x_{i+1}} - u_i^{xx} \frac{(\Delta x_{i+1} + \Delta x_i/2)^3 - (\Delta x_i/2)^3}{6\Delta x_{i+1}}\right]^2 .$$

In the next step, we replace u_i by (3.18)

$$\left[\overline{u}_{i-1} - \overline{u}_i + \frac{1}{2}u_i^x(\Delta x_{i-1} + \Delta x_i) - \frac{1}{12}u_i^{xx}(\Delta x_{i-1} + \Delta x_i)(2\Delta x_{i-1} + \Delta x_i)\right]^2 + \\ + \left[\overline{u}_{i+1} - \overline{u}_i - \frac{1}{2}u_i^x(\Delta x_{i+1} + \Delta x_i) - \frac{1}{12}u_i^{xx}(\Delta x_{i+1} + \Delta x_i)(2\Delta x_{i+1} + \Delta x_i)\right]^2 .$$

To simplify the notation, we further introduce

$$\begin{aligned} \Delta x_{i,i\pm1} &= \Delta x_{i\pm1} + \Delta x_i \\ \Delta_2 x_{i,i\pm1} &= 2\Delta x_{i\pm1} + \Delta x_i \end{aligned} \tag{3.19}$$

to get the final formula for the deviation functional

$$\phi(u_i^x, u_i^{xx}) = \left[\overline{u}_{i-1} - \overline{u}_i + \frac{1}{2}u_i^x \Delta x_{i,i-1} - \frac{1}{12}u_i^{xx}\Delta x_{i,i-1}\Delta_2 x_{i,i-1}\right]^2 + \\ + \left[\overline{u}_{i+1} - \overline{u}_i - \frac{1}{2}u_i^x \Delta x_{i,i+1} - \frac{1}{12}u_i^{xx}\Delta x_{i,i+1}\Delta_2 x_{i,i+1}\right]^2 . \tag{3.20}$$

To minimize the functional, we express its first derivatives according to the unknown parameters u_i^x, u_i^{xx} and set them equal to zero

$$\begin{aligned} 0 = \frac{\partial\phi}{\partial u_i^x} &= \left[\overline{u}_{i-1} - \overline{u}_i + \frac{1}{2}u_i^x \Delta x_{i,i-1} - \frac{1}{12}u_i^{xx}\Delta x_{i,i-1}\Delta_2 x_{i,i-1}\right] \Delta x_{i,i-1} - \\ &- \left[\overline{u}_{i+1} - \overline{u}_i - \frac{1}{2}u_i^x \Delta x_{i,i+1} - \frac{1}{12}u_i^{xx}\Delta x_{i,i+1}\Delta_2 x_{i,i+1}\right] \Delta x_{i,i+1} \\ 0 = \frac{\partial\phi}{\partial u_i^{xx}} &= -\left[\overline{u}_{i-1} - \overline{u}_i + \frac{1}{2}u_i^x \Delta x_{i,i-1} - \frac{1}{12}u_i^{xx}\Delta x_{i,i-1}\Delta_2 x_{i,i-1}\right] \frac{1}{6}\Delta x_{i,i-1}\Delta_2 x_{i,i-1} - \\ &- \left[\overline{u}_{i+1} - \overline{u}_i - \frac{1}{2}u_i^x \Delta x_{i,i+1} - \frac{1}{12}u_i^{xx}\Delta x_{i,i+1}\Delta_2 x_{i,i+1}\right] \frac{1}{6}\Delta x_{i,i+1}\Delta_2 x_{i,i+1} . \end{aligned}$$

The final formula for the unlimited coefficients is obtained by the solution of this linear system. Here, we introduce a novel labeling $\overline{u}_i^x = u_i^x, \overline{u}_i^{xx} = u_i^{xx}$ to distinguish the coefficients of the linear and parabolic reconstructions[2]. The unlimited piecewise parabolic reconstruction has the final form

$$\overline{u}_i^x = 2\frac{(\overline{u}_{i+1} - \overline{u}_i)\Delta x_{i,i-1}\Delta_2 x_{i,i-1} + (\overline{u}_i - \overline{u}_{i-1})\Delta x_{i,i+1}\Delta_2 x_{i,i+1}}{\Delta x_{i,i-1}\Delta x_{i,i+1}(\Delta_2 x_{i,i-1} + \Delta_2 x_{i,i+1})} \tag{3.21}$$

$$\overline{u}_i^{xx} = 12\frac{(\overline{u}_{i+1} - \overline{u}_i)\Delta x_{i,i-1} - (\overline{u}_i - \overline{u}_{i-1})\Delta x_{i,i+1}}{\Delta x_{i,i-1}\Delta x_{i,i+1}(\Delta_2 x_{i,i-1} + \Delta_2 x_{i,i+1})} \tag{3.22}$$

$$u_i^R(x) = \overline{u}_i + \overline{u}_i^x(x - x_i) + \frac{1}{2}\overline{u}_i^{xx}\left[(x - x_i)^2 - \frac{1}{12}\Delta x_i^2\right]. \tag{3.23}$$

The last term in the previous formula results from the conservation requirement (3.18). In the 1D case of the parabolic reconstruction in a cell, the final derivative approximations are calculated using the two neighboring cells. An example of the reconstruction is plotted in Fig. 3.2. Presented solution of the system $\frac{\partial\phi}{\partial u_i^x} = 0$, $\frac{\partial\phi}{\partial u_i^{xx}} = 0$ is equivalent to the both zero contributions in the functional $\phi(u_i^x, u_i^{xx})$ in (3.20). In other words, the minimum of the deviation functional is always zero in the particular 1D case.

By following this minimization method, one may derive a general polynomial reconstruction in more spatial dimensions. As an example, a different expression for the slope

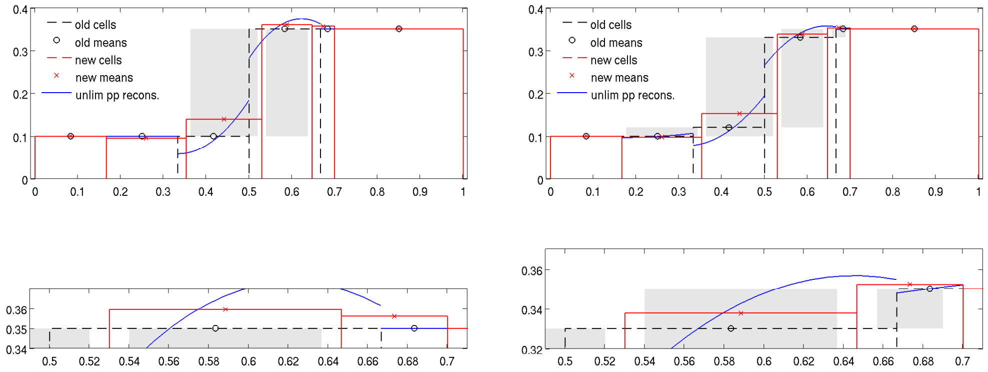

(a)

(b)

Figure 3.2.: Single remap of a step (a) and smooth (b) function with the unlimited piecewise parabolic reconstruction. Old grid with the mean values (circles) is in black, new grid is in red. Reconstruction is plotted in blue, its bounds in gray. A zoom is provided in the smaller bottom figures.

---

[2] but $\overline{u}_i \neq u_i$, see (3.18)

u_i^x in a 1D piecewise linear reconstruction can be found

$$u_i^x = 2\frac{(\overline{u}_{i+1} - \overline{u}_i)\Delta x_{i,i+1} + (\overline{u}_i - \overline{u}_{i-1})\Delta x_{i,i-1}}{\Delta x_{i,i-1}^2 + \Delta x_{i,i+1}^2}\,. \tag{3.24}$$

It ii easy to see that the approximations $\overline{u}_i^x$ and u_i^x of the first derivative for the linear and parabolic reconstruction are not equal. The equality occurs only for the special case of the equidistant mesh, where both formulas give the same expression as the central difference approximation (3.8).

3.1.5. Limiters for a piecewise parabolic reconstruction

Keeping the same logic as in the linear case, we present here limiters for the piecewise parabolic reconstruction.

Minmod (MM) limiter for the piecewise parabolic reconstruction [64] is done as sequential application of (3.9) starting with the second derivative

$${}^{m}u_i^{xx} = \operatorname{minmod}\left(\overline{u}_i^{xx}, \beta\frac{\overline{u}_{i+1}^x - \overline{u}_i^x}{\Delta x_{i,i+1}/2}, \beta\frac{\overline{u}_i^x - \overline{u}_{i-1}^x}{\Delta x_{i,i-1}/2}\right), \text{ with } \beta \in (1,2)\,.$$

If the limitation of the second derivative is not necessary (i.e. if ${}^{m}u_i^{xx} = \overline{u}_i^{xx}$), then we

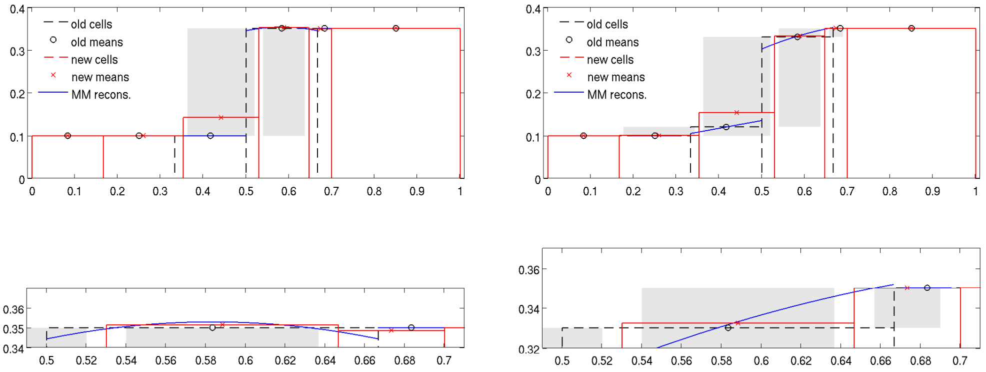

(a) (b)

Figure 3.3.: Single remap of a step (a) and smooth (b) function with the MM limited piecewise parabolic reconstruction. Old grid with the mean values (circles) is in black, new grid is in red. Reconstruction is plotted in blue, its bounds in gray. A zoom is provided in the smaller bottom figures.

set ${}^{m}u_i^x = \overline{u}_i^x$, otherwise

$$ {}^{m}u_i^x = \operatorname{minmod}\left(\overline{u}_i^x, \beta\frac{\overline{u}_{i+1}-\overline{u}_i}{\Delta x_{i,i+1}/2}, \beta\frac{\overline{u}_i-\overline{u}_{i-1}}{\Delta x_{i,i-1}/2}\right) . $$

The final formula for the minmod–limited piecewise parabolic reconstruction reconstruction is

$$ u_i^{\text{minmod}}(x) = \overline{u}_i + {}^{m}u_i^x(x-x_i) + \frac{1}{2}\,{}^{m}u_i^{xx}\left[(x-x_i)^2 - \frac{1}{12}\Delta x_i^2\right] . \tag{3.25} $$

An example of the limiter behavior is plotted in Fig. 3.3.

Kuzmin–Barth–Jespersen (KBJ) limiter [65] for the piecewise parabolic reconstruction (Fig. 3.4) is based on the BJ limiter (3.13). The original limiter for the piecewise linear reconstruction can be expressed as a function BJ $(\overline{u}_{i-1}, \overline{u}_i, \overline{u}_{i+1}, \overline{u}_i^x, \Delta x_i)$ with the return value α_i. An example of the sequential application of the limiter, as it is described bellow,

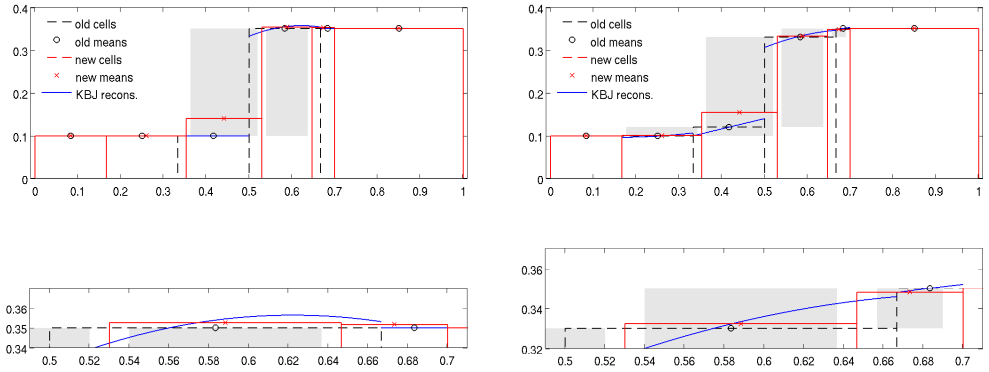

(a)

(b)

Figure 3.4.: Single remap of a step (a) and smooth (b) function with the KBJ limited piecewise parabolic reconstruction. Old grid with the mean values (circles) is in black, new grid is in red. Reconstruction is plotted in blue, its bounds in gray. A zoom is provided in the smaller bottom figures.

is plotted in Fig. 3.4

$$\begin{aligned}
\alpha_i^{xx} &= \mathrm{BJ}\left(\overline{u}_{i-1}^{x}, \overline{u}_i^{x}, \overline{u}_{i+1}^{x}, \overline{u}_i^{xx}, \Delta x_i\right) \\
\alpha_i^{xo} &= \mathrm{BJ}\left(\overline{u}_{i-1}, \overline{u}_i, \overline{u}_{i+1}, \overline{u}_i^{x}, \Delta x_i\right) \\
\alpha_i^{x} &= \max\left(\alpha_i^{xo}, \alpha_i^{xx}\right) \\
{}^{B}u_i^{xx} &= \alpha_i^{xx}\overline{u}_i^{xx} \\
{}^{B}u_i^{x} &= \alpha_i^{x}\overline{u}_i^{x} \\
u_i^{\mathrm{KBJ}}(x) &= \overline{u}_i + {}^{B}u_i^{x}(x - x_i) + \frac{1}{2}\,{}^{B}u_i^{xx}\left[(x - x_i)^2 - \frac{1}{12}\Delta x_i^2\right] .
\end{aligned} \tag{3.26}$$

Nejat limiter [66] for the piecewise parabolic reconstruction is expressed as

$$\sigma = \frac{1 - \tanh(S(\phi_0 - \phi_i))}{2},$$

with the constants $\phi_0 = 0.8$ and $S = 20$ as in the original thesis [66]. The limiter value ϕ_i is given by (3.15), resulting in the final formula

$$\begin{aligned}
{}^{N}u_i^{xx} &= \sigma\overline{u}_i^{xx} \\
{}^{N}u_i^{x} &= \left[(1 - \sigma)\phi_i + \sigma\right]\overline{u}_i^{x} \\
u_i^{\mathrm{Nejat}}(x) &= \overline{u}_i + {}^{N}u_i^{x}(x - x_i) + \frac{1}{2}\,{}^{N}u_i^{xx}\left[(x - x_i)^2 - \frac{1}{12}\Delta x_i^2\right] .
\end{aligned} \tag{3.27}$$

When used to solve the advection part of a hydrodynamic scheme, the smooth Nejat and the Venkatakrishnan extensions of the original Barth–Jespersen limiter generally show better results, introducing adjustable portion of numerical diffusion. On the contrary, this could be a disadvantage during the remapping stage, as we have no information on how to adjust their parameters. The remapping step does not need to be necessarily repeated after every time–step for the whole mesh, resulting in the different requirements for the limitation.

All the last three limiters applied to a piecewise parabolic reconstruction are suggested mainly to avoid numerical oscillations of the high–order schemes. In the original papers, the preservation of the local bounds is not addressed. Numerical examples of their performance are typically limited to equidistant meshes. In this thesis, we present a comparison of the limiters for a non–equidistant mesh during the remapping stage in the first section of the fifth chapter.

Piecewise Parabolic Method (PPM) [67] is well adapted in many hydrodynamic codes and is extendable to even higher order of accuracy [68]. This limiter satisfies the reconstruction bounds exactly. Another modification [37] have been developed to preserve smooth extrema, which is necessary to maintain its third order of accuracy. Unfortunately, this modification is applicable only for the equidistant meshes.

This method presents another option how to find appropriate reconstruction. Instead of searching second– and first–derivative approximations $\overline{u}^{xx}$ and $\overline{u}^{x}$ in the cell center, the parabolic reconstruction can be described by the value u^l at the left node $x_{i-1/2}$ and u^r at the right node $x_{i+1/2}$ of the cell i. A simple relation between these coefficients can by expressed

$$\begin{aligned}\overline{u}_i^x &= \frac{u_i^r - u_i^l}{\Delta x_i}\\ \overline{u}_i^{xx} &= 12\frac{(u_i^r + u_i^l)/2 - \overline{u}_i}{\Delta x_i^2}\,.\end{aligned} \tag{3.28}$$

The nodal approximations are calculated from a higher–order interpolant around the nodes and further modified to get a value bounded by the mean values in the surrounding cells:

$$\begin{aligned}u_{i+1/2} = \overline{u}_i &+ \frac{\Delta x_i}{\Delta x_i + \Delta x_{i+1}}(\overline{u}_{i+1} - \overline{u}_i) + \frac{1}{\Delta x_{i-1} + \Delta x_i + \Delta x_{i+1} + \Delta x_{i+1}}\times\\ &\times\left\{\frac{2\Delta x_{i+1}\Delta x_i}{\Delta x_i + \Delta x_{i+1}}\left[\frac{\Delta x_{i-1} + \Delta x_i}{2\Delta x_i + \Delta x_{i+1}} - \frac{\Delta x_{i+2} + \Delta x_{i+1}}{2\Delta x_{i+1} + \Delta x_i}\right](\overline{u}_{i+1} - \overline{u}_i) -\right.\\ &\left. - \Delta x_i\frac{\Delta x_{i-1} + \Delta x_i}{2\Delta x_i + \Delta x_{i+1}}\delta\overline{u}_{i+1} + \Delta x_{i+1}\frac{\Delta x_{i+1} + \Delta x_{i+2}}{\Delta x_i + 2\Delta x_{i+1}}\delta\overline{u}_i\right\}\,,\end{aligned} \tag{3.29}$$

where the average slope $\delta\overline{u}_i$ of the parabola in the cell i is approximated as

$$\delta\overline{u}_i = \begin{cases} 0 & \text{if } (\overline{u}_{i+1} - \overline{u}_i)(\overline{u}_i - \overline{u}_{i-1}) < 0\\ \min(|\Delta x_i \overline{u}_i^x|, 2|(\overline{u}_i - \overline{u}_{i-1})|, 2|(\overline{u}_{i+1} - \overline{u}_i)|)\cdot \operatorname{sign}(\Delta x_i \overline{u}_i^x) & \text{otherwise,}\end{cases} \tag{3.30}$$

where $\overline{u}_i^x$ in the previous expression comes from (3.21). This condition guarantees that $u_{i+1/2}$ stays in bounds of $\overline{u}_i$ and $\overline{u}_{i+1}$ and leads to a steeper representation of the shocks [67].

The whole PPM algorithm can be summarized as follows: Initialization of the one–side values at nodes $u_i^r = u_{i+1}^l = u_{i+1/2}$ as described above. To reduce the overshoots (the

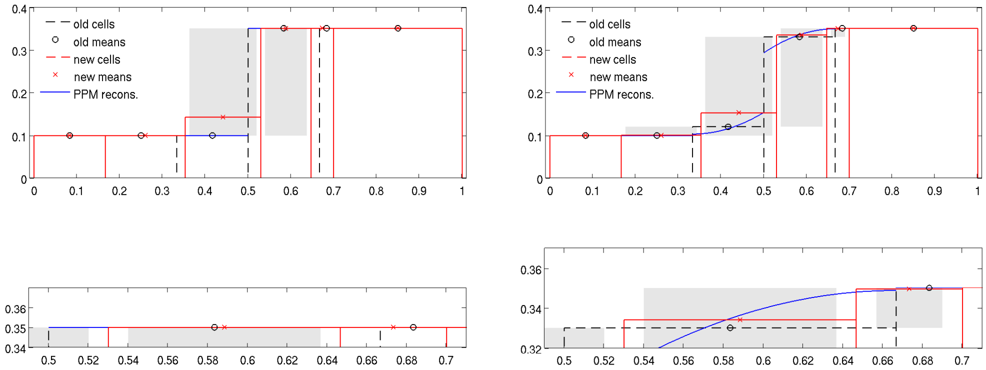

(a) (b)

Figure 3.5.: Single remap of a step (a) and smooth (b) function with the PPM piecewise parabolic reconstruction. Old grid with the mean values (circles) is in black, new grid is in red. Reconstruction is plotted in blue, its bounds in gray. A zoom is provided in the smaller bottom figures.

bounds violation by the reconstruction near discontinuities), another restrictions are applied. The restrictions represent the limiting process. If $\overline{u}_i$ is a local maximum/minimum, i.e. if

$$(u_i^r - \overline{u}_i)(\overline{u}_i - u_i^l) \leq 0\,,$$

then we set $u_i^r = u_i^l = \overline{u}_i$ to get a constant reconstruction in the cell. The last conditions guarantee the monotonicity of the reconstruction in the cell. If

$$(u_i^r - u_i^l)\left(\overline{u}_i - \frac{1}{2}(u_i^r + u_i^l)\right) > \frac{(u_i^r - u_i^l)^2}{6}$$

then we set $u_i^l = 3\overline{u}_i - 2u_i^r$. Similarly if

$$-\frac{(u_i^r - u_i^l)^2}{6} > (u_i^r - u_i^l)\left(\overline{u}_i - \frac{1}{2}(u_i^r + u_i^l)\right)$$

then $u_i^r = 3\overline{u}_i - 2u_i^l$. This gives us the final values. The final reconstruction formula for the piecewise parabolic reconstruction by the PPM method is obtained from (3.23) using the values provided by (3.28). Figure 3.5 presents an example of the reconstruction. Comparison of selected reconstructions for different functions is shown in Fig. 3.6. On the contrary to the previous methods (unlimited, MM– and KBJ–limited), the PPM method guaranties the bound preservation by its construction.

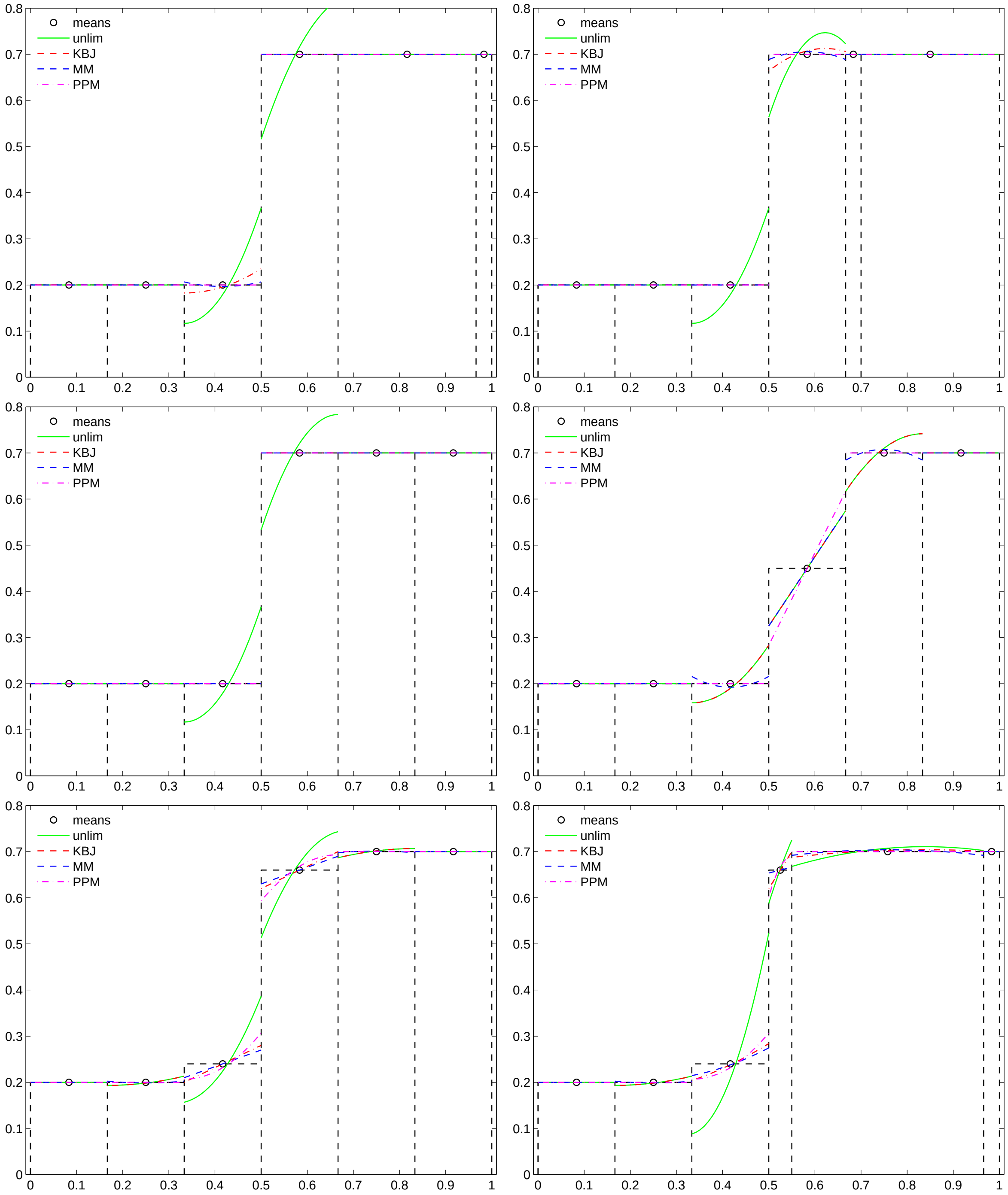

Figure 3.6.: 1D piecewise parabolic reconstructions with the different limiters for different mean values on different meshes.

The extension of remapping methods to higher (two and three) spatial dimensions is not straightforward. Both the limited reconstruction and quadrature become more complicated and novel approaches and ideas are needed to maintain required properties and computational efficiency. We describe first the reconstruction of a scalar quantity followed by its limitation.

3.2. 2D reconstruction of a scalar quantity

On the contrary to the one–dimensional case, we do not aim to derive analytical formulas for the piecewise polynomial reconstruction. Therefore, we start directly with the second–order piecewise quadratic reconstruction [9]. Lower–order methods are accessible through nullifying the high–order parts. The mean value (3.1) is extended to the form

$$\overline{u}_c = \frac{1}{V_c} \int\limits_{\Omega_c} u^R(y, x)\, \mathrm{d}x\, \mathrm{d}y \,, \tag{3.31}$$

where the computational cell c is defined by the polygon[3] Ω_c with the volume V_c.

3.2.1. Unlimited piecewise quadratic reconstruction

Further, deriving formulas for a quadratic reconstruction in a single cell, we omit the cell index c. According to a Taylor expansion, the quadratic reconstruction formula is

$$\begin{aligned} u^H(x, y) = \overline{u} - \lambda_0 + \lambda_1(x - x_c) + \lambda_2(y - y_c) + \lambda_3(x - x_c)^2 \\ + \lambda_4(x - x_c)(y - y_c) + \lambda_5(y - y_c)^2 \,, \end{aligned} \tag{3.32}$$

where x_c and y_c (defined below) represent the coordinates of the cell centroid and $\{\lambda_0, \ldots, \lambda_5\}$ is a set of unknown coefficients of the reconstruction. Similarly to (3.18), the first coefficient is derived from the requirement to preserve the mean value of the conservative quantity over a single cell

$$\lambda_0 = \lambda_3(x_s - x_c^2) + \lambda_4(z_c - x_c y_c) + \lambda_5(y_s - y_c^2) \,. \tag{3.33}$$

Definitions of the terms x_s, y_s, z_c are provided later in the final formulas for the remaining coefficients $\Lambda = (\lambda_1, \ldots, \lambda_5)^T$. The coefficients are calculated by minimization of the

---

[3] In most examples, the cells are quadrilaterals, but the method can be applied to other cell shapes.

reconstruction deviation functional in the surrounding cells

$$\sum_{k\in\mathcal{C}} \left(\overline{u}_k - \frac{1}{V_k} \int\limits_{\Omega_k} u^H(x,y)\,\mathrm{d}x\,\mathrm{d}y \right)^2 . \tag{3.34}$$

Here Ω_k stands for the area of the cell k with the volume V_k and $\mathcal{C}$ represents the set of n neighboring cells to the appointed cell. At least 5 neighboring cells are required to get a unique solution for Λ. Here, we choose 8 corner and edge neighbors for quadrilateral and edge neighbors for other polygonal meshes containing at least 5 edge neighbors (e.g. Voronoi meshes in [31]). The minimization process is equivalent to the solution of the following overdetermined linear system in the least square sense

$$\mathbb{A}\Lambda = \vec{B} \qquad \vec{B} = (\beta_1, \ldots, \beta_n)^T \qquad \mathbb{A} = \begin{pmatrix} \alpha_{1,1} & \cdots & \alpha_{1,5} \\ \vdots & \ddots & \\ \alpha_{n,1} & & \alpha_{n,5} \end{pmatrix} \tag{3.35}$$

with

$$\begin{aligned} \beta_k &= \overline{u}_k - \overline{u} \\ \alpha_{k,1} &= x_{c_k} - x_c \\ \alpha_{k,2} &= y_{c_k} - y_c \\ \alpha_{k,3} &= x_{s_k} - x_s + 2(x_c^2 - x_c x_{c_k}) \\ \alpha_{k,4} &= z_{c_k} - z_c + 2x_c y_c - x_{c_k} y_c - y_{c_k} x_c \\ \alpha_{k,5} &= y_{s_k} - y_s + 2(y_c^2 - y_c y_{c_k}) \, . \end{aligned}$$

The right hand side of the system consists of the differences from the mean values. The differences of the cell centroids x_c, y_c and x_{c_k}, y_{c_k} determine the first two columns of the matrix. The first two column sub–matrix can be used to obtain linear reconstruction in the cell. For the 1D case, the linear reconstruction follows exactly from the form (3.24). The centroid coordinates x_c, y_c of the cell and x_{c_k}, y_{c_k} of the adjacent cell k can be expressed thanks to the Green formula as integrals over the boundary between the cells.

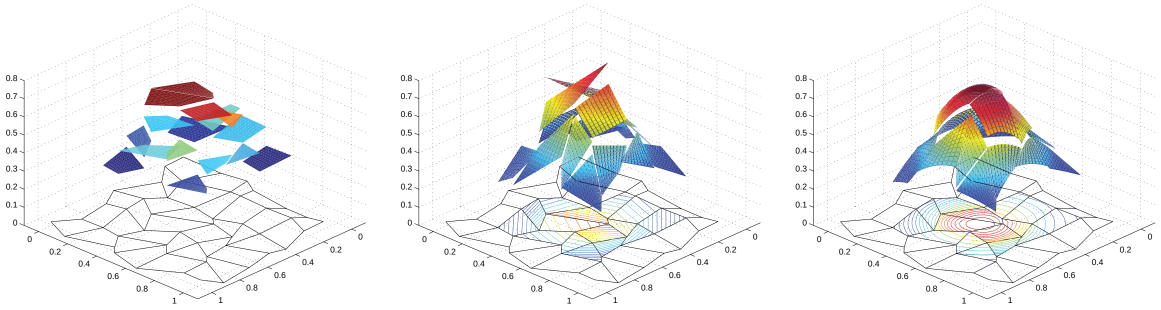

(a) (b) (c)

Figure 3.7.: Piecewise constant (a), linear (b) and quadratic (c) reconstruction over a general quadrilateral mesh (solid black line).

These boundary integrals take a simple form for the polynomial functions

$$x_c = \frac{1}{V}\int\limits_{\Omega} x\,\mathrm{d}V = \frac{1}{6V}\sum_{q\in\mathcal{P}}(x_q^2 + x_q x_{q-1} + x_{q-1}^2)(y_q - y_{q-1}) \tag{3.36}$$

$$y_c = \frac{1}{V}\int\limits_{\Omega} y\,\mathrm{d}V = -\frac{1}{6V}\sum_{q\in\mathcal{P}}(y_q^2 + y_q y_{q-1} + y_{q-1}^2)(x_q - x_{q-1})\,. \tag{3.37}$$

Here $\mathcal{P}$ is the set of all nodes of the selected cell and we assume (without the loss of generality) an ordering, which allows us to select the previous $(q-1)$ and the next $(q+1)$ point in this set in the counter-clockwise direction.

The elements in the remaining sub–matrix in (3.35), which define the second–order terms, can be expressed in the similar form

$$x_s = \frac{1}{V}\int\limits_{\Omega} x^2\,\mathrm{d}V = \frac{1}{12V}\sum_{q\in\mathcal{P}}(x_q + x_{q-1})(x_q^2 + x_{q-1}^2)(y_q - y_{q-1}) \tag{3.38}$$

$$y_s = \frac{1}{V}\int\limits_{\Omega} y^2\,\mathrm{d}V = -\frac{1}{12V}\sum_{q\in\mathcal{P}}(y_q + y_{q-1})(y_q^2 + y_{q-1}^2)(x_q - x_{q-1}) \tag{3.39}$$

$$\begin{aligned} z_c = \frac{1}{V}\int\limits_{\Omega} xy\,\mathrm{d}V = \frac{1}{24V}\sum_{q\in\mathcal{P}} \big[x_{q-1}^2(3y_{q-1} + y_q) + 2x_{q-1}x_q(y_{q-1} + y_{q-1}) + {} \\ + x_q^2(y_{q-1} + 3y_q)\big]\,(y_q - y_{q-1}) \end{aligned} \tag{3.40}$$

$$V = \int\limits_{\Omega} \mathrm{d}V = \frac{1}{2}\sum_{q\in\mathcal{P}}(x_q + x_{q-1})(y_q - y_{q-1})\,. \tag{3.41}$$

In the piecewise quadratic case, we use the Singular Value Decomposition (SVD) iterative numerical method to solve the least–square system (3.35). An illustrative comparison of the two dimensional piecewise polynomial reconstruction is plotted in Fig. 3.7.

3.2.2. Barth–Jespersen limiter

The Barth–Jespersen limiter for a piecewise linear reconstruction represents the standard limitation during the remapping stage in recent ALE codes. This limiter is used as a benchmark for our methods.

In the case of a linear reconstruction over a convex cell (we still omit the cell index here for simplicity), the extreme values are always achieved at the cell vertices. The reconstruction

$$u^H(x,y) = \overline{u} + \lambda_1(x - x_c) + \lambda_2(y - y_c)$$

is therefore, first extrapolated with the unlimited slopes

$$\lambda_1 = \left(\frac{\delta u}{\delta x}\right)^{\text{unlim}}, \ \lambda_2 = \left(\frac{\delta u}{\delta y}\right)^{\text{unlim}}$$

for all vertices $\vec{x}_n, n \in \mathcal{N}$ of the cell (in the same manner as 3.11)

$$u^u_n = u^u(\vec{x}_n) = \overline{u} + \lambda_1(x_n - x_c) + \lambda_2(y_n - y_c)\,. \tag{3.42}$$

The local bounds are computed as the min/max of the mean values over the neighboring cells (3 × 3 patch) around the particular cell. The computation of the unlimited slopes has been presented in the previous subsection. The final slopes, which are used for the numerical integration during remap, are then

$$\lambda_1 = \alpha\left(\frac{\delta u}{\delta x}\right)^{\text{unlim}}, \lambda_2 = \alpha\left(\frac{\delta u}{\delta y}\right)^{\text{unlim}}, \tag{3.43}$$

where the parameter α is calculated according to (3.13), where $u^u_{i,i\pm1/2}$ is replaced by u^u_n at each node. Instead of the minimum of the two nodal values $\alpha_i^{i\pm1/2}$ in 1D, we set α as the minimum of the all nodal values of the 2D computational cell.

This example of the BJ limiter for a piecewise linear reconstruction reveals the first difficulty of a high–order extension. The quadratic reconstructed function can reach extreme value within the computational cell. In the 1D case, the PPM method detects this situation and fix the slope to get a monotone (constant) reconstruction in the cell. In

2D, this process would require using a constrained optimization problem detection. This can be achieved with the Lagrange multiplier method but the solution is not obvious at all. A further motivation to avoid the reconstruction limiting is presented in the next sections.

3.3. 2D reconstruction of a vector

A straightforward extension of the reconstruction methods to vectors may consist in an application of the methods for each Cartesian component of the vector separately. However, e.g. the polar symmetry of a radial flow can be violated by such an extension [43].

The radial flows are of special importance for the ICF target design. Preservation of the spherical symmetry in compression of the ICF capsule is crucial to achieve ignition conditions. Therefore, a great care has to be taken to distinguish the physically relevant hydrodynamic instabilities from the numerical instability caused by inappropriate methods used in numerical simulations of the capsule compression. Our particular goal is to design new remapping methods, which are proven to preserve polar symmetry for radial vector fields.

3.3.1. Unlimited piecewise linear reconstruction

Here, we describe a cell–based unlimited piecewise linear reconstruction. An analogical reconstruction on a dual mesh for a staggered discretization is presented in [a2]. The reconstruction of the vector $\vec{w}$ in the computational cell c has the form

$$\vec{w}_c(\vec{x}) = \vec{w}_c + (\nabla \vec{w})_c (\vec{x} - \vec{x}_c)\,. \tag{3.44}$$

Here $\vec{x}_c$ denotes the cell centroid and $(\nabla \vec{w})_c$ an approximation of the gradient. An example of a constant and a linear vector reconstruction in a single cell is plotted in Fig. 3.8. The gradient approximation in the given cell c has the form

$$(\nabla \vec{w})_c = \begin{pmatrix} \frac{\delta w^x}{\delta x} & \frac{\delta w^x}{\delta y} \\ \frac{\delta w^y}{\delta x} & \frac{\delta w^y}{\delta y} \end{pmatrix}_c\,. \tag{3.45}$$

Instead of the least–square fitting formula (3.35) used in the case of the scalar quantity, the particular gradients can be derived from the mean value of the gradient over the computational cell. After analytical manipulation, a particular gradient component of

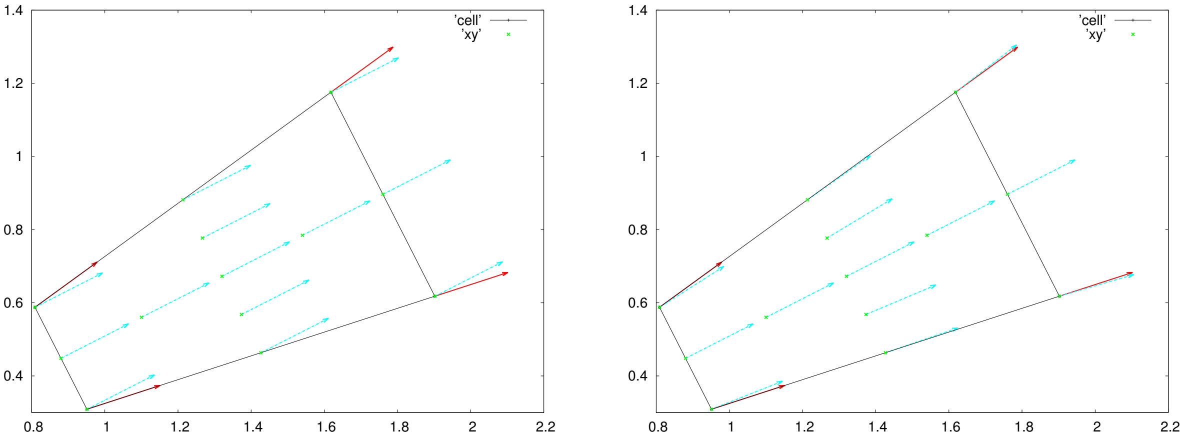

(a)

(b)

Figure 3.8.: Constant (a) and unlimited (b) linear reconstruction (blue) of a constant radial field (red) in a polar cell (black).

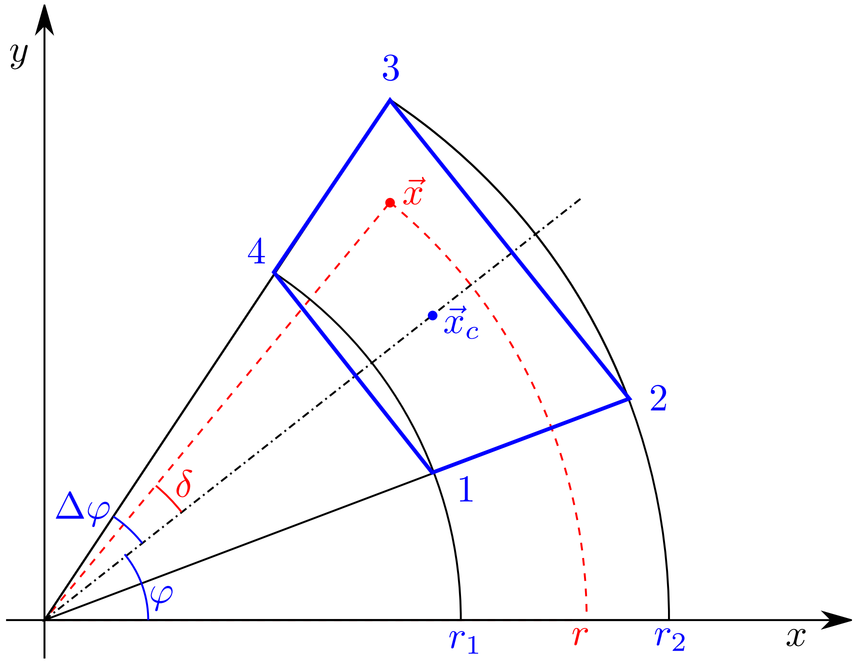

Figure 3.9.: Notation of nodes and angles for a polar cell.

the reconstructed function $f \in \{w^x, w^y\}$ can be expressed in the form

$$\begin{aligned}\oint_{\partial V_c} f \,\mathrm{d}y = \int_{V_c} \frac{\partial f}{\partial x}\,\mathrm{d}V \approx \frac{\partial f}{\partial x}\int_{V_c} \mathrm{d}V = \frac{\delta f}{\delta x}V_c \\ \frac{\delta f}{\delta x} = \frac{1}{V_c}\oint_{\partial V_c} f\,\mathrm{d}y \approx \frac{1}{V_c}\sum_{q\in\mathcal{P}(c)} \frac{f_{q+1}+f_q}{2}(y_{q+1}-y_q) = \frac{\delta f}{\delta x}\,,\end{aligned} \tag{3.46}$$

where V_c is the cell volume (3.41) and the summation (integration path) is done counter–clockwise around the cell[4] c, as indicated in Fig. 3.9. The derivative approximation with respect to y has the similar form

$$\frac{\delta f}{\delta y} = -\frac{1}{2V_c}\sum_{q\in\mathcal{P}(c)} (f_{q+1}+f_q)(x_{q+1}-x_q)\,. \tag{3.47}$$

Although the later formula for the gradient approximation is more suitable to analytically prove the symmetry of the calculated gradient than the solution of the two–column sub–matrix in (3.35), both methods can be used for remap providing comparable results.

Next, we derive analytical constraints for vector limiters, which are necessary to preserve the symmetry. For the particular polar cell indicated in Fig. 3.9 and for a symmetric radial vector field with the magnitude $W = |\vec{w}|$, the unlimited slopes are obtained through (3.46) and (3.47) as

$$\begin{aligned}\frac{\delta w^x}{\delta x} &= \frac{1}{r_2^2-r_1^2}\Big\{[W(r_2)+W(r_1)](r_2-r_1) + 2[W(r_2)r_1 - W(r_1)r_2]\cos^2\varphi\Big\} \\ \frac{\delta w^y}{\delta y} &= \frac{1}{r_2^2-r_1^2}\Big\{[W(r_2)-W(r_1)](r_2+r_1) + 2[W(r_1)r_2 - W(r_2)r_1]\cos^2\varphi\Big\} \\ \frac{\delta w^x}{\delta y} = \frac{\delta w^y}{\delta x} &= \frac{1}{r_2^2-r_1^2}\Big\{W(r_2)r_1 - W(r_1)r_2\Big\}\sin 2\varphi\end{aligned} \tag{3.48}$$

The derivative approximations (3.48) in the linear part of the reconstruction can be expressed in a more illustrative way. Multiplying the first terms in curly brackets by $1 = \sin^2\varphi + \cos^2\varphi$ and introducing the notation $\Delta W = W(r_2) - W(r_1)$, $\overline{W} = \frac{W(r_2)+W(r_1)}{2}$,

---

[4] The integration over cell vertices is useful for a staggered discretization. For a cell–centered discretization, the approximate integration can be performed over centroids of neighboring cells.

$\Delta r = r_2 - r_1$ and $\overline{r} = \frac{r_2+r_1}{2}$, we get

$$\begin{aligned}
\frac{\delta w^x}{\delta x} &= \frac{\Delta W}{\Delta r}\cos^2\varphi + \frac{\overline{W}}{\overline{r}}\sin^2\varphi \\
\frac{\delta w^y}{\delta y} &= \frac{\Delta W}{\Delta r}\sin^2\varphi + \frac{\overline{W}}{\overline{r}}\cos^2\varphi \\
\frac{\delta w^x}{\delta y} = \frac{\delta w^y}{\delta x} &= \left(\frac{\Delta W}{\Delta r} - \frac{\overline{W}}{\overline{r}}\right)\sin\varphi\cos\varphi\,.
\end{aligned}$$

These formulas correspond well to the analytical one, which can be expressed as $\frac{\partial}{\partial r} = \frac{\partial x}{\partial r}\frac{\partial}{\partial x} + \frac{\partial y}{\partial r}\frac{\partial}{\partial y}$ and $\frac{\partial}{\partial \varphi} = \frac{\partial x}{\partial \varphi}\frac{\partial}{\partial x} + \frac{\partial y}{\partial \varphi}\frac{\partial}{\partial y}$. The inverse relations are

$$\begin{aligned}
\frac{\partial}{\partial x} = \cos\varphi\frac{\partial}{\partial r} - \frac{\sin\varphi}{r}\frac{\partial}{\partial\varphi} &\to \frac{\partial w^x}{\partial x} = \frac{\partial W}{\partial r}\cos^2\varphi + \frac{W}{r}\sin^2\varphi \\
&\to \frac{\partial w^y}{\partial x} = \left(\frac{\partial W}{\partial r} - \frac{W}{r}\right)\sin\varphi\cos\varphi \\
\frac{\partial}{\partial y} = \sin\varphi\frac{\partial}{\partial r} + \frac{\cos\varphi}{r}\frac{\partial}{\partial\varphi} &\to \frac{\partial w^y}{\partial y} = \frac{\partial W}{\partial r}\sin^2\varphi + \frac{W}{r}\cos^2\varphi \\
&\to \frac{\partial w^x}{\partial y} = \left(\frac{\partial W}{\partial r} - \frac{W}{r}\right)\sin\varphi\cos\varphi\,.
\end{aligned}$$

To proof the symmetry of the linear part the high–order term $(\nabla\vec{w})_c(\vec{x} - \vec{x}_c)$ of the reconstruction (3.44), we rotate this term clockwise by an angle φ by the rotation matrix

$$\mathbb{R}^+ = \begin{pmatrix} \cos(\varphi) & \sin(\varphi) \\ -\sin(\varphi) & \cos(\varphi) \end{pmatrix}\,. \tag{3.49}$$

After some algebra, we get

$$\mathbb{R}^+(\nabla\vec{w})_c(\vec{x} - \vec{x}_c) = \begin{pmatrix} \frac{W(r_2)-W(r_1)}{r_2-r_1}\left[r\cos\delta - \frac{2}{3}\frac{r_1^2+r_1r_2+r_2^2}{r_1+r_1}\cos\Delta\varphi\right] \\ \frac{W(r_2)+W(r_1)}{r_2+r_1}r\sin\delta \end{pmatrix}\,. \tag{3.50}$$

To make this expression more clear, we introduce local cell coordinates $\vec{\eta} = \binom{\eta}{\xi}$. The first one, $\eta = r\cos\delta$, represents the radial and $\xi = r\sin\delta$ the angular direction given by the angle δ. The angles δ and $\Delta\varphi$ are explained in Fig. 3.9. Finally

$$\mathbb{R}^+(\nabla\vec{w})_c(\vec{x} - \vec{x}_c) = (\nabla\vec{w})_c^{\vec{\eta}}(\vec{\eta} - \vec{\eta}_c) = \begin{pmatrix} \frac{W(r_2)-W(r_1)}{r_2-r_1} & 0 \\ 0 & \frac{W(r_2)+W(r_1)}{r_2+r_1} \end{pmatrix}_c \begin{pmatrix} \eta - \eta_c \\ \xi \end{pmatrix}, \tag{3.51}$$

where η_c is a local coordinate of the cell centroid.

The formula (3.51) proves that the unlimited term is symmetric. We started with reconstruction from a general angle φ and the result is angle–independent. Symmetry of the reconstruction with respect to the cell axis is obvious e.g. for $\varphi = 0$. To conclude, the unlimited linear reconstruction preserves the radial symmetry for a radial flow on a equiangular polar mesh. Therefore, we focus on the limiters, whereas the symmetry violation originates.

3.3.2. Limitation of a piecewise linear reconstruction

The limited piecewise linear reconstruction with the unlimited gradient approximation $(\nabla\vec{w})_c$ (3.45) components given by (3.46) and (3.47) has the general form

$$\vec{w}_c(\vec{x}) = \vec{w}_c + \mathbb{L}_c(\nabla\vec{w})_c(\vec{x} - \vec{x}_c) \tag{3.52}$$

with the limiter matrix

$$\mathbb{L}_c = \begin{pmatrix} \Phi_c^{xx} & \Phi_c^{xy} \\ \Phi_c^{yx} & \Phi_c^{yy} \end{pmatrix} . \tag{3.53}$$

Setting $\Phi_c^{xy} = \Phi_c^{yx} = 0$ and calculating remaining coefficients independently according to the scalar case is a standard way to limit vectors in many hydrodynamic codes.

To preserve the radial flow symmetry on a polar mesh, we need an aditional condition for the limiter matrix. For the specific cell c with the cell centroid $\vec{x}_c$ on the axis x, the gradient (3.45) has to have only diagonal components for the symmetric radial vector (velocity) field. To explain this, we express each Cartesian component of the linear part of the reconstruction (the linear part $(\nabla\vec{w})_c(\vec{x} - \vec{x}_c)$ is given by the gradient $(\nabla\vec{w})_c$) as the third coordinate above the Cartesian space (x, y). Now, the linear part of the reconstruction of the 2D vector is represented by two planes (one for each Cartesian coordinate) in this space. To keep the symmetry, the first plane associated with the y–component of the linear part of the velocity reconstruction has to intersect all points on the axis x, e.g. the cell centroid $\vec{x}_c$, where $(\nabla\vec{w})_c(\vec{x} - \vec{x}_c) = (\nabla\vec{w})_c(\vec{x}_c - \vec{x}_c) = 0$. For any other point on the axis x, the reconstructed y–component is anti–symmetric with respect to the axis for symmetric radial fields. On the contrary, the second reconstruction plane associated with the x–component has to be constant in the direction perpendicular to the axis for symmetric radial fields.

These conditions on the non–diagonal elements being equal to zero provide useful constraints for slope limiters. When we apply the limiter (3.53) to the gradient (3.45) (which was originally diagonal) rotated by the matrix $\mathbb{R}^+$ (3.49) to a general direction, we expect the gradient to remain diagonal after the rotation backwards by the matrix $\mathbb{R}^- = (\mathbb{R}^+)^\top$

$$\mathbb{R}^-\mathbb{L}_c\mathbb{R}^+(\nabla\vec{w})_c^{\vec{\eta}} = \mathbb{R}^- \begin{pmatrix} \Phi_c^{xx} & \Phi_c^{xy} \\ \Phi_c^{yx} & \Phi_c^{yy} \end{pmatrix} \mathbb{R}^+ \begin{pmatrix} \frac{\delta w^\eta}{\delta\eta} & 0 \\ 0 & \frac{\delta w^\xi}{\delta\xi} \end{pmatrix}_c . \tag{3.54}$$

This condition leads to the set of equations

$$(\Phi_c^{xx} - \Phi_c^{yy}) \sin\varphi\cos\varphi + (\Phi_c^{xy}\cos^2\varphi - \Phi_c^{yx}\sin^2\varphi) = 0 \tag{3.55}$$

$$(\Phi_c^{xx} - \Phi_c^{yy}) \sin\varphi\cos\varphi + (\Phi_c^{yx}\cos^2\varphi - \Phi_c^{xy}\sin^2\varphi) = 0 \tag{3.56}$$

with the solution

$$\Phi_c^{xy} = \Phi_c^{yx} = \frac{\Phi_c^{yy} - \Phi_c^{xx}}{2}\tan 2\varphi\,, \tag{3.57}$$

where φ is an angle of rotation. From the necessary condition (3.57) for the symmetry preservation, we immediately see, that the standard limiter form with $\Phi_c^{xy} = \Phi_c^{yx} = 0$ is symmetric only for $\Phi_c^{xx} = \Phi_c^{yy}$. To get a sufficient condition for the symmetry preservation, we need a frame–independent[5] definition of the limiter matrix (3.53).

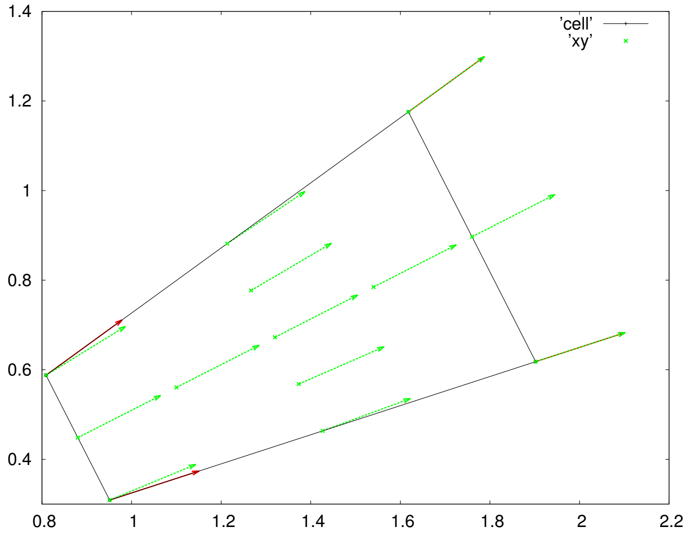

Figure 3.10.: Limited piecewise linear reconstruction (green) of a constant radial field (red) for a polar cell (black).

---

[5] angle–independent for the polar case

Here, we present a few of the frame–invariant definitions. The first method [45] is based on a local frame–invariant transformation of the reconstructed vector prior to the limiter application. For example, a rotation into the direction of the vector in the given cell is the frame invariant transformation. We use this transformation because of the close relation between the vector direction and limitation, which is useful to show properties of the limiter, namely the symmetry– and bound–preservation. In this case, the bounds for the vector $\vec{w}_c = \binom{w_c^x}{w_c^y}$ in the local (with respect to the cell c) coordinates ξ, η given by $\binom{\xi}{\eta} = \mathbb{R}_c^+ \binom{x}{y}$ are[6]

$$\begin{aligned} w_c^{\xi,\min} &= \min_{k \in \{\mathcal{C}(c),c\}} \left(\mathbb{R}_c^+ \vec{w}_k\right)^{\xi} \\ w_c^{\eta,\min} &= \min_{k \in \{\mathcal{C}(c),c\}} \left(\mathbb{R}_c^+ \vec{w}_k\right)^{\eta} \\ w_c^{\xi,\max} &= \max_{k \in \{\mathcal{C}(c),c\}} \left(\mathbb{R}_c^+ \vec{w}_k\right)^{\xi} \\ w_c^{\eta,\max} &= \max_{k \in \{\mathcal{C}(c),c\}} \left(\mathbb{R}_c^+ \vec{w}_k\right)^{\eta} \,. \end{aligned} \tag{3.58}$$

Minimization/maximization goes over the set $\mathcal{C}(c)$ of all neighboring cells, including the cell c. The rotation is realized thanks to the local rotation matrix

$$\mathbb{R}_c^+ = \frac{1}{|\vec{w}_c|} \begin{pmatrix} w_c^x & w_c^y \\ -w_c^y & w_c^x \end{pmatrix} \,. \tag{3.59}$$

The same transformation is used to project reconstructed values with the unlimited slopes at the cell vertices (3.42) and at the cell centers following the BJ limiter logic

$$\vec{w}_c^{u,\xi,\eta}(\vec{x}) = \mathbb{R}_c^+ \vec{w}_c^u(\vec{x}) \qquad\qquad \vec{w}_c^{\xi,\eta} = \mathbb{R}_c^+ \vec{w}_c(\vec{x})\,. \tag{3.60}$$

For each component of $\vec{w}_c^{u,\xi,\eta}(\vec{x})$, the BJ limiter (3.43) is applied to obtain the limiting coefficients α_c^{ξ} and α_c^{η}, each of them as in the scalar 2D case. Then, these coefficients are transformed back to the global Cartesian coordinate system. Following this way we obtain the limiter form suitable for the equation (3.52)

$$\mathbb{L}_c = \mathbb{R}_c^- \begin{pmatrix} \alpha_c^{\xi} & 0 \\ 0 & \alpha_c^{\eta} \end{pmatrix} \mathbb{R}_c^+ \,. \tag{3.61}$$

---

[6] note that these coordinates differ from ξ, η in (3.51)

The projection of the BJ limiter is simple and it does not introduce any significant computational cost. We clearly recommend an application of this modification whenever the vector limiting is necessary. Figure 3.10 presents an example of the limited vector reconstruction.

However, for a particular application, the limitation in the form (3.61) is not sufficient to preserve a specific bound. For a polar grid and a radial flow, this limiter does not preserve neither the maximal nor the minimal bound in the local radial component of the field. This is illustrated in Fig. 3.11 (a) and (d), where the bounds are plotted in the Cartesian space for a radial vector field. The bounds in the local radial component (d) are clearly more restrictive than the BJ bounds (a). The symmetry violation of the standard scalar (non–rotated) BJ limiter is evident for two locally identical cells with a different angular position in Fig. 3.11 (a), where a particular vector (denoted by a cross) with same relative position to both cells falls into the blue polygon but not into the red one.

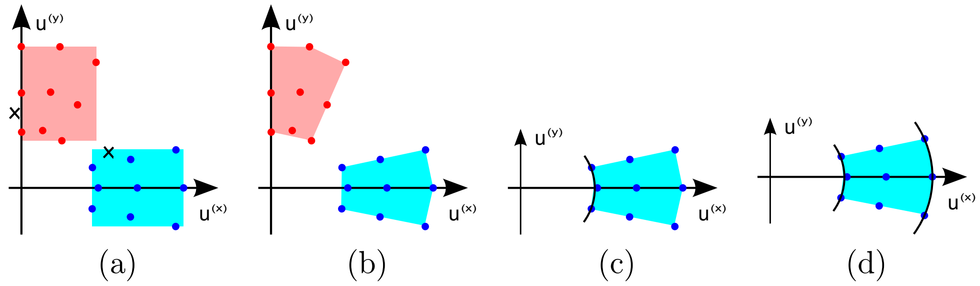

(a) (b) (c) (d)

Figure 3.11.: Bounds (from 3×3 stencil around the central cell c) for a vector reconstruction of: scalar extension of the BJ limiter (a), VIP limiter (b), MVIP limiter and an exact spherical limiter (d). The two identical cells with a different angular position (red and blue). Plot axes are the vector components $\vec{w} = \binom{u^{(x)}}{u^{(y)}}$.

The importance of the application of a symmetric min/max (3.58) is demonstrated in subsection 5.2.1 for the polar 2D Sedov hydrodynamic test case on a polar grid, where a non–symmetric limitation of the velocity vector during remap introduces artificial velocity oscillations.

3.3.3. Vector Image Polygon (VIP) limiter

The Vector Image Polygon (VIP) method [43] is an example of a more restrictive limiter. A graphical representation of the VIP limiter in the space of the vector field components is provided in Fig. 3.11 (b). The min/max (bounds) of the BJ limiter, as well as the limiter's projected form, are represented by a rectangle in the space in Fig. 3.11 (a).

The rectangle is bounded by the vector field components in the 3×3 patch around the a given cell c. Now, if we construct a convex hull[7] of these vector field components, the hull always fits the rectangle. Therefore, the VIP limiter is more restrictive than BJ limiter and the slope given by the VIP limiter is always smaller then the slope given by the BJ limiter.

The definition of the bounds is only the first part of the limiting procedure. The second task is the definition of the limitation matrix coefficients (3.53). As it was proven before, the diagonal form of the matrix satisfies the symmetry requirement only for $\Phi_c^{xx} = \Phi_c^{yy}$. Therefore, we investigate the special form of the limiter matrix

$$\mathbb{L}_c = \phi_c \mathbb{I}\,, \tag{3.62}$$

where $\mathbb{I}$ is the identity matrix and ϕ_c is a common scalar value.

To state the VIP limitation more formally, we repeat the limitation procedure for the piecewise linear reconstruction (3.52) with the limiter matrix (3.53). The limited reconstruction in the cell vertices has a form

$$\vec{w}_{nc}^{\mathrm{lim}} = \vec{w}_c + \phi_c (\nabla \vec{w})_c (\vec{x}_n - \vec{x}_c)\,. \tag{3.63}$$

For every cell center $\vec{x}_c$, we want to find ϕ_c, so that the limited reconstructions at all nodes $n \in N(c)$ ($N(c)$ is the set of 4 nodes of the quadrilateral cell c) are kept inside the VIP bounds VIP_c of the cell c. We require

$$\forall n \in N(c) \quad \vec{w}_{nc}^{\mathrm{lim}} \in \mathrm{VIP}_c \tag{3.64}$$

where VIP_c represents the Convex Hull of the neighboring cell's velocities $\vec{w}_k$, $k \in C(c)$ ($C(c)$ is the set of 9 cells of the 3×3 path around the cell c).

At first for all nodes $n \in N(c)$, we find the maximal $\phi_c \in (0, 1)$, which keeps $\vec{w}_{nc}^{\mathrm{lim}}$ inside the VIP_c. Let us call these values ϕ_{nc}^{VIP} and $\vec{w}_{nc}^{\mathrm{VIP}}$. Having computed all ϕ_{nc}^{VIP} corresponding to $\vec{w}_{nc}^{\mathrm{VIP}}$, we set the final

$$\phi_c = \min_{n \in N(c)} \left(\phi_{nc}^{\mathrm{VIP}} \right)$$

---

[7] vector image polygon

minimum of the nodal values ϕ_{nc} which satisfy the condition (3.64). Computation of a particular ϕ_{nc}^{VIP} can be done in the following way.

We denote the unlimited linear part of the reconstruction at the node n

$$\vec{u}_{nc} = (\nabla \vec{w})_c (\vec{x}_n - \vec{x}_c)\,.$$

This vector is in the limits if it lies in the convex hull (CH) of the set

$$\mathrm{CH}\{\vec{w}_{c'c}, c' \in C(c)\} = P_c \qquad\qquad \vec{w}_{c'c} = \vec{w}_{c'} - \vec{w}_c\,.$$

The polygon P_c has one to 9 (for quadrilateral mesh) vertices depending on the vector field and the polygon always contains the origin $\vec{0}$. Examples of these polygons are plotted in Fig. 3.12. The zero vector represents the piecewise constant low–order reconstruction $\vec{w}_c(\vec{x}) = \vec{w}_c$. Because of the linear reconstruction inside the cell and because of the scalar limiter ϕ_{nc}, the achievable reconstructions are located on the line segment $(\vec{0}, \vec{u}_{nc})$. The set of possible limiter values is represented by an intersection of this line segment with the convex hull P_c, i.e. it is again a line segment $(\vec{0}, \vec{u}_{nc}^{\mathrm{VIP}})$, where $\vec{u}_{nc}^{\mathrm{VIP}}$ is the intersection of the segment $(\vec{0}, \vec{u}_{nc})$ with the P_c boundary. The best (least diffusive) limiter value ϕ_n^c, given by the bounds in the cell c, is the closest to the $\vec{u}_{nc}$ and corresponds to the intersection $\vec{u}_{nc}^{\mathrm{VIP}}$. The construction of the convex hull P_c can be avoided by the computation of all intersections of $(\vec{0}, \vec{u}_{nc})$ with all segments $(\vec{w}_{cc_1}, \vec{w}_{cc_2})$ for all pairs of cells $c_1, c_2 \in C(c)$. To get the best (highest) limiter ϕ_{nc}^{VIP} (corresponding to the intersection $\vec{u}_{nc}^{\mathrm{VIP}}$), the maximal limiter value from the computation of all these intersections is taken.

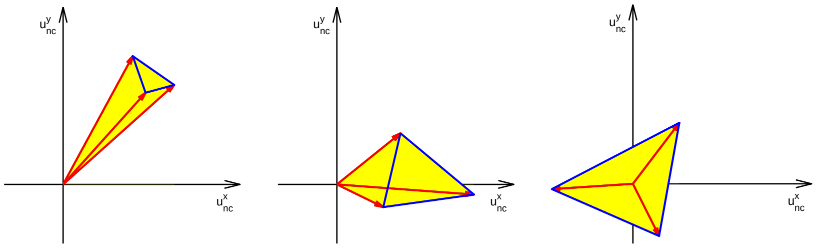

Figure 3.12.: Examples of three polygons P_c are plotted in yellow (these polygons are shifted from the polygons in Fig. 3.11). Red arrows represent the linear part of min/max velocities $\vec{w}_{c'c}$ and the segments $(\vec{w}_{cc_1}, \vec{w}_{cc_2})$ are in blue.

The limitation based on the piecewise linear reconstruction with the VIP limiter is perfectly symmetric for radial fields on polar meshes. However, there still might be a small violation of the lower bound for the radial component, while the preservation of the maximal bound is guaranteed by the definition of the VIP limiter. This undershoot is the main motivation for the suggested correction of vector bounds called Modified VIP (MVIP).

3.3.4. Modified VIP limiter

The Modified VIP limiter is constructed to add a new constraint (see Fig. 3.11 (c)) for the minimal vector magnitude, however, only in situations, where it is suitable. At first, suppose one–dimensional situation with only two vectors in the opposite directions having the same magnitude. In this case, the VIP set of these vectors is a line segment and after a restriction on the minimal magnitude (absolute value in 1D), it would not allow any contribution of the high–order part of piecewise linear reconstruction. However, standard limiters in 1D, e.g. (3.13) are applied for the value itself instead of its magnitude (absolute value), allowing the absolute value of limited reconstruction to be smaller than the absolute value in the neighboring nodes. The similar situation occurs in 2D when e.g. the origin of the coordinate system falls inside the CH of the vectors in the neighboring cell's. In this case, any restriction in on minimal vector magnitude does not make a good sense. Therefore, we choose the following condition for application of the minimal magnitude correction of VIP. If there exist any rotated coordinate system, in which all limiting vectors are located in one quadrant, then these vectors have a small angular discrepancy and the minimal magnitude condition is applied.

To compute the MVIP slope limiter, we extend the previous VIP algorithm. We evaluate the unlimited reconstruction in the cell nodes n and check the bounds for MVIP (instead of VIP (3.64))

$$\forall n \in N(c) \quad \vec{w}_{nc}^{\mathrm{lim}} \in \mathrm{MVIP}_c\,, \tag{3.65}$$

where

$$\mathrm{MVIP}_c = \begin{cases} \mathrm{VIP}_c \cap \mathrm{R}_c(0, \vec{w}^{\min}) & \text{for} \qquad \forall c_1, c_2 \in C(c),\ \vec{w}_{c_1} \cdot \vec{w}_{c_2} > 0 \\ \mathrm{VIP}_c & \qquad \text{otherwise}\,, \end{cases}$$

Here VIP_c represents the Convex Hull of cell velocities $\vec{w}_c$, $c \in N(c)$ and $\mathrm{R}_c(0, \vec{w}^{\min}) = \big\{\vec{w}, |w| \geq \min\limits_{k \in \{c, C(c)\}} (|\vec{w}_k|)\big\}$.

For a particular node n of the cell c, we find the maximal ϕ_{nc}^{VIP} as described in the previous section. For a vector field with a large angular discrepancy in the 3×3 patch around the cell c, $\mathrm{MVIP}_c = \mathrm{VIP}_c$ and therefore $\phi_{nc}^{\mathrm{MVIP}} = \phi_{nc}^{\mathrm{VIP}}$. Otherwise, we check if the limited vector $\vec{w}_{nc}^{\mathrm{VIP}}$ lies in MVIP_c and set

$$\phi_{nc}^{\mathrm{MVIP}} = \begin{cases} \phi_{nc}^{\mathrm{VIP}} & \text{for} \qquad \vec{w}_{nc}^{\mathrm{VIP}} \in \mathrm{R}_c(0, \vec{w}^{\min}) \\ \phi_{nc}^{i} & \text{otherwise}\,, \end{cases} \tag{3.66}$$

where ϕ_{nc}^{i} is the limiter value given by the intersection of the boundary of $\mathrm{R}_c(0, \vec{w}^{\min})$ (i.e. a circle) with the line segment $(\vec{w}_c, \vec{w}_{nc}^{\mathrm{VIP}})$. The particular reconstruction $\vec{w}_{nc}^{\mathrm{VIP}}$ is now clearly outside the $\mathrm{R}_c(0, \vec{w}^{\min})$ (i.e. inside the circle) and the mean value $\vec{w}_c \in \mathrm{R}_c(0, \vec{w}^{\min})$ (i.e. outside the circle). This implies that the intersection exists and is unique, $\phi_{nc}^{i} \in (0, \phi_{nc}^{\mathrm{VIP}})$ and finally $\vec{w}_{nc}^{\mathrm{lim}} \in \mathrm{MVIP}_c$.

In [a5], we describe the applications of the VIP limiter for the momentum remap in the staggered discretization, derive the MVIP limiter and demonstrate its performance on a set of cyclic remap [38] tests.

3.4. 1D remapping methods

In this section, the complete remapping algorithm including the calculation of numerical fluxes is described. Remap is a procedure how from the old integral averages (3.1), which are known, obtain the new integral averages (3.2) on the new rezoned mesh. Density $\overline{\rho}_i$ is an example of the integral average of a conservative quantity. Remap is easier to state in conservative quantities, which is mass in this case. The mass of the cell i in 1D is $M_i = \overline{\rho}_i \Delta x_i$. For a general distribution integral average, the old value of conservative quantity in the cell i in 1D is $Q_i = \overline{u}_i \Delta x_i$ and the flux form of the remap (2.4) can be written as (see fig. 3.1)

$$Q_i^n = Q_i + F_{i+1/2} - F_{i-1/2}\,. \tag{3.67}$$

In the section 3.1, several methods for the reconstruction of the distribution in 1D are described. The second part of the remapping algorithm is the computation of numerical fluxes through cell faces[8]. These fluxes are obtained by the integration of the reconstruction. Assuming a small displacement of the Lagrangian (old) and rezoned grids, the rezoned nodes of the new grid (marked with superscript n) stay inside two neighboring old cells, i.e. $x_{i-3/2} \le x_{i-1/2}^n \le x_{i+1/2}$, $\forall i$. In this case, the numerical fluxes F can be computed exactly for polynomial reconstruction. For a particular node motion to the

---

[8] nodes in 1D and edges in 2D

right, i.e $x^n_{i-1/2} \geq x_{i-1/2}$, we get

$$\begin{aligned} F_{i-1/2} &= \int\limits_{x_{i-1/2}}^{x^n_{i-1/2}} u^R_i(x)\,\mathrm{d}x = \int\limits_{x_{i-1/2}}^{x^n_{i-1/2}} a_i + b_i x + c_i x^2\,\mathrm{d}x = \\ &= \left(x^n_{i-1/2} - x_{i-1/2}\right)\left[a_i + b_i \frac{x^n_{i-1/2} + x_{i-1/2}}{2} + \frac{c_i}{3}\left({x^n_{i-1/2}}^2 + x^n_{i-1/2}x_{i-1/2} + {x_{i-1/2}}^2\right)\right], \end{aligned} \tag{3.68}$$

where we express the parabolic interpolant in the form $a_i + b_i x + c_i x^2$ for simplicity. The parabolic term is related to this form by

$$\begin{aligned} c_i &= \frac{1}{2}\overline{u}^{xx}_i \\ b_i &= \overline{u}^x_i - \overline{u}^{xx}_i x_i \\ a_i &= \overline{u}_i - \overline{u}^x_i x_i + \frac{1}{2}\overline{u}^{xx}_i\left(x_i^2 - \frac{1}{12}\Delta x_i^2\right) . \end{aligned}$$

For the nodal movement to the left, i.e. $x^n_{i-1/2} \leq x_{i-1/2}$, the numerical flux is

$$\begin{aligned} F_{i-1/2} &= \int\limits_{x_{i-1/2}}^{x^n_{i-1/2}} u^R_{i-1}(x)\,\mathrm{d}x = \int\limits_{x_{i-1/2}}^{x^n_{i-1/2}} a_{i-1} + b_{i-1} x + c_{i-1} x^2\,\mathrm{d}x = \\ &= \left(x^n_{i-1/2} - x_{i-1/2}\right) \times \\ &\times \left[a_{i-1} + b_{i-1} \frac{x^n_{i-1/2} + x_{i-1/2}}{2} + \frac{c_{i-1}}{3}\left({x^n_{i-1/2}}^2 + x^n_{i-1/2}x_{i-1/2} + {x_{i-1/2}}^2\right)\right] . \end{aligned} \tag{3.69}$$

The conservative quantity in the cell i has the form $Q_i = \overline{u}_i \Delta x_i$. To stay conservative (3.3), the value $\overline{u}^n_i$ in a new cell is equal to the sum of the old u_i and the difference[9] of the numerical fluxes, as indicated in Fig. 3.1. Supposing rigid boundary nodes, i.e. $x_{1/2} = x^n_{1/2}$ and $x_{N+1/2} = x^n_{N+1/2}$, the corresponding boundary numerical fluxes are zero. By a simple rearrangement of the formula, we get the remapped values $\overline{u}^n$ on the new grid

$$\begin{aligned} \overline{u}^n_i \Delta x^n_i &= \overline{u}_i \Delta x_i + F_{i+1/2} - F_{i-1/2} \\ \overline{u}^n_i &= \overline{u}_i \frac{\Delta x_i}{\Delta x^n_i} + \frac{F_{i+1/2} - F_{i-1/2}}{\Delta x^n_i} . \end{aligned} \tag{3.70}$$

---

[9] In 1D, we denote the fluxes positive if they are in the direction of the x axis.

The formula (3.70) together with the numerical fluxes (3.68) and (3.69) provide the final form of a remapping method using a piecewise constant, linear or parabolic reconstruction.

The remapping process can be further extended. Significant properties of the reconstruction are the conservativity and the bound preservation (3.6). Similar properties can be defined for the whole remapping process. The conservativity is then a direct consequence of the numerical fluxes (2.4) form of the remap. Bounds for the remapped function $\overline{u}_i^n$ are defined by values $\overline{u}_{i-1}$, $\overline{u}_i$ and $\overline{u}_{i+1}$ (3.4).

The bounds preservation can be enforced by another methods. For example, the so called repair [69, 70], where the out of bounds quantity is redistributed to the neighboring cells. Another possibility is the FCR method. The method uses a convex combination of a low– (piecewise constant reconstruction based) and high–order (unlimited piecewise linear or parabolic reconstruction based) numerical fluxes to preserve the high order of convergence on a smooth solution and to keep it in bounds near discontinuities. A multidimensional FCR method is described the next section directly for two spatial dimensions.

3.5. 2D remapping methods for a scalar

An exact integration of the reconstruction over the rezoned mesh displacement is computationally expensive. This is mainly due to the costly calculation of many possible intersections of the mesh cells. In order to avoid the calculation of the intersections of the old and new cells, the swept–area based method [40] uses an integration over the areas given by the mesh displacement, as indicated in Fig. 3.13.

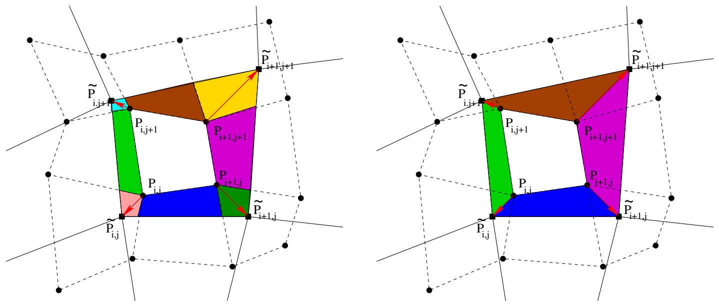

(a) (b)

Figure 3.13.: Exact (a) and swept (b) regions for the numerical fluxes quadrature. The dashed line denotes a Lagrangian– and the full line a rezoned–mesh [71]. The red arrows mark the movement of the mesh nodes during the rezone.

Thanks to its simplicity, computational efficiency and accuracy preservation, the swept–area method is widely applied during the remapping step with the piecewise linear BJ limited two dimensional reconstruction. However, a bound–preserving reconstruction does not imply the bound preservation of the remapped quantities in this case. To avoid a non–physical[10] repair technique, we prefer application of the FCR (2.5) idea. Contrary to the repair, the FCR method is local and compromises only between the two numerical fluxes obtained by two different methods.

3.5.1. Flux Corrected Remapping

Regardless to a particular numerical flux calculation method, suppose that we know the numerical fluxes F_{ik} from the cell i to the cell k of a particular conservative quantity Q. The remapped quantity $\tilde{Q}$ has the form (2.4). Or, we can rewrite the formula for the mean of conservative quantity distribution of the $u_i = Q_i/V_i$ and $\tilde{u}_i = \tilde{Q}_i/\tilde{V}_i$ in the cell[11] i with the volume of the Lagrangian cell V_i (3.41) and the rezoned cell $\tilde{V}_i$

$$\tilde{u}_i = \frac{1}{\tilde{V}_i}\left(u_i V_i + \sum_k F_{ik}\right) . \tag{3.71}$$

According to the particular numerical flux calculation method, the summation goes over all edge–neighboring cells $\mathcal{E}(i)$ (swept–based approach) or the node–neighbors $\mathcal{N}(i)$ (exact integration).

The FCR bounds are defined for the distribution of the conservative quantity

$$u_i^{\min} \leq \tilde{u}_i \leq u_i^{\max} \tag{3.72}$$

$$u_i^{\min} = \min_{k\in\{i,\mathcal{C}(i)\}}(u_k) \qquad u_i^{\max} = \max_{k\in\{i,\mathcal{C}(i)\}}(u_k) \qquad \mathcal{C}(i) = \mathcal{E}(i) \cup \mathcal{N}(i)\,. \tag{3.73}$$

Starting with the maximal bound and substituting (3.71) and (2.5) into (3.72), we derive

---

[10] We call this additional step of a remapping method non–physical because there is no physical reason to introduce additional redistribution of the interpolated quantities.

[11] In 2D case, we omit writing the line over mean values and replace the superscript n by tilde for remapped quantity to distinguish from 1D case.

the FCR constraints

$$\begin{aligned} u_i^{\max} &\geq \tilde{u}_i \\ u_i^{\max}\tilde{V}_i &\geq \tilde{u}_i\tilde{V}_i = \underbrace{u_iV_i + \sum_k \big(F_{ik}^L}_{\tilde{U}_i^L} + C_{ik}dF_{ik}\big) . \end{aligned}$$

The anti–diffusive flux $dF_{ik} = F_{ik}^H - F_{ik}^L$ is given by the low–order flux F_{ik}^L using the piecewise constant reconstruction and by the high–order flux F_{ik}^H using the piecewise parabolic (or piecewise linear) reconstruction.

$$\begin{aligned} u_i^{\max}\tilde{V}_i - \tilde{U}_i^L &\geq \sum_k C_{ik}dF_{ik} \\ u_i^{\max}\tilde{V}_i - \tilde{U}_i^L &\geq \sum_{k,dF_{ik}>0} C_{ik}dF_{ik} + \sum_{k,dF_{ik}<0} C_{ik}dF_{ik} \end{aligned}$$

The key points of the derivation are: the neglecting of the negative contributions $\sum\limits_{k,dF_{ik}<0} C_{ik}dF_{ik}$ in the sum on the right hand side

$$u_i^{\max}\tilde{V}_i - \tilde{U}_i^L \geq \sum_{k,dF_{ik}>0} C_{ik}dF_{ik}$$

and the factoring of the coefficients $C_{ik} \in (0,1)$ in front of the sum (both to handle a worst–case FCR scenario) to obtain

$$C_{ik} \leq D_i^{\max} = \frac{u_i^{\max}\tilde{V}_i - \tilde{U}_i^L}{\sum\limits_{k,dF_{ik}>0} dF_{ik}} . \tag{3.74}$$

For every cell i, we have now the sufficient condition for its numerical fluxes $C_{ik} \leq D_i^{\max}$. The minimal constraint is derived in the very similar way

$$\begin{aligned} u_i^{\min} &\leq \tilde{u}_i \\ u_i^{\min}\tilde{V}_i &\leq \tilde{u}_i\tilde{V}_i = \underbrace{u_iV_i + \sum_k \big(F_{ik}^L}_{\tilde{U}_i^L} + C_{ik}dF_{ik}\big) \end{aligned}$$

$$
\begin{aligned}
&\tilde{U}_i^L - u_i^{\min}\tilde{V}_i \geq -\sum_k C_{ik} dF_{ik} \\
&\tilde{U}_i^L - u_i^{\min}\tilde{V}_i \geq -\left(\sum_{k, dF_{ik}>0} C_{ik} dF_{ik} + \sum_{k, dF_{ik}<0} C_{ik} dF_{ik} \right) \\
&\qquad\qquad\qquad \Uparrow \\
&\tilde{U}_i^L - u_i^{\min}\tilde{V}_i \geq - \sum_{k, dF_{ik}<0} C_{ik} dF_{ik}
\end{aligned}
\tag{3.75}
$$

giving us the final condition on C_{ik}

$$
C_{ik} \leq D_i^{\min} = \frac{u_i^{\min}\tilde{V}_i - \tilde{U}_i^L}{\sum\limits_{k, dF_{ik}<0} dF_{ik}} \,. \tag{3.76}
$$

To satisfy all cell–based constraints (3.74) and (3.76) at the interface between two cells i and k, we set

$$
C_{ik} = \min\left(D_i^{\min}, D_i^{\max}, D_k^{\min}, D_k^{\max}\right) \,. \tag{3.77}
$$

So far, we did not discuss in detail the choice of the low– and high–order numerical fluxes F_{ik}^L and F_{ik}^H. To get the low–order fluxes, the piecewise constant reconstruction $u_i(x, y) = u_i$ in the cell i together with the exact integration would be appropriate. To avoid the calculation of cell intersections, we use a different form for the swept–based method

$$
u_{ij}^*(x, y) = \begin{cases} u_i \text{ for } V_{ij} > 0 \\ u_j \text{ for } V_{ij} < 0 \end{cases} , \tag{3.78}
$$

where $u_{ij}^*(x, y)$ represents the constant reconstruction for the particular swept flux $F_{ij} = u_{ij}^* V_{i,j}$ through the edge (i, j) and V_{ij} is the oriented volume of the swept area. For both methods with low–order fluxes and a small mesh displacement during the rezone, i.e. that the sum of absolute values of negative volume fluxes does not exceed the original cell volume [72], the remapped scalar quantity preserves bounds (3.72).

The same options are valid for the high–order numerical fluxes F_{ik}^H depending on the integration method. Up to the second–order piecewise quadratic reconstruction (3.32), the particular numerical flux has the form

$$F_{ik}^{H} = \int\limits_{\mathcal{S}} u^{H} \,\mathrm{d}V = \big[(\overline{u} - \lambda_0) + \lambda_1(x_c^{\mathcal{S}} - x_c) + \lambda_2(y_c^{\mathcal{S}} - y_c) + \lambda_3(x_s^{\mathcal{S}} - 2x_c^{\mathcal{S}} x_c + x_c^2) + \\ + \lambda_4(z_c^{\mathcal{S}} - y_c^{\mathcal{S}} x_c - x_c^{\mathcal{S}} y_c + x_c y_c) + \lambda_5(y_s^{\mathcal{S}} - 2y_c^{\mathcal{S}} y_c + y_c^2)\big]\, V^{\mathcal{S}} \,,$$

where the x_c, y_c are coordinates of the cell centroid and all other terms are given by the integral formulas (3.36 - 3.40) over the swept area $\mathcal{S}$ corresponding to the edge (i, k), e.g. $x_s^{\mathcal{S}} = \frac{1}{V^{\mathcal{S}}} \int_{\mathcal{S}} x^2 \,\mathrm{d}V$.

3.6. 2D remapping methods for a vector

Concerning vector remapping, the vector quantities for Euler equations are the velocity and momentum. Vectors are usually treated component by component. For the reconstruction, we showed that this component based treatment preserves the radial symmetry. The integration of the vector reconstruction is performed for each Cartesian component, introducing no new phenomena. All the methods described for a scalar in the previous section can be used here.

However, there are some differences. The bounds are typically no longer required for the momentum (volume density), but for the rotated velocity $\vec{u}$ components in the computational cell i

$$w_i^{\xi,\min} \le \tilde{\vec{u}}_i^{\xi} \le w_i^{\xi,\max}, \qquad w_i^{\xi,\min/\max} = \min_{k\in\{i,\mathcal{C}_i\}}/\max \left((\mathbb{R}_i \vec{u}_k)^{\xi} \right) \tag{3.79}$$

$$w_i^{\eta,\min} \le \tilde{\vec{u}}_i^{\eta} \le w_i^{\eta,\max}, \qquad w_i^{\eta,\min/\max} = \min_{k\in\{i,\mathcal{C}_i\}}/\max \left((\mathbb{R}_i \vec{u}_k)^{\eta} \right), \tag{3.80}$$

where the rotation matrix is given by (3.59) with respect to the velocity vector and the bounds are expressed in the local coordinates to preserve the symmetry. Also the FCR has to be performed in a frame–invariant way to preserve the symmetry, similarly to the methods addressed for the vector reconstruction in section 3.3.

3.6.1. Flux Corrected Remapping

Here, we describe the FCR methods for the momentum remap for a special case of the momentum flux given by the previously known mass flux multiplied by a velocity reconstruction at given point. Although the product form of the momentum flux is not necessary to the symmetry preserving FCR remap derivation, we use that form here with respect to possible applications. The form is useful e.g. for a particular implementation in the staggered discretization [a2], whereas here, we describe the method for the cell–centered discretization.

The remapped momentum in Cartesian coordinates is

$$\widetilde{m}_c\, \widetilde{\vec{w}}_c^{\,xy} = m_c\, \vec{w}_c^{\,xy} + \sum_{s\in\mathcal{S}(c)} \vec{F}_{c,s}^{\mu,\mathrm{FCR},xy},$$

where the flux is a combination of the low-order and high-order fluxes

$$\vec{F}_{c,s}^{\mu,\mathrm{FCR},xy} = \vec{F}_{c,s}^{\mu,\mathrm{L},xy} + C_{c,s}\, d\vec{F}_{c,s}^{\mu,xy}, \qquad\qquad d\vec{F}_{c,s}^{\mu,xy} = \vec{F}_{c,s}^{\mu,\mathrm{H},xy} - \vec{F}_{c,s}^{\mu,\mathrm{L},xy}.$$

We express the momentum flux as a product of (scalar) mass flux $F_{c,s}^m$ between cells c and s and the reconstructed velocity $\vec{w}_{c,s}$ in the particular flux position (the centroid of the swept region)

$$\vec{F}_{c,s}^{\mu,\mathrm{L},xy} = F_{c,s}^m\, \vec{w}_{c,s}^{\,\mathrm{L},xy}, \qquad \vec{F}_{c,s}^{\mu,\mathrm{H},xy} = F_{c,s}^m\, \vec{w}_{c,s}^{\,\mathrm{H},xy}, \qquad d\vec{F}_{c,s}^{\mu,xy} = F_{c,s}^m \left(\vec{w}_{c,s}^{\,\mathrm{H},xy} - \vec{w}_{c,s}^{\,\mathrm{L},xy}\right).$$

This particular flux form yields the FCR flux

$$\vec{F}_{c,s}^{\mu,\mathrm{FCR},xy} = F_{c,s}^m \,\left(\vec{w}_{c,s}^{\,\mathrm{L},xy} + C_{c,s}\left(\vec{w}_{c,s}^{\,\mathrm{H},xy} - \vec{w}_{c,s}^{\,\mathrm{L},xy}\right)\right)\,. \tag{3.81}$$

The remapped momentum is rotated to the (ξ,η) coordinates by

$$\mathbb{R}_c\left(\widetilde{m}_c\, \widetilde{\vec{w}}_c^{\,xy}\right) = \widetilde{m}_c\, \overbrace{\mathbb{R}_c\, \widetilde{\vec{w}}_c^{\,xy}}^{\widetilde{\vec{w}}_c^{\,\xi\eta}} = m_c\, \overbrace{\mathbb{R}_c\, \vec{w}_c^{\,xy}}^{\vec{w}_c^{\,\xi\eta}} + \sum_{s\in\mathcal{S}(c)} F_{c,s}^m \,\left(\mathbb{R}_c\, \vec{w}_{c,s}^{\,\mathrm{L},xy} + \mathbb{R}_c\, C_{c,s}\left(\vec{w}_{c,s}^{\,\mathrm{H},xy} - \vec{w}_{c,s}^{\,\mathrm{L},xy}\right)\right)\,.$$

giving the set of constraints (3.79) and (3.80) for the cell c multiplied by the remapped mass $\widetilde{m}_c$

$$\widetilde{m}_c w_c^{\xi,\min} \le m_c \overbrace{(\mathbb{R}_c \vec{w}_c^{\,xy})^{\xi}}^{w_c^{\xi}} + \sum_{s\in\mathcal{S}(c)} F_{c,s}^m \,\left(\mathbb{R}_c \vec{w}_{c,s}^{\,\mathrm{L},xy} + C_{c,s}\,\mathbb{R}_c\left(\vec{w}_{c,s}^{\,\mathrm{H},xy} - \vec{w}_{c,s}^{\,\mathrm{L},xy}\right)\right)^{\xi} \le \widetilde{m}_c w_c^{\xi,\max}, \tag{3.82}$$

$$\widetilde{m}_c w_c^{\eta,\mathrm{min}} \le m_c \underbrace{(\mathbb{R}_c \vec{w}_c^{xy})^\eta}_{w_c^\eta} + \sum_{s\in\mathcal{S}(c)} F^m_{c,s} \left(\mathbb{R}_c \vec{w}^{\mathrm{L},xy}_{c,s} + C_{c,s}\, \mathbb{R}_c \left(\vec{w}^{\mathrm{H},xy}_{c,s} - \vec{w}^{\mathrm{L},xy}_{c,s}\right)\right)^\eta \le \widetilde{m}_c w_c^{\eta,\mathrm{max}}. \tag{3.83}$$

The following point is to find the scalar flux correction factor $C_{c,s}$ for the each flux around the cell c. That is, to find the maximum possible $C_{c,s}$ that satisfies constraints (3.82) and (3.83) for the cell c and analogous constraints for the cell $s \in \mathcal{C}(c)$. Let us consider the constraints for the ξ-component of the momentum in the cell c (3.82). We reorder them and the define available range for the antidiffusive correction of the momentum Q at the lower and upper bound

$$\begin{aligned}
Q_c^{\xi,\mathrm{min}} &= \widetilde{m}_c\, w_c^{\xi,\mathrm{min}} - \widetilde{m}_c\, \widetilde{w}_c^{\xi,L} = \widetilde{m}_c\, w_c^{\xi,\mathrm{min}} - m_c\, w_c^\xi - \sum_{s\in\mathcal{S}(c)} F^m_{c,s} \left(\mathbb{R}_c\, \vec{w}^{\mathrm{L},xy}_{c,s}\right)^\xi \;\le\; 0,\\
Q_c^{\xi,\mathrm{max}} &= \widetilde{m}_c\, w_c^{\xi,\mathrm{max}} - \widetilde{m}_c\, \widetilde{w}_c^{\xi,L} = \widetilde{m}_c\, w_c^{\xi,\mathrm{max}} - m_c\, w_c^\xi - \sum_{s\in\mathcal{S}(c)} F^m_{c,s} \left(\mathbb{R}_c\, \vec{w}^{\mathrm{L},xy}_{c,s}\right)^\xi \;\ge\; 0,
\end{aligned}$$

where the inequalities (sign of Q) follow from the fact that the low-order momentum flux preserves the local bounds by construction. Now the constraint for the ξ-component becomes

$$Q_c^{\xi,\mathrm{min}} \;\le\; \sum_{s\in\mathcal{S}(c)} C_{c,s}\, F^m_{c,s} \left(\mathbb{R}_c \left(\vec{w}^{\mathrm{H},xy}_{c,s} - \vec{w}^{\mathrm{L},xy}_{c,s}\right)\right)^\xi \;\le\; Q_c^{\xi,\mathrm{max}} \tag{3.84}$$

and similarly for the η-component

$$Q_c^{\eta,\mathrm{min}} \;\le\; \sum_{s\in\mathcal{S}(c)} C_{c,s}\, F^m_{c,s} \left(\mathbb{R}_c \left(\vec{w}^{\mathrm{H},xy}_{c,s} - \vec{w}^{\mathrm{L},xy}_{c,s}\right)\right)^\eta \;\le\; Q_c^{\eta,\mathrm{max}}. \tag{3.85}$$

Let us denote

$$d\mu^\xi_{c,s} \;=\; F^m_{c,s} \left(\mathbb{R}_c \left(\vec{w}^{\mathrm{H},xy}_{c,s} - \vec{w}^{\mathrm{L},xy}_{c,s}\right)\right)^\xi, \tag{3.86}$$

$$d\mu^\eta_{c,s} \;=\; F^m_{c,s} \left(\mathbb{R}_c \left(\vec{w}^{\mathrm{H},xy}_{c,s} - \vec{w}^{\mathrm{L},xy}_{c,s}\right)\right)^\eta \tag{3.87}$$

and split the sums according to the sign of the terms $d\mu^\xi_{c,s}$, $d\mu^\eta_{c,s}$

$$Q_c^{\xi,\mathrm{min}} \quad\le\quad \sum_{s;\, d\mu^\xi_{c,s}>0} C_{c,s}\, d\mu^\xi_{c,s} + \sum_{s;\, d\mu^\xi_{c,s}<0} C_{c,s}\, d\mu^\xi_{c,s} \quad\le\quad Q_c^{\xi,\mathrm{max}},$$

$$Q_c^{\eta,\min} \quad \leq \quad \sum_{s;\, d\mu^{\eta}_{c,s}>0} C_{c,s}\; d\mu^{\eta}_{c,s} + \sum_{s;\, d\mu^{\eta}_{c,s}<0} C_{c,s}\; d\mu^{\eta}_{c,s} \quad \leq \quad Q_c^{\eta,\max}$$

The sufficient conditions for the bounds preservation, based on the worst case scenario, are

$$Q_c^{\xi,\min} \quad \leq \quad \sum_{s;\, d\mu^{\xi}_{c,s}<0} C_{c,s}\; d\mu^{\xi}_{c,s}, \tag{3.88a}$$

$$Q_c^{\xi,\max} \quad \geq \quad \sum_{s;\, d\mu^{\xi}_{c,s}>0} C_{c,s}\; d\mu^{\xi}_{c,s}, \tag{3.88b}$$

$$Q_c^{\eta,\min} \quad \leq \quad \sum_{s;\, d\mu^{\eta}_{c,s}>0} C_{c,s}\; d\mu^{\eta}_{c,s}, \tag{3.88c}$$

$$Q_c^{\eta,\max} \quad \geq \quad \sum_{s;\, d\mu^{\eta}_{c,s}<0} C_{c,s}\; d\mu^{\eta}_{c,s}, \tag{3.88d}$$

where the correction factor $C_{c,s}$ will be kept between 0 (low-order flux) and 1 (high-order flux), so it will not change the sign of the sums.

Now, we switch from the edge–related correction factors $C_{c,s}$ to the cell-related bounds D_c. Let us define $D_c^{\xi,\max}$ as

$$D_c^{\xi,\max} \quad = \quad Q_c^{\xi,\max} / \sum_{s;\, d\mu^{\xi}_{c,s}>0} d\mu^{\xi}_{c,s}.$$

Clearly, if the correction factors $C_{c,s}$ are chosen so that

$$0 \leq C_{c,s} \leq D_c^{\xi,\max} \qquad \text{for all } s \text{ such that} \quad d\mu^{\xi}_{c,s} > 0,$$

then (3.88b) holds, since

$$Q_c^{\xi,\max} \quad = \quad D_c^{\xi,\max} \sum_{s;\, d\mu^{\xi}_{c,s}>0} d\mu^{\xi}_{c,s} \quad = \quad \sum_{s;\, d\mu^{\xi}_{c,s}>0} D_c^{\xi,\max}\; d\mu^{\xi}_{c,s} \quad \geq \quad \sum_{s; d\mu^{\xi}_{c,s}>0} C_{c,s}\; d\mu^{\xi}_{c,s}.$$

Carrying out the same considerations for the other constraints, we have four quantities

D

$$
\begin{aligned}
D_c^{\xi,\min} &= Q_c^{\xi,\min} / \sum_{s;d\mu_{c,s}^{\xi}<0} d\mu_{c,s}^{\xi}, && (3.89a)\\
D_c^{\xi,\max} &= Q_c^{\xi,\max} / \sum_{s;d\mu_{c,s}^{\xi}>0} d\mu_{c,s}^{\xi}, && (3.89b)\\
D_c^{\eta,\min} &= Q_c^{\eta,\min} / \sum_{s;d\mu_{c,s}^{\eta}<0} d\mu_{c,s}^{\eta}, && (3.89c)\\
D_c^{\eta,\max} &= Q_c^{\eta,\max} / \sum_{s;d\mu_{c,s}^{\eta}>0} d\mu_{c,s}^{\eta} && (3.89d)
\end{aligned}
$$

with the following sufficient condition for the bounds preservation (3.88)

$$C_{c,s}^{c} \leq \min\left(D_c^{\xi,\min}, D_c^{\eta,\min}, D_c^{\xi,\max}, D_c^{\eta,\max}\right) . \tag{3.90}$$

We are now looking at the interface c and s, while and we know all necessary values of $\mathbb{R}$, $d\mu$, Q and D. To compute the final correction factor $C_{c,s}$, we use the minimum from the two cells c and s

$$C_{c,s} = \min\left(C_{c,s}^{c}, C_{c,s}^{s}\right) . \tag{3.91}$$

The described approach is symmetric for the radially symmetric velocity field on polar grids and preserves the local velocity bounds in the direction of the flow. However, the preservation of the local velocity bounds in directions ξ and η does not imply the preservation of the bounds in the radial velocity component. If there is a radial velocity field with a constant radial velocity component $W^{\xi} > 0$, the local bounds use a lower bound on $w^{\xi,\min} < W^{\xi}$, because the projection of the radial velocity from the neighboring cells (located off the axis ξ) to the direction ξ is strictly smaller than W^{ξ}.

3.7. Remap of conservative variables for Euler equations

As stated before, an exact integration of the reconstruction over the rezoned mesh displacement is computationally expensive. The second task is the preservation of bounds for density, velocity and specific internal energy. Concerning the conservation during a remapping step, the reconstruction has to be done for the distribution (volume density) of a conservative variable. For the mass, the distribution is density, which is a primitive variable. However, this is no more valid neither for the momentum nor for the total energy.

It is not obvious at all how to achieve the bound preservation during the remap concerning the Euler equations by the reconstruction limiting. That is why we focus here on the application of the FCR method to the whole system.

For the Euler hydrodynamic equations, the conservative quantities are the total mass $\sum_i M_i$, the total momentum components $\sum_i P_i^x$, $\sum_i P_i^y$ and the total energy $\sum_i E_i$. The conservation is enforced by the flux form of the remapped values

$$\tilde{Q}_i = Q_i + \sum_{k \in \mathcal{C}(i)} F_{ik}^Q \,. \tag{3.92}$$

Here $Q_i \in \{M_i, P_i^x, P_i^x, E_i\}$ represents the old mean cell quantity and F_{ik}^Q the corresponding numerical flux. Other remapped variables (lower–case) are defined as a combination of the conservative ones and the volume V_i of the cell i, that is, the mean cell density $\tilde{\rho}_i$, velocity $\tilde{\vec{u}}_i$, momentum $\tilde{\vec{\mu}}_i$, total energy $\tilde{e}_i$ and specific internal energy $\tilde{\epsilon}_i$

$$\tilde{\rho}_i = \tilde{M}_i/\tilde{V}_i \tag{3.93}$$

$$\tilde{\vec{u}}_i = \tilde{\vec{\mu}}_i/\tilde{\rho}_i = \tilde{\vec{P}}_i/\tilde{M}_i \tag{3.94}$$

$$\tilde{\epsilon}_i = \tilde{e}_i/\tilde{\rho}_i - \tilde{\vec{u}}_i^2/2 = \tilde{E}_i/\tilde{M}_i - \tilde{\vec{P}}_i^2/(2\tilde{M}_i^2) \,. \tag{3.95}$$

To be conservative, the reconstruction inside each cell is performed for the distributions of the conservative quantities $u_i \in \{\rho_i, \vec{\mu}_i, e_i\}$.

3.7.1. Flux Corrected Remapping

The application of the Flux Corrected Transport method during the remapping step of the ALE algorithm is reviewed in [52]. The remapped vector of the conservative quantities in the cell i has the form

$$\tilde{Q}_i = V_i u_i + \sum_{k \in \mathcal{C}(i)} F_{ik}^Q = Q_i + \sum_{k \in \mathcal{C}(i)} \Big[F_{ik}^{Q,L} + C_{ik} \underbrace{(F_{ik}^{Q,H} - F_{ik}^{Q,L})}_{dF_{ik}^Q} \Big] = Q_i^L + \sum_{k \in \mathcal{C}(i)} C_{ik} dF_{ik}^Q \,. \tag{3.96}$$

The summation goes over the set of all edge neighbors $\mathcal{C}(i)$, V_i represents the cell volume, Q_i^L the quantity remapped by a low–order method and dF_{ik}^Q the difference between high–

and low–order numerical fluxes, i.e. so called anti–diffusive flux.

There are different methods to compute the edge–based correction factors $C_{ik} \in [0,1]$ for the mass, momentum and total energy remap. In the 1D sequential FCR idea [51], the correction factor for the momentum remap C^{μ}_{ik} is expressed as $C^{\mu}_{ik} = C^{m}_{ik} C_{ik} < C^{m}_{ik}$ i.e. the correction factor for the mass remap and similarly $C^{E}_{ik} = C^{\mu}_{ik} C^{m}_{ik} C_{ik}$ for the energy remap. A local optimization procedure with a constrained minimization problem for each interface (i,k) is performed in the synchronized FCR [35, 52] method to get the optimal value of the independent coefficients $(C^{m}_{ik}, C^{\mu_x}_{ik}, C^{\mu_y}_{ik}, C^{E}_{ik})$ for the mass, the Cartesian momentum components and the energy simultaneously.

On the contrary, here we assume the same correction factors $C^{m}_{ik} = C^{\mu_x}_{ik} = C^{\mu_y}_{ik} = C^{E}_{ik} = C_{ik}$, because of a simple and efficient resolution of all constraints. We require a preservation of the bounds on the remapped density, components of velocity projected in the local flow direction (ξ, η) and specific internal energy

$$\rho_i^{\min} \le \tilde{\rho}_i \le \rho_i^{\max}, \qquad \rho_i^{\min/\max} = \min_{k\in\{i,\mathcal{C}(i)\}}/\max\,(\rho_k) \tag{3.97}$$

$$w_i^{\xi,\min} \le \left(\tilde{\vec{u}}_i\right)^{\xi} \le w_i^{\xi,\max}, \qquad w_i^{\xi,\min/\max} = \min_{k\in\{i,\mathcal{C}(i)\}}/\max\left(\left(\mathbb{R}_i \vec{u}_k\right)^{\xi}\right) \tag{3.98}$$

$$w_i^{\eta,\min} \le \left(\tilde{\vec{u}}_i\right)^{\eta} \le w_i^{\eta,\max}, \qquad w_i^{\eta,\min/\max} = \min_{k\in\{i,\mathcal{C}(i)\}}/\max\left(\left(\mathbb{R}_i \vec{u}_k\right)^{\eta}\right) \tag{3.99}$$

$$\epsilon_i^{\min} \le \tilde{\epsilon}_i \le \epsilon_i^{\max *}, \qquad \epsilon_i^{\min} = \min_{k\in\{i,\mathcal{C}(i)\}} (\epsilon_k) \tag{3.100}$$

$$\mathbb{R}_i = \frac{1}{|\vec{u}_i|}\begin{pmatrix} (\vec{u}_i)^x & (\vec{u}_i)^y \\ -(\vec{u}_i)^y & (\vec{u}_i)^x \end{pmatrix}, \qquad \epsilon_i^{\max *} = \max\left(\tilde{\epsilon}_i^{L}, \max_{k\in\{i,\mathcal{C}(i)\}} (\epsilon_k)\right). \tag{3.101}$$

Because of the form (3.95), even the internal energy $\tilde{\epsilon}_i^{L}$ remapped by a low–order method can exceed the maximum bound. Therefore, the greater term from the remapped value $\tilde{\epsilon}_i^{L}$ and the maximum over surrounding cells is taken in (3.101).

Thanks to (3.93), the local limiting coefficients for the density are the same as derived for a scalar case (3.74) and (3.76)

$$C_{ik} \le D_i^1 = \frac{\rho_i^{\min}\tilde{V}_i - \tilde{M}_i^{L}}{\sum\limits_{k\in\mathcal{C}(i)} \min\left(0, dF^{M}_{ik}\right)} \tag{3.102}$$

$$C_{ik} \le D_i^2 = \frac{\rho_i^{\max}\tilde{V}_i - \tilde{M}_i^{L}}{\sum\limits_{k\in\mathcal{C}(i)} \max\left(0, dF^{M}_{ik}\right)}, \tag{3.103}$$

where $\tilde{M}_i^L$ and dF_{ik}^M stand for the low-order remapped mass and the anti–diffusive mass flux.

Concerning the remap of momentum, we need to combine the mass fluxes F_{ik}^M and the corresponding remapped mass $\tilde{M}_i$ with the momentum fluxes $F_{ik}^{\vec{P}}$. For the minimum bound of the remapped momentum $\tilde{\mu}^\xi$ in the $\xi-$direction and for the $\xi-$velocity constraint (3.98), we obtain

$$\begin{aligned}
w_i^{\xi,\min} &\leq \left(\tilde{\vec{u}}_i\right)^\xi \\
w_i^{\xi,\min}\tilde{M}_i &\leq \tilde{P}_i^\xi \\
w_i^{\xi,\min}\left(\tilde{M}_i^L + \sum_{k\in\mathcal{C}(i)} C_{ik} dF_{ik}^M\right) &\leq \tilde{P}^{\xi,L} + \sum_{k\in\mathcal{C}(i)} C_{ik} dF_{ik}^{P\xi} \\
w_i^{\xi,\min}\tilde{M}_i^L - \tilde{P}^{\xi,L} &\leq \sum_{k\in\mathcal{C}(i)} C_{ik}\left(dF_{ik}^{P\xi} - w_i^{\xi,\min} dF_{ik}^M\right) .
\end{aligned}$$

The sufficient condition for the last equation is

$$C_{ik} \leq D_i^3 = \frac{w_i^{\xi,\min}\tilde{M}_i^L - \tilde{P}_i^{\xi,L}}{\sum\limits_{k\in\mathcal{C}(i)} \min\left(0, dF_{ik}^{P\xi} - w_i^{\xi,\min} dF_{ik}^M\right)} . \tag{3.104}$$

In a similar way, the next set of constraints is derived for the second inequality (3.98) and the η component (3.99)

$$C_{ik} \leq D_i^4 = \frac{w_i^{\xi,\max}\tilde{M}_i^L - \tilde{P}_i^{\xi,L}}{\sum\limits_{k\in\mathcal{C}(i)} \max\left(0, dF_{ik}^{P\xi} - w_i^{\xi,\max} dF_{ik}^M\right)} \tag{3.105}$$

$$C_{ik} \leq D_i^5 = \frac{w_i^{\eta,\min}\tilde{M}_i^L - \tilde{P}_i^{\eta,L}}{\sum\limits_{k\in\mathcal{C}(i)} \min\left(0, dF_{ik}^{P\eta} - w_i^{\eta,\min} dF_{ik}^M\right)} \tag{3.106}$$

$$C_{ik} \leq D_i^6 = \frac{w_i^{\eta,\max}\tilde{M}_i^L - \tilde{P}_i^{\eta,L}}{\sum\limits_{k\in\mathcal{C}(i)} \max\left(0, dF_{ik}^{P\eta} - w_i^{\eta,\max} dF_{ik}^M\right)} . \tag{3.107}$$

These constraints for the momentum are not the same as (3.89) derived for the symmetric FCR vector remap in section 3.6. In the previous method for a momentum vector, the remapped mass was supposed to be known prior to the remap of the momentum. Further, the remapped flux had a special form of the cell mass times the vector quantity. On the contrary, here we suppose the same correction factor C_{ik} for the mass and momentum remap, resulting in a different form of the FCR constraints.

Similarly to the velocity, the specific internal energy is not remapped directly. Starting from the required inequality (3.100), we get

$$\begin{aligned}\epsilon_i^{\min} &\leq \tilde{\epsilon}_i \\ \epsilon_i^{\min}\tilde{M}_i^2 &\leq \tilde{E}_i\tilde{M}_i - \frac{\left(\tilde{P}_i^{\xi}\right)^2 + \left(\tilde{P}_i^{\eta}\right)^2}{2}\,.\end{aligned}$$

Further, we use the formula (3.96) for the remapped mass, momentum and total energy

$$\begin{aligned}\epsilon_i^{\min}\left(\tilde{M}_i^L + \sum_k C_{ik} dF_{ik}^M\right)^2 \leq \left(\tilde{E}^L + \sum_k C_{ik} dF_{ik}^E\right)\left(\tilde{M}^L + \sum_k C_{ik} dF_{ik}^M\right) - \\ - \frac{1}{2}\left[\left(\tilde{P}^{\xi,L} + \sum_k C_{ik} dF_{ik}^{P^\xi}\right)^2 + \left(\tilde{P}^{\eta,L} + \sum_k C_{ik} dF_{ik}^{P^\eta}\right)^2\right]\end{aligned}$$

and after rearrangement, we get

$$\begin{aligned}&\epsilon_i^{\min}(\tilde{M}_i^L)^2 - \tilde{E}_i^L\tilde{M}_i^L + \frac{1}{2}\left[\left(\tilde{P}_i^{\xi,L}\right)^2 + \left(\tilde{P}_i^{\eta,L}\right)^2\right] \leq \\ &\leq \sum_k C_{ik}\Bigg[\underbrace{dF_{ik}^E\tilde{M}_i^L - dF_{ik}^{P^\xi}\tilde{P}_i^{\xi,L} - dF_{ik}^{P^\eta}\tilde{P}_i^{\eta,L} + dF_{ik}^M\left(\tilde{E}_i^L - 2\epsilon_i^{\min}\tilde{m}_i^L\right)}_{dF_{ik}^{de,\min}} + \\ &+ \sum_l C_{il}\underbrace{\left(dF_{ik}^E dF_{il}^M - \frac{1}{2}dF_{ik}^{P^\xi}dF_{il}^{P^\xi} - \frac{1}{2}dF_{ik}^{P^\eta}dF_{il}^{P^\eta} - \epsilon_i^{\min}dF_{ik}^M dF_{il}^M\right)}_{dF_{ikl}^{ds,\min}}\Bigg]\,.\end{aligned}$$

To get a sufficient condition for this inequality, we decrease the negative part (the positive part is neglected later) of the right–hand side by substituting $C_{il} = 1$ for negative terms in the inner sum and by neglecting the positive terms (in the inner sum).

$$\epsilon_i^{\min}(\tilde{M}_i^L)^2 - \tilde{E}_i^L\tilde{M}_i^L + \frac{1}{2}\left[\left(\tilde{P}_i^{\xi,L}\right)^2 + \left(\tilde{P}_i^{\eta,L}\right)^2\right] \leq \sum_k C_{ik}\left[dF_{ik}^{de,\min} + \sum_l \min\left(0, dF_{ikl}^{ds,\min}\right)\right],$$

which is translated via the worst case scenario into

$$C_{ik} \leq D_i^7 = \frac{\epsilon_i^{\min}(\tilde{M}_i^L)^2 - \tilde{E}_i^L \tilde{M}_i^L + \frac{1}{2}\left[\left(\tilde{P}_i^{\xi,L}\right)^2 + \left(\tilde{P}_i^{\eta,L}\right)^2\right]}{\sum\limits_{k \in \mathcal{C}(i)} \min\left(0, dF_{ik}^{de,\min} + \sum\limits_{l \in \mathcal{C}(i)} \min\left(0, dF_{ikl}^{ds,\min}\right)\right)} . \tag{3.108}$$

$$C_{ik} \leq D_i^8 = \frac{\epsilon_i^{\max *}(\tilde{M}_i^L)^2 - \tilde{E}_i^L \tilde{M}_i^L + \frac{1}{2}\left[\left(\tilde{P}_i^{\xi,L}\right)^2 + \left(\tilde{P}_i^{\eta,L}\right)^2\right]}{\sum\limits_{k \in \mathcal{C}(i)} \max\left(0, dF_{ik}^{de,\max} + \sum\limits_{l \in \mathcal{C}(i)} \max\left(0, dF_{ikl}^{ds,\max}\right)\right)} . \tag{3.109}$$

To conclude, knowing all the low–order remapped values of the mass $\tilde{M}_i^L$, radial $\tilde{P}_i^{\xi,L}$ and polar $\tilde{P}_i^{\eta,L}$ momentum components and total energy $\tilde{E}_i^L$; as well as corresponding anti-diffusive fluxes dF_{ik}^M, $dF_{ik}^{P^\xi}$, $dF_{ik}^{P^\eta}$, dF_{ik}^E, the FCR technique of substituting (3.96) into both sides of inequalities (3.97 – 3.100) with respect to (3.93 – 3.95) provides a set of cell-based constraints D_i^{1-8} (3.102 – 3.109).

The described FCT–based remapping method for the system of Euler equations is computationally efficient, only a summation of the earlier–calculated terms is required. Bounds preservation for the density, velocity and specific internal energy is guaranteed by the construction of the constraints. The ideas for the preservation of the radial symmetry are employed in the presented FCR method. The numerical performance of the method is demonstrated on a set of standard hydrodynamic test cases in subsections 5.2.2 – 5.2.5. Details of a particular application of our FCR method using piecewise quadratic reconstruction are presented in [a1].

4. Laser absorption modeling methods

In this chapter, a general description of the laser plasma interaction is supplemented by a presentation of the ray–tracing method for problems of a cylindrical symmetry and a discussion of the low–density foam modeling. These methods are applied to numerical simulations of experiments presented in the next chapter.

We use the CGS (centimeter, gram, second) system of physical units modified for the plasma, where the temperature is expressed in the electron–Volt equivalent instead of Kelvin. In difference from the standard SI units (kilogram, meter, second), the CGS system is widely used in hydrodynamic codes related to plasma physics. A list of all relevant physical constants in given in Tab. 4.1

physical constant	symbol	value and units
Boltzmann constant	k_B	$1.602 \cdot 10^{-12}$ erg/eV
reduced Planck const.	$\hbar$	$1.055 \cdot 10^{-27}$ erg·s
electron charge	e	$4.803 \cdot 10^{-10}$ statC
electron mass	m_e	$9.109 \cdot 10^{-28}$ g
speed of light	c	$2.998 \cdot 10^{10}$ cm/s

Table 4.1.: CGS physical constants.

In the final results, we recalculate the energy units to Joule, where 1 J = $1 \cdot 10^7$ erg and the laser intensity to common Watt per centimeter squared.

4.1. Laser plasma interaction

We start the description of the modeling of the laser light interaction with the simplest configuration, which is the ideal collisionless plasma. Then, we add the collision term to introduce the inverse–bremsstrahlung absorption, which is the main mechanism of the laser energy dissipation for given experimental conditions.

4.1.1. Propagation in collisionless plasma

In the simplest model, a propagation of the laser radiation with the angular frequency ω in a collisionless plasma is described by the dispersion relation

$$\omega^2 = \omega_p^2 + k^2 c^2 \,, \tag{4.1}$$

with the speed of light c and the wave vector $\vec{k}$. The plasma frequency ω_p, i.e. the frequency of the electron oscillations in a cold plasma with the electron density n_e, mass m_e and charge e, is determined by [20]

$$\omega_p = \sqrt{\frac{4\pi e^2 n_e}{m_e}} \quad [\mathrm{s}^{-1}] \,. \tag{4.2}$$

For the $\omega = \omega_p$ in (4.1), the wave vector $\vec{k}$ is equal to zero, defining the critical frequency ω_k. Laser radiation cannot propagate in a denser plasma because of the electron screening effect. The plasma frequency ω_p is a function of the free–electron density n_e. Therefore, for a given laser frequency f, the electromagnetic field can propagate in the plasma only for the density smaller the critical value. Concerning laser angular frequency $\omega = 2\pi f = 2\pi c/\lambda$ for the laser vacuum wavelength λ, we can write

$$\left(\frac{2\pi c}{\lambda}\right)^2 = \frac{4\pi e^2 n_e^{\mathrm{crit}}}{m_e}$$

providing the critical density of free electrons

$$n_e^{\mathrm{crit}} = \frac{m_e \pi c^2}{e^2 \lambda^2} \quad [\mathrm{cm}^{-3}]. \tag{4.3}$$

No dissipation processes are taken into account in this derivation, resulting in the reflection of the laser radiation. The plasma is a dielectric medium characterized by a permittivity ϵ given by

$$\epsilon = 1 - \frac{\omega_p^2}{\omega^2} = 1 - \frac{n_e}{n_e^{\mathrm{crit}}} \tag{4.4}$$

providing useful relations for the light refraction index n and the absorption index χ as the real and the imaginary part of the complex permittivity ϵ

$$n = \Re(\sqrt{\epsilon}) \text{ and } \chi = \Im(\sqrt{\epsilon}) \,. \tag{4.5}$$

4.1.2. Ray equation

A ray equation describes a propagation of the laser radiation in a plasma in the geometric optics approximation, neglecting the diffraction phenomena. The approximation is valid in a weakly inhomogeneous plasma with the characteristic density scale length much larger than the laser wavelength. The laser beam is presented as a bunch of thin rays each carrying out a small portion of the whole beam power. The propagation of each other separate ray is calculated independently to each other. The ray trajectory is determined by the refractive index n (4.5) according to the ray equation

$$\frac{\mathrm{d}}{\mathrm{d}s}\left(n\frac{\mathrm{d}\vec{r}}{\mathrm{d}s}\right) = \nabla n\,, \tag{4.6}$$

where r stands for the ray coordinate and $\frac{\mathrm{d}}{\mathrm{d}s}$ is the derivative along this trajectory.

According to (4.6), the trajectory is determined by plasma density variations and the angle of incidence of a laser beam on a plasma with respect to the plasma density gradient. For each ray, the initial spatial position and the direction of the ray on a plasma boundary (represented by the boundary of the computational domain) are given by spatial and angular profiles of the laser beam.

The ray equation (4.6) can be transformed to a system of ordinary differential equations, whereas standard numerical methods such as an explicit Runge–Kutta method can be applied to solve the problem. Let us define a unit vector in the ray direction in the spherical coordinates

$$\frac{\mathrm{d}\vec{r}}{\mathrm{d}s} = (\sin\theta\cos\phi, \sin\theta\sin\phi, \cos\theta)\,, \tag{4.7}$$

where θ is the polar angle with respect to the vertical axis z and ϕ is the azimuthal angle in the xy–plane. Then substituting this expression in (4.6), i.e. replacing the derivative with

$$\frac{\mathrm{d}}{\mathrm{d}s} = \frac{\mathrm{d}\theta}{\mathrm{d}s}\frac{\partial}{\partial\theta} + \frac{\mathrm{d}\phi}{\mathrm{d}s}\frac{\partial}{\partial\phi} + \frac{\mathrm{d}n}{\mathrm{d}s}\frac{\partial}{\partial n}$$

we get

$$\begin{aligned}
\frac{\partial n}{\partial x} &= n\cos\theta\cos\phi\frac{\mathrm{d}\theta}{\mathrm{d}s} - n\sin\theta\sin\phi\frac{\mathrm{d}\phi}{\mathrm{d}s} + \sin\theta\cos\phi\frac{\mathrm{d}n}{\mathrm{d}s}\\
\frac{\partial n}{\partial y} &= n\cos\theta\sin\phi\frac{\mathrm{d}\theta}{\mathrm{d}s} + n\sin\theta\cos\phi\frac{\mathrm{d}\phi}{\mathrm{d}s} + \sin\theta\sin\phi\frac{\mathrm{d}n}{\mathrm{d}s}\\
\frac{\partial n}{\partial z} &= -n\sin\theta\frac{\mathrm{d}\theta}{\mathrm{d}s} + \cos\theta\frac{\mathrm{d}n}{\mathrm{d}s}\,.
\end{aligned}$$

From these equations, we can eliminate the terms $\frac{\mathrm{d}n}{\mathrm{d}s}$. Expressing from the third equation

$$\frac{\mathrm{d}n}{\mathrm{d}s} = \frac{1}{\cos\theta}\left[\frac{\partial n}{\partial z} + n\sin\theta\frac{\mathrm{d}\theta}{\mathrm{d}s}\right] ,$$

we put the term into the remaining two equations. The acquired system can be transformed in two equations for the ray direction angles $\frac{\mathrm{d}\theta}{\mathrm{d}s}$ and $\frac{\mathrm{d}\phi}{\mathrm{d}s}$. Using (4.7), we can write the final system of ordinary differential equations

$$\begin{aligned}
\frac{\mathrm{d}x}{\mathrm{d}s} &= \sin\theta\cos\phi \\
\frac{\mathrm{d}y}{\mathrm{d}s} &= \sin\theta\sin\phi \\
\frac{\mathrm{d}z}{\mathrm{d}s} &= \cos\theta \\
\frac{\mathrm{d}\theta}{\mathrm{d}s} &= \frac{\cos\theta}{n}\left[\cos\phi\frac{\partial n}{\partial x} + \sin\phi\frac{\partial n}{\partial y}\right] - \frac{\sin\theta}{n}\frac{\partial n}{\partial z} \\
\frac{\mathrm{d}\phi}{\mathrm{d}s} &= \frac{1}{n\sin\theta}\left[\cos\phi\frac{\partial n}{\partial y} - \sin\phi\frac{\partial n}{\partial x}\right] .
\end{aligned} \tag{4.8}$$

4.1.3. Inverse bremsstrahlung absorption

For the investigated plasma parameters, the Coulomb collisions of plasma electrons and ions are the main absorption mechanism of the laser light. The bremsstrahlung is a radiation process induced by an accelerated charged particle. Similarly to the original X–radiation discovered when a linearly accelerated electron is stopped by heavy ions, the electron acceleration in a plasma is due to its Coulomb interaction with the plasma ions. The reverse process of the radiation energy transformation into the kinetic energy of plasma electrons, is called inverse bremsstrahlung.

Starting from the model of a cold plasma, where an electron is placed in a static ion background, we consider its motion in the oscillating laser electric field. By taking into account the deceleration of the electron given by an electron–ion collision frequency ν_{ei}, we can write the equation of the electron motion in the harmonic electric field of laser $\vec{E}_0\mathrm{e}^{-i\omega t}$

$$\frac{\mathrm{d}^2\vec{r}}{\mathrm{d}t^2} + \nu_{ei}\frac{\mathrm{d}\vec{r}}{\mathrm{d}t} = \frac{e}{m_e}\vec{E}_0\mathrm{e}^{-i\omega t} .$$

The coherent electron motion in the laser field produces an electric current which modifies the laser propagation. The electron collisions contribute to the complex permittivity ϵ of the plasma

$$\epsilon = 1 - \frac{\omega_p^2}{\omega^2 + \nu_{ei}^2} + i\frac{\nu_{ei}}{\omega}\frac{\omega_p^2}{\omega^2 + \nu_{ei}^2} \,. \tag{4.9}$$

Compared to (4.4) the imaginary part of ϵ is approximately proportional to the electron–ion collision frequency ν_{ei}.

The electron–ion collision frequency in an ideal high temperature plasma is described by the Spitzer formula [73]. For low electron temperatures T_e comparable to the Fermi energy $E_F = \frac{\hbar^2}{2m_e}\left(3\pi^2 n_e\right)^{2/3}$ the electrons are partially degenerate. An approximate expression for the electron–ion collision frequency, which is valid for a larger range of electron temperatures $k_B T_e \geq E_F$, reads:

$$\nu_{ei} = \frac{4}{3}\frac{\sqrt{2\pi}Z^2 e^4 n_i \ln\Lambda}{\sqrt{m_e}(k_B T_e + E_F)^{3/2}} \quad [\mathrm{s}^{-1}] \,, \tag{4.10}$$

with the electron density $n_e = Z n_i$, the ionization Z, the ion density $n_i = \frac{\rho}{A m_p}$, the mass density ρ, and the atomic number A. The Coulomb logarithm $\ln\Lambda$ can be expressed in the form

$$\ln\Lambda = \max[2, \ln\sqrt{b_{max}^2/b_{min}^2}] \,,$$

where $b_{max} = (k_B T_e/m_e)^{1/2}/\max[\omega_p, \omega]$ and $b_{min} = \max[Ze^2/k_B T_e, \hbar/(k_b T_e/m_e)^{1/2}]$ are the maximum and the minimum impact parameters in the electron–ion collision. According to (4.5), the permittivity determines both the laser ray propagation via the refraction index n and the laser absorption. The laser energy absorption along the ray trajectory is calculated from

$$\frac{\mathrm{d}Q}{\mathrm{d}s} = -\kappa_{\mathrm{ib}} Q \,, \tag{4.11}$$

where the absorption coefficient for the inverse bremsstrahlung κ_{ib} has the form

$$\kappa_{\mathrm{ib}} = \frac{2\omega}{c}\Im(\sqrt{\epsilon}) \,. \tag{4.12}$$

4.2. 3D ray–tracing method for 2D cylindrically symmetric codes

The physical relations describing the laser ray propagation and the energy deposition in plasma are derived in the previous section. Here, the issues specific for the energy deposition calculation in a 2D Lagrangian hydrodynamic code are addressed. An overview of a general ray–tracing algorithm is followed by the description of a particular implementation in the cylindrically symmetric hydrodynamic code PALE [21].

A fully 3D ray–tracing scheme [55] on unstructured grids composed of hexahedra, prisms, pyramids, and tetrahedra for the laser beam evolution is almost uniquely using in Lagrangian codes applied for modeling of a laser–produced plasma. The laser beam is represented by an ensemble of discrete rays propagating in a plasma according to the law of the geometrical–optics. The equations for the ray trajectory are integrated using a first– or a second–order approximation, which is exact for a constant density gradient. The ray–tracing method is based on the exact solution of the ray equation (4.6) inside each computational cell and the calculation of the ray refraction on the cells boundaries. The exact solution of the ray trajectory in a cell is a parabola assuming a constant density gradient. Applying the Snell law of refraction, the parabolas are linked together to form the complete ray trajectory inside a computational mesh. The energy deposition along the ray trajectory is calculated according to the equation (4.11). For the 2D Cartesian calculation in the PALE code, the Kaiser's method is directly applicable [20].

To initialize a ray–tracing algorithm, the incoming laser beam has to be split into separate rays, whereas each ray is defined by its spatial position and direction on a computational domain boundary.

For the 2D Cartesian case in the PALE code, spatial positions of the rays are initialized at the laser–irradiated mesh boundary, such as a fixed number of rays is equidistantly distributed along each cell boundary. Assuming the target location in the beam focal plane and the beam Rayleigh length much larger than the target size, the direction of each ray can be initialized parallel to the beam axis. For a general target and a single laser beam in the target symmetry axis (e.g. the double–foil target modeling [a4]), we initialize the ray according to the Gaussian beam model in the normal direction with respect to the local beam wavefront. In the latter case, an artificial diffractive was added to each ray in order to avoid non–physical focusing of the beam to a point or a caustic surface (Fig. 4.1) leading to a laser–intensity singularity. For all particular laser–target configurations, the

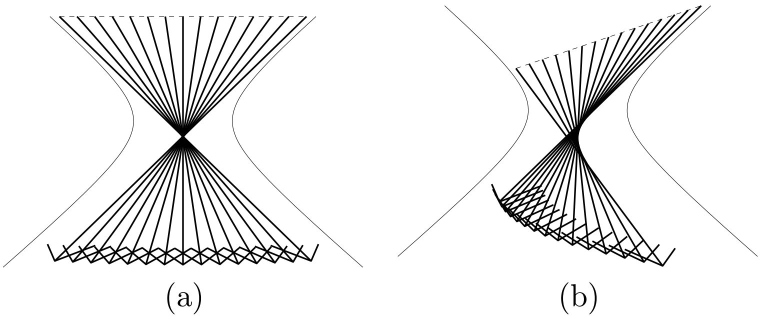
(a)
(b)

Figure 4.1.: Rays focusing to a point (a) and caustic surface (b) for the focused laser beam. Gaussian beam distribution at the computational domain boundary (dashed line).

ray–tracing calculation [20] can be performed on two–dimensional computational mesh for both Cartesian and cylindrical geometries in the PALE code providing a laser energy absorption on each time step.

4.2.1. Laser energy estimation along the beam axis

However, a special attention is needed for the calculation of the absorbed laser energy along the symmetry axis by 2D ray–tracing algorithms in 2D cylindrically–symmetric codes. This problem is addressed in [74] for a ray–tracing algorithm for the 2D Eulerian hydrodynamic code CRASH based on the direct numerical solution of the ODE's (4.8) in the whole computational domain instead of using the analytical solution inside each computational cell. The direct integration is more suitable for Cartesian rectangular grids because of a simple mapping of the ray trajectory into the regular domain and vice versa, i.e. simple evaluation of the refractive index everywhere inside the domain. The authors of Ref. [74] point out that for the laser ray, which is not pointing to the cylindrical axis of symmetry[1], an apparent reflection of the ray calculated with a 3D ray–tracing algorithm appears in the axi–symmetric target plane off the axis whereas the same ray calculated by a 2D ray–tracing always hit the axis.

Although the requirement for the 3D ray–tracing originates from the cylindrical symmetry violation of the laser–target setup, the 3D ray–tracing is useful even for the symmetric configurations of the PALS [6] laser, which are typically simulated by the 2D cylindrically–symmetric code PALE. Firstly, the artificial diffractive term can be replaced by a random deviation of the laser rays from the wave front normal in order to obtain

---

[1] These rays are typical for the beams that are not perfectly aligned with the target axis, e.g. the beams of recent multiple–beam ICF laser facilities.

in the focal plane the beam intensity distribution corresponding to experimental conditions. A random ray deviation is better applicable for general situations and it provides a physically–relevant far–field image of an object in focal plane. This method has been introduced in the 3D ray–tracing algorithm of the code PALE. Low–density foams with a random microscopic internal material structure present another example of the configuration, where the 3D ray–tracing method is needed. To simulate the microscopic foam inhomogeneities on macroscopic level, we introduce a random reflection of laser rays at the homogenization surface of the foam. Non–cylindrically–symmetric rays are introduced in both examples, requiring a 3D ray–tracing treatment of the laser energy deposition. The hydrodynamic motion remains axi–symmetric. The absorbed energy is averaged over the azimuthal angle so that the overall plasma dynamics is still described by the cylindrically–symmetric model.

4.2.2. 3D ray–tracing algorithm

The goal of this subsection is to introduce a computationally–efficient 3D ray–tracing algorithm for a 2D Lagrangian computational mesh supposing a cylindrical symmetry of the hydrodynamic flow. A direct application of the general 3D method [55] would require an additional discretization in the angular dimension, dramatically increasing the number of computational cells. Instead of this, we assume to have only one computational cell for all azimuthal angles to produce 3D mesh. The supposed 3D cell has a torus–like shape, whereas the original 2D computational cell defines the inner cross section of the torus. The number of conical faces of the 3D cell is equal to 2D cell's edge number. Supposing constant plasma parameters and thus a constant index of refraction n inside the cell, a straight–line solution of the ray–tracing equation 4.6 is obtained instantly

$$\begin{aligned}\frac{\mathrm{d}}{\mathrm{d}s}\left(n\frac{\mathrm{d}\vec{r}}{\mathrm{d}s}\right) &= 0\\ n\frac{\mathrm{d}\vec{r}}{\mathrm{d}s} &= \vec{d}\\ \vec{r} &= \vec{d}x + \vec{p},\end{aligned}$$

where $x = s/n$ in the line parameter and constant vectors $\vec{d} = (d_x, d_y, d_z)^T$, $\vec{p} = (p_x, p_y, p_z)^T$ are given by the conditions on the cell boundary. Although the piecewise line–trajectory rays are supposed to be inaccurate in the original paper [55], we adapt a different method [73] for the computation of the normal of the refractive surface on the cell faces, providing a sufficient precision in the energy deposition. This is illustrated in Fig. 4.2, where the piecewise line method is compared to the direct numerical solution of (4.8).

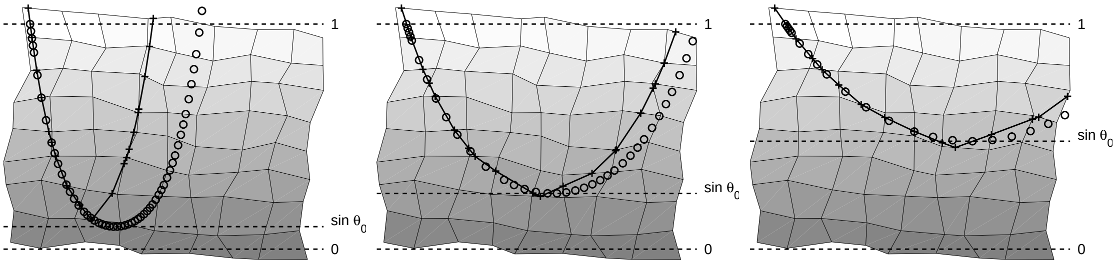

Figure 4.2.: Ray propagation calculated by the piecewise line ray–tracing (solid line) and by the direct numerical method (circle) for the different ray incidence angles $\theta_0 = \{0.1, 0.25, 0.5\}$ rad on a coarse random grid.

On the cell's boundaries, the rays with the incoming/outgoing direction $\vec{d}_{\text{in}}$, $\vec{d}_{\text{out}}$ are refracted according to the general Snell law for normalized (unit) vectors [55]

$$\vec{d}_{\text{out}} = \frac{n_{\text{in}}}{n_{\text{out}}} \left[\vec{n} \times \left(-\vec{n} \times \vec{d}_{\text{in}} \right) \right] - \vec{n} \sqrt{1 - \left(\frac{n_{\text{in}}}{n_{\text{out}}} \right)^2 (\vec{n} \times \vec{d}_{\text{in}}) \cdot (\vec{n} \times \vec{d}_{\text{in}})} \tag{4.13}$$

with the refractive index n_{in} in the cell, where the ray comes from and n_{out} in the next cell. Components of the vector of the refractive plane normal $\vec{n} = (n_x, n_y, n_z)^T$ before normalization are

$$\begin{aligned} N_x &= \nabla_R \frac{p_x}{\sqrt{p_x^2 + p_y^2}} \\ N_y &= \nabla_R \frac{p_y}{\sqrt{p_x^2 + p_y^2}} \\ N_z &= \nabla_Z \,, \end{aligned} \tag{4.14}$$

where $\vec{\nabla} = (\nabla_R, \nabla_Z)^T$ is the refractive index gradient (expressed in the cylindrical coordinates R, Z of the 2D code PALE) in the ray boundary intersection point $\vec{P} = (P_R, P_Z)^T = (\sqrt{p_x^2 + p_y^2}, p_z)^T$. The normalization is performed in the way to get a correct orientation of the refractive plane

$$\vec{n} = \begin{cases} \frac{\vec{N}}{|\vec{N}|} \text{ if } \vec{N} \cdot \vec{d}_{\text{in}} \leq 0 \\ \frac{-\vec{N}}{|\vec{N}|} \text{ if } \vec{N} \cdot \vec{d}_{\text{in}} > 0 \end{cases} .$$

The case where the square root in (4.13) in negative corresponds to the internal reflection. Then the ray direction is inverted

$$\vec{d}_{\mathrm{out}} = 2(-\vec{n} \cdot \vec{d}_{\mathrm{in}})\vec{n} + \vec{d}_{\mathrm{in}} \,. \tag{4.15}$$

To finalize the ray–tracing algorithm, the intersections of the conical cell faces with the rays have to be calculated. The problem leads to the solution of a single quadratic equation at each interface [55]. Knowing the ray initial energy Q_{in} and trajectory, the absorption of the laser energy in each particular cell ΔQ is given by

$$\Delta Q = Q_{\mathrm{in}} - Q_{\mathrm{out}} = Q_{\mathrm{in}} \left(1 - \mathrm{e}^{-\int \kappa_{\mathrm{ib}} \, \mathrm{d}s}\right) = Q_{\mathrm{in}} \left(1 - \mathrm{e}^{-\kappa_{\mathrm{ib}} L}\right) \,, \tag{4.16}$$

with the κ_{ib} given by (4.12) and the optical path $L = |\vec{p}_{\mathrm{in}} - \vec{p}_{\mathrm{out}}|$ of the ray in the cell.

The 3D ray–tracing algorithm, as described above, is applied for the simulation of a low–density foam target irradiated by an intense laser beam. The results of the simulation are presented in the fifth chapter of this thesis.

4.3. Laser–foam interaction

In this section, modifications of a hydrodynamic code are described, which are introduced in order to provide a correct model of the laser absorption in a low density foam. It enables to describe physical phenomena as the ionization front propagation and plasma heating. These modifications allow to simulate microstructured targets with standard hydrodynamic codes without considering a microscopic foam structure on the hydrodynamic level.

An interaction of a low–density foam target with a high–intensity laser pulse is modeled on two scales. At the macroscale level, the Lagrangian hydrodynamic model considers an artificial transient material state in the homogenization layer and a modified laser–plasma interaction, which simulates complex microscopic physics of the laser energy deposition. The both modifications are governed by an evolution of the detail foam structure calculated at the microscale level.

The microscale physics describes the local homogenization of the foam by an expansion of a thin plastic layer in 1D geometry. This model was firstly introduced in [60], where the expansion speed of each thin solid layer was governed by the local plasma sound speed. The microscale structure is introduced only in one layer of computational cells on the interface between the homogenized plasma and a cold non–ionized foam. For the macroscale model, the cell size corresponds to the estimated size of a single pore in the foam.

4.3.1. Time–dependent absorption coefficient in 1D

Here, we briefly describe the model of the laser–absorption in low–density foams, as it was introduced in [60]. Assuming that no laser radiation is reflected from the low–density foam target, the laser intensity at the plasma boundary is equal to the laser intensity $I_0 = I_0(t)$ at the given time. Following the notation of the third chapter, the laser intensity at the nodes of the computational mesh for the staggered discretization is defined as

$$I_{i+1/2} = I(x_{i+1/2}) = I_0 \mathrm{e}^{-\kappa_i^{\mathrm{ef}}(t)\Delta x_i}\,, \tag{4.17}$$

where $\Delta x_i = x_{i+1/2} - x_{i-1/2}$ and the time dependent absorption coefficient $\kappa_i^{\mathrm{ef}}(t)$ equals

$$\kappa_i^{\mathrm{ef}}(t) = \begin{cases} 2/\delta_0 & \text{for} \quad s_i^e(t) \leq \delta_0 \left(\frac{\rho_{\mathrm{av}}}{\rho_{\mathrm{cr}}}\right)^{\alpha} \\ \kappa_i^{\mathrm{ib}} & \text{for} \quad s_i^e(t) > \delta_0 \left(\frac{\rho_{\mathrm{av}}}{\rho_{\mathrm{cr}}}\right)^{\alpha} \end{cases} . \tag{4.18}$$

Here, ρ_{av} stands for the average foam mass density and ρ_{cr} for the mass critical density assuming the full ionization

$$\rho_{\mathrm{cr}} = n_e^{\mathrm{crit}} \frac{A m_p}{Z_i} \tag{4.19}$$

with the free–electron critical density n_e^{crit} given by (4.3). The inverse bremsstrahlung absorption coefficient κ_i^{ib} (4.12) is modified with respect to the expanding layer density

$$\kappa_i^{\mathrm{ib}} = \frac{\nu_{ei_i}}{c} \frac{\rho_i^e}{\rho_{\mathrm{cr}}} \tag{4.20}$$

with the effective density

$$\rho_i^e = \max \left[\frac{A m_p}{Z_i} n_{e_i} \,, \left(\frac{\delta_0}{s_i^e(t)} \right)^{\frac{1}{\alpha}} \rho_{\mathrm{av}} \right] , \tag{4.21}$$

the electron–ion collision frequency ν_{ei_i} (4.10), the proton mass m_p, the average mass number A, the average ionization Z_i and the free electron density n_{e_i} in the cell i. The empirical parameter $\alpha < 1$ accounts for the fractal structure of the foam. It depends on the pore size δ_0, its shape and on the chemical content of the material.

In the model [60], the thickness of a single expanding layer is approximated as

$$s_i^e(t) = \sum_{n=1}^{t} c_i^n \Delta t^n \tag{4.22}$$

with the hydrodynamic time step Δt^n, the recent time index t and the sound speed c_i^n depending on the current electron temperature $T_{e_i}^n$ and the initial temperature T^0

$$c_i^n = \sqrt{\frac{Z_i}{Am_p}(T_{e_i}^n - T^0)}. \tag{4.23}$$

Model parameters corresponding to the given foam are the pore size δ_0 and a foam fractal parameter α. These coefficients are given by the microscopic foam structure according to the scaling law for the solid density ρ_s and the characteristic width δ_s of the foam element

$$\delta_s \approx \delta_0 \left(\frac{\rho_{\text{av}}}{\rho_s}\right)^{\alpha}. \tag{4.24}$$

Note that $\alpha = 1$ corresponds to 1D situation with membrane–like structure and $\alpha = 1/2$ to 2D wire–like foam. The critical expansion factor s_{cr} of a single foam element in the right hand side of the inequalities (4.18) is therefore

$$\begin{aligned} \rho_{\text{cr}} s_{\text{cr}}^{\frac{1}{\alpha}} &\approx \rho_s \delta_s^{\frac{1}{\alpha}} \\ s_{\text{cr}} &\approx \delta_s \left(\frac{\rho_s}{\rho_{\text{cr}}}\right)^{\alpha} \approx \delta_0 \left(\frac{\rho_{\text{av}}}{\rho_s}\right)^{\alpha} \left(\frac{\rho_s}{\rho_{\text{cr}}}\right)^{\alpha} \approx \delta_0 \left(\frac{\rho_{\text{av}}}{\rho_{\text{cr}}}\right)^{\alpha}. \end{aligned} \tag{4.25}$$

We have observed that a 1D hydrodynamic simulation employing this method leads to a reduction of the speed of the ionization front in the foam. However, this reduction is not sufficient for the case of the GEKKO experiment [75].

4.3.2. Microscale foam model and its discretization

We extended the microscopic model [60] to a more realistic 3D geometry. Here, each computational cell at the hydrodynamic macroscale is supposed to contain one thin layer of the foam. This layer has the initial density of the solid material and it is approximated by a 1D flat layer. The layer is homogeneously heated either by the laser rays, which are entering in the computational cell, or by an electron heat transfer from the surrounding hot plasma. These source terms, i.e. the laser absorption and the heat flux, needed for the calculation of the solid layer expansion at the microscale level, are estimated from the macroscale hydrodynamic model.

The solid layer expansion is calculated by a standard hydrodynamic method with several sub-time-steps within each macroscale time-step. When the density of the modeled 1D layer becomes lower then the plasma critical density (4.25), the computational cell is supposed to be homogenized and transparent for the laser radiation.

At the microscale level, a symmetric 1D expansion is supposed, so only a half of the layer is modeled. A staggered discretization with the cell centered scalar variables (density ρ, specific internal energy ϵ and pressure p of the foam material) and node centered vectors (position s_e and velocity v_e) is used. The mass of the layer is divided between two nodes (the central node c and the edge node e) giving the nodal mass m_n. The central node is rigid with the local position $s_o = 0$ and velocity $v_o = 0$.

A temporal evolution of the velocity v_e of the edge node is given by

$$\frac{v_e^{n+1} - v_e^n}{\Delta t} = \frac{\max(0, p - p_{\text{ext}})}{m_n} \,. \tag{4.26}$$

The microscale time step Δt is obtained from a local CFL condition and the microscale pressure $p = p(\rho, \epsilon)$ from the equation of state of a plastic. Here, p_{ext} stands for the external (macroscale) hydrodynamic pressure. No compression of the layer is allowed, and thus an artificial viscosity term may be omitted.

Finally, the nodal position s_e and the specific internal energy ϵ are updated according to

$$\frac{s_e^{n+1} - s_e^n}{\Delta t} = \frac{1}{2}\left(v_e^{n+1} + v_e^n\right) \,, \tag{4.27}$$

$$\frac{\epsilon^{n+1} - \epsilon^n}{\Delta t} = \frac{-p\left(v_e^{n+1} + v_e^n\right)}{2m_n} - \frac{\Delta Q_c}{2\rho_c} \,. \tag{4.28}$$

The source term ΔQ_c presents the laser energy absorbed in the cell c. It is calculated according to the formula (4.16) provided by the ray–tracing algorithm and the density ρ_c of the macroscale computational cell.

The Spitzer–Harm collisional electron heat conductivity with a flux limiter is used [8]. If the internal energy of the macroscale computational cell in the homogenization layer is increased, the microscale cell internal energy is also increased with the same amount

(4.29).

$$\tilde{\epsilon}^{n+1} = \epsilon^{n+1} + \max(0, \tilde{\epsilon}_c - \epsilon_c) \,. \tag{4.29}$$

Here ϵ_c and $\tilde{\epsilon}_c$ stands for the macroscale specific internal energy before and after the heat conductivity step. The heat conductivity is calculated on the macroscale level in the PALE code. The increase in the microscale internal energy causes faster expansion of the slab in the following time step. Note that the cell temperature increases as far as the laser is being absorbed. A foam material ionization induced by heat transport starts to effect the computation if the local laser intensity decrease below the heat flux level.

4.3.3. Modifications on the hydrodynamic scale

The foam is modeled as a homogeneous material with the corresponding average density consisting of two states of computational cells. Except of the first layer of cells on the laser–irradiated target side, all other cells are supposed to be non–homogenized at the time $t = 0$. For the first layer of cells we do not introduce the absorption index modification according to (4.18), instead, we allow the cell to absorb all energy brought with the rays until the cell is expanded sufficiently according to (4.22). This slight modification allows to avoid too strong initial density gradient at the foam surface. Two modifications with respect to the microscale homogenization state of the cells are applied in the ALE hydrodynamic part of the PALE code with a standard heat transfer.

Firstly, the initially cold foam does not respond to pressure gradients and therefore the material stays rigid and does not move before the laser arrives. More precisely, nodal forces responsible for the Lagrangian mesh movement are set to zero for a node with at least one non–homogenized cell attached to the node. Once all the attached cells becomes homogenized, i.e. solid microscale layers associated with the cells expand below the critical density (4.25), we do not apply any restriction for the nodal forces.

Secondly, the foam solid layers are assumed to be opaque and to have a random orientation in the foam. Therefore, the direction of incoming laser rays is randomly altered at the homogenization (ionization) front, i.e. the surface between the cold foam and an ionized homogeneous plasma. These rays have uniform random distribution in the solid angle. Some rays penetrate the ionization front to be absorbed here. Remaining rays are returned back to homogenized plasma hitting the surface again or escaping from the target. These modifications take part only in the non–homogenized area of the computational grid.

The laser absorption in a homogenized plasma is calculated by the 3D ray–tracing algorithm described above using the bremsstrahlung absorption coefficient (4.12). In the cells of the homogenization layer, the local absorption coefficient κ_{ib} (4.16) is set to a value high enough to absorb all the laser rays penetrating these cells. Therefore, due to a random reflection of the incoming rays at the irradiated side of the cells, a half of the laser energy, which reached the homogenization layer is absorbed and a half reflected back to the homogenized plasma with the possibility of the future absorption in a different place or by the inverse bremsstrahlung.

5. Applications

We start this chapter with the numerical tests of the remapping methods, which are discussed in the third chapter. The cyclic remapping and full–hydrodynamic tests are performed to demonstrate the properties of these methods. We focus on the order–of accuracy, bounds– and symmetry–preservation properties of the methods. In the second part of this chapter, applicability of the different absorption methods is investigated for the hydrodynamic modeling of the laser beam interaction with a low–density foam. Finally, we present hydrodynamic simulations of the experiments performed on the PALS [6] and GEKKO [4] facilities by taking into account the particular modifications of the hydrodynamic model of the laser–foams interaction, as described in the fourth chapter.

5.1. Cyclic remap numerical tests

We start with a cyclic remapping [38] for a scalar quantity. The cyclic remapping is a numerical test based on a sequence of computational grids. Some analytical function is discretized on the first grid and then remapped to the second one. From the second grid it is again remapped to the next one until the final grid is reached. A comparison of the remapped values with the discretized known analytical function on the final grid provides the error accumulated during all these remapping steps.

5.1.1. 1D remapping methods

Here, we provide the comparison of the selected one–dimensional remapping methods described in the third chapter. The order of convergence and the bound–preservation of these methods are numerically demonstrated on cyclic remapping tests.

In this paragraph, we review the notation being used for the particular remapping methods. The remap with the piecewise constant reconstruction is denoted *donor*, with the piecewise linear reconstruction *lin.* – in case of unlimited slope described by (3.8) *unl.*, and with the piecewise parabolic reconstruction *pp* – in case of unlimited coefficients (3.23) *unl.*. Abbreviations for the slope and parabolic limiters correspond to *BJ* – *Barth–*

Jespersen (3.14), *MM – minmod* (3.9), respective (3.25), *KBJ – Kuzmin–Barth–Jespersen* (3.26) and *Nejat* – (3.27). In the case of the *MM* limiter we use $\beta = 1.5$ in (3.9) and (3.25) and we use $K = 1$ for Nejat limiter. The *PPM* marks the reconstruction according to (3.28) and *lin. FCR*, resp. *pp FCR* the FCR methods (2.5, 3.74) with the piecewise linear unlimited, respective piecewise parabolic unlimited reconstructions used for the high–order fluxes.

In the cyclic remapping test cases, the first two steps of the ALE method, namely the Lagrangian step and the rezoning step, are replaced by the prescribed motion of the computational grid. The numerical fluxes through the cell interfaces (nodes in 1D) are present only due to the grid motion. The exact solution of the cyclic remap corresponds to the preservation of the initial value if the initial and the final grids are the same.

Numerical error measurement

We assume than the mean $\overline{u}_i^0$ in all N cells of the initial computational grid x^0 and the grid motion (described later) are known. In n-th remapping pseudo–time step we get the means $\overline{u}_i^n$ on the mesh x^n and after n_t pseudo-timesteps, we get the means $\overline{u}_i^f$ on the final grid x^f. If the initial and the final grids are the same $x^0 = x^f$ (nodes are marked as $x_{i+1/2}$ and cells are indexed by i according to the section 3.1), then we define the absolute error of the cyclic remap as

$$E^c = \sum_{i=1}^{n} |\overline{u}_i^0 - \overline{u}_i^f| \Delta x_i^f \, ,$$

where $\Delta x_i^f = x_{i+1/2}^f - x_{i-1/2}^f$ is the volume of the cell i in the grid x^f. Generally, if the function $u(x)$ is known and the initial and the final grids x^0 and x^f are not the same, the exact values on the final grid can be evaluated as

$$\overline{u}_i^e = \frac{1}{\Delta x_i^f} \int_{x_{i-1/2}^f}^{x_{i+1/2}^f} u(x) \, \mathrm{d}x$$

and we define the overall error of the cyclic[1] remap as

$$E^c = \sum_{i=1}^{n} |\overline{u}_i^e - \overline{u}_i^f| \Delta x_i^f \, . \tag{5.1}$$

The bounds definition (3.4) is connected only with the single remapping step. We define

---

[1] The grid does not cycle back to the initial position, i.e. $x_f \neq x_0$, however we keep the name cyclic, or we use the name sub–cyclic to emphasize this difference.

the out–of–bounds error in n-th pseudo–time step as

$$E^{b^n} = \sum_{i=1}^{n} \max\left(0, \overline{u}_i^n - {}^{\max}\overline{u}_i^{n-1}\right) \Delta x_i^n + \sum_{i=1}^{n} \max\left(0, {}^{\min}\overline{u}_i^{n-1} - \overline{u}_i^n\right) \Delta x_i^n \,,$$

where the n-th pseodo–time step bounds are ${}^{\max}\overline{u}^n = \max\{\overline{u}_{i-1}^n, \overline{u}_i^n, \overline{u}_{i+1}^n\}$ a ${}^{\min}\overline{u}^n = \min\{\overline{u}_{i-1}^n, \overline{u}_i^n, \overline{u}_{i+1}^n\}$. Overall out–of–bounds error for the whole cyclic remapping is then the L_1 error in the pseodo–time

$$E^b = \sum_{n=1}^{n_t} E^{b^n} \Delta t_n \,. \tag{5.2}$$

Another interesting property of the remap is the preservation of the global bounds of the initial function

$$E^g = \sum_{i=1}^{n} \max\left(0, \overline{u}_i^f - {}^{\max}\overline{u}\right) \Delta x_i^f + \sum_{i=1}^{n} \max\left(0, {}^{\min}\overline{u} - \overline{u}_i^f\right) \Delta x_i^f \,, \tag{5.3}$$

where the initial bounds are ${}^{\max}\overline{u} = \max_i\{\overline{u}_i^0\}$ a ${}^{\min}\overline{u} = \min_i\{\overline{u}_i^0\}$. All the described errors (together with the ratio of E^c at different mesh resolutions) for the selected remapping methods are presented in tables 5.1, 5.3, 5.2 and 5.4 for the different initial functions, different computational grid motion and different mesh resolution (meshes with 64–512 cells). Values in the second, third and fourth columns of each table stand for the ratios of remapping errors E^c (5.1) during the grid refinement, while the order of convergence (not shown in the tables) are the base–two logarithm of these values. The rest of the columns show the errors E_n^c 5.1, E_n^b 5.2 and E_n^g 5.3 for a mesh with N cells.

Mesh movement

We perform commonly used [38] computational grid movement, where the grids x^n are given by their nodes $\{x_{i-1/2}^n, i = 1, \ldots, n; n = 0, \ldots, n_t\}$. The mesh movement (illustrated in Fig. 5.1) is described by the smooth function

$$x(\xi, t) = (1 - \alpha(t))\xi + \alpha(t)\xi^3 \,,\ \alpha(t) = \frac{\sin(4\pi t)}{2} \,,\ 0 \le \xi \le 1 \qquad 0 \le t \le 1 \,. \tag{5.4}$$

Using this function, the grid sequence x^n is given by the grid nodes positions $x_{i-1/2}^n =$

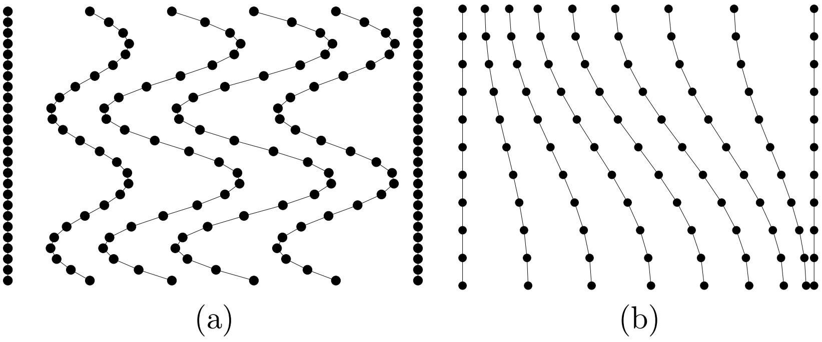
(a) (b)

Figure 5.1.: Computational grid sequence for 5 cells and 25 pseudo–time steps (a) in the pseudo–time interval $t \in [0,1]$ and for 8 cells in 10 steps with $t \in [-1/8, 1/8]$ (b). The horizontal axis represent the spatial coordinate x and the vertical one the pseudo–time t.

$x(\xi_i, t^n)$ where

$$t^n = \frac{n}{n_t}\ ,\ n = 0, \dots, n_t\ ;\ \xi_i = \frac{i-1}{N}, i = 1, \dots, N+1\,. \tag{5.5}$$

The number of pseudo–time steps n_t is set to $n_t = 5N$, where N is the number of cells in given mesh. This condition is related to a standard CFL condition. If we define

$$\mathrm{CFL} = \Delta t \left[\max_i \left(\frac{a_{i-1/2}}{\Delta x_i}\right)\right]^{-1}\ , \tag{5.6}$$

where the node velocity is $a_{i-1/2} = \frac{\mathrm{d}x_{i-1/2}}{\mathrm{d}t}$, then we obtain the maximal CFL number approximately 0.48 for this mesh motion. This condition can be interpreted as the condition on the nodes of the new grid. Each node of the new grid x^{n+1} has to stay in limits defined by the neighboring cell–centers from the previous grid x^n.

Cyclic remap to initial grid of a sinus function

Numerical performance of our methods for the cyclic remap with a different (random) grid movement is demonstrated in [a3]. Here, we use the smooth mesh movement (5.4) in all 1D test cases for two different pseudo–time intervals. As the first test case, we choose a smooth initial function $\sin(2\pi x) + 1$ on the computational domain $x \in [0,1]$. The results indicating the order of convergence, errors and the bound violations for the first test are presented in Tab. 5.1. The sinus function has a local extrema in this domain, leading to the worse convergence of the strictly bounds–preserving methods, such as PPM and FCR. Further, the smooth grid movement described by (5.4) for the pseudo–time $t \in [0,1]$

Remap	$\frac{64}{128}$	$\frac{128}{256}$	$\frac{256}{512}$	E^c_{64}	E^c_{512}	E^b_{64}	E^b_{512}	E^g_{64}	E^g_{512}
donor	1.8	1.9	1.9	$1.43 \cdot 10^{-1}$	$2.17 \cdot 10^{-2}$	0	0	0	0
lin. unl.	8.0	8.0	8.0	$4.37 \cdot 10^{-4}$	$8.55 \cdot 10^{-7}$	$7.2 \cdot 10^{-6}$	$1.4 \cdot 10^{-8}$	0	0
lin. BJ	4.6	4.8	4.9	$2.87 \cdot 10^{-3}$	$2.62 \cdot 10^{-5}$	0	0	0	0
lin. MM	4.5	4.8	4.9	$5.36 \cdot 10^{-3}$	$5.12 \cdot 10^{-5}$	0	0	0	0
lin. FCR	4.9	4.9	4.7	$1.09 \cdot 10^{-3}$	$9.84 \cdot 10^{-6}$	0	0	0	0
pp unl.	8.0	8.0	8.0	$3.90 \cdot 10^{-4}$	$7.63 \cdot 10^{-7}$	$7.2 \cdot 10^{-6}$	$1.4 \cdot 10^{-8}$	0	0
pp KBJ	8.0	8.0	8.0	$3.91 \cdot 10^{-4}$	$7.63 \cdot 10^{-7}$	$7.2 \cdot 10^{-6}$	$1.4 \cdot 10^{-8}$	0	0
pp MM	8.0	8.0	8.0	$3.90 \cdot 10^{-4}$	$7.63 \cdot 10^{-7}$	$7.2 \cdot 10^{-6}$	$1.4 \cdot 10^{-8}$	0	0
pp FCR	5.2	5.6	5.6	$9.66 \cdot 10^{-4}$	$5.93 \cdot 10^{-6}$	0	0	0	0
PPM	5.1	5.5	5.6	$2.06 \cdot 10^{-3}$	$1.33 \cdot 10^{-5}$	0	0	0	0
pp Nejat	3.3	3.8	4.0	$1.28 \cdot 10^{-3}$	$2.53 \cdot 10^{-5}$	$5.5 \cdot 10^{-6}$	$1.8 \cdot 10^{-8}$	$1.5 \cdot 10^{-4}$	$5.6 \cdot 10^{-6}$

Table 5.1.: Errors and their ratios for different cyclic remaps of $\sin(2\pi x) + 1$ on $x \in [0, 1]$ for the pseudo–time $t \in [0, 1]$ on grids with $N = 64,\ 128,\ 256$ and 512 cells.

leads to the super–convergence of the piecewise linear unlimited method (errors in the norm (5.1) show the third–order of accuracy corresponding to the errors ratio 8). It seems that errors, accumulated during the mesh movement to the right, are canceled with the errors introduced by the backward motion. To eliminate this super–convergence, we use the same grid motion (5.4) however with the pseudo–time $t \in [-1/8, 1/8]$, which we call sub–cyclic remap as the final mesh is different from the initial one (so it is not cyclic).

Sub–cyclic remap of a sinus function

As stated above, the same initial function $\sin(2\pi x) + 1$ is discretized on the initial mesh, which is however different from the first test case. The grid motion (5.4) is modified only by its application to the sub–cyclic pseudo–time $t \in [-1/8, 1/8]$ instead of $t \in [0, 1]$. This motion is indicated in Fig. 5.1 (b), where we can see that the initial and final meshes are different. According to the CFL (5.6) condition, we set $n_t = \frac{5}{4}N$ for pseudo–time interval $t \in [-1/8, 1/8]$. Results for the sub–cyclic pseudo–time interval are shown in Tab. 5.2. The super–convergence of the piecewise linear unlimited method (lin. unl.) is canceled by the change of the pseudo–time interval. In Tab. 5.1 we see, that the donor is first order, all methods with piecewise linear reconstructions are second order, piecewise parabolic pp unl, pp KBJ and pp MM ate third order, pp FCR and PPM are better than second order and pp Nejat is second order for this test. Note, that lin. unl. method does not satisfy bounds, while limited piecewise linear methods satisfy bounds. From piecewise parabolic methods, only pp FCR and PPM satisfy bounds, when pp unlimited and pp limited by KBJ or MM do not satisfy bounds. This is related to the existence of local extrema of the

Remap	$\frac{64}{128}$	$\frac{128}{256}$	$\frac{256}{512}$	E^c_{64}	E^c_{512}	E^b_{64}	E^b_{512}	E^g_{64}	E^g_{512}
donor	1.9	2.0	2.0	$4.20 \cdot 10^{-2}$	$5.53 \cdot 10^{-3}$	0	0	0	0
lin. unl.	4.1	4.0	4.0	$3.99 \cdot 10^{-4}$	$6.11 \cdot 10^{-6}$	$7.0 \cdot 10^{-6}$	$1.4 \cdot 10^{-8}$	$9.9 \cdot 10^{-6}$	$5.2 \cdot 10^{-8}$
lin. BJ	4.2	4.4	4.4	$1.42 \cdot 10^{-3}$	$1.72 \cdot 10^{-5}$	0	0	0	0
lin. MM	4.2	4.5	4.5	$2.15 \cdot 10^{-3}$	$2.58 \cdot 10^{-5}$	0	0	0	0
lin. FCR	4.0	3.9	3.9	$7.27 \cdot 10^{-4}$	$1.19 \cdot 10^{-5}$	0	0	0	0
pp unl.	8.0	8.0	8.0	$9.66 \cdot 10^{-5}$	$1.91 \cdot 10^{-7}$	$7.0 \cdot 10^{-6}$	$1.4 \cdot 10^{-8}$	$1.2 \cdot 10^{-5}$	$5.5 \cdot 10^{-8}$
pp KBJ	7.9	8.0	8.0	$9.66 \cdot 10^{-5}$	$1.92 \cdot 10^{-7}$	$7.0 \cdot 10^{-6}$	$1.4 \cdot 10^{-8}$	$1.2 \cdot 10^{-5}$	$5.5 \cdot 10^{-8}$
pp MM	7.9	8.0	8.0	$9.75 \cdot 10^{-5}$	$1.93 \cdot 10^{-7}$	$7.0 \cdot 10^{-6}$	$1.4 \cdot 10^{-8}$	$1.2 \cdot 10^{-5}$	$5.5 \cdot 10^{-8}$
pp FCR	5.6	5.6	5.5	$4.39 \cdot 10^{-4}$	$2.57 \cdot 10^{-6}$	0	0	0	0
PPM	5.3	5.0	5.2	$1.04 \cdot 10^{-3}$	$7.52 \cdot 10^{-6}$	0	0	0	0
pp Nejat	3.7	4.0	4.1	$4.47 \cdot 10^{-4}$	$7.35 \cdot 10^{-6}$	$5.4 \cdot 10^{-6}$	$1.7 \cdot 10^{-8}$	$1.6 \cdot 10^{-5}$	$1.3 \cdot 10^{-6}$

Table 5.2.: Errors and their ratios for different sub–cyclic remaps of $\sin(2\pi x) + 1$ on $x \in [0, 1]$ for the pseudo–time $t \in [-1/8, 1/8]$ on grids with $N = 64,\ 128,\ 256$ and 512 cells.

remapped function inside the computational domain. Note that for piecewise parabolic methods we can either reach third order (unl., KBJ and MM) or preserve bounds (pp FCR and PPM), none of the methods is able to reach third order and preserve bounds for functions with a local extrema inside the computational domain. However, the paper [37] might inspire improvements at local extrema.

Sub–cyclic remap of a monotone function

For this test case, the function $\exp(x)$ is monotone and has no local extrema in the computational domain $x \in [0, 1]$ and thus all remapping methods preserve bounds. Table

Remap	$\frac{64}{128}$	$\frac{128}{256}$	$\frac{256}{512}$	E^c_{64}	E^c_{512}	E^b_{64}	E^b_{512}	E^g_{64}	E^g_{512}
donor	2.0	2.0	2.0	$7.91 \cdot 10^{-3}$	$1.01 \cdot 10^{-3}$	0	0	0	0
lin. unl.	3.9	3.9	4.0	$1.16 \cdot 10^{-5}$	$1.92 \cdot 10^{-7}$	0	0	0	0
lin. BJ	3.8	3.9	4.0	$1.13 \cdot 10^{-5}$	$1.91 \cdot 10^{-7}$	0	0	0	0
lin. MM	3.9	3.9	4.0	$1.16 \cdot 10^{-5}$	$1.92 \cdot 10^{-7}$	0	0	0	0
lin. FCR	3.9	3.9	4.0	$1.16 \cdot 10^{-5}$	$1.92 \cdot 10^{-7}$	0	0	0	0
pp unl.	7.9	7.9	8.0	$4.67 \cdot 10^{-7}$	$9.32 \cdot 10^{-10}$	0	0	0	0
pp KBJ	7.9	7.9	8.0	$4.67 \cdot 10^{-7}$	$9.32 \cdot 10^{-10}$	0	0	0	0
pp MM	7.9	7.9	8.0	$4.67 \cdot 10^{-7}$	$9.32 \cdot 10^{-10}$	0	0	0	0
pp FCR	7.9	7.9	8.0	$4.67 \cdot 10^{-7}$	$9.32 \cdot 10^{-10}$	0	0	0	0
PPM	8.0	8.0	8.0	$2.13 \cdot 10^{-7}$	$4.15 \cdot 10^{-10}$	0	0	0	0
pp Nejat	4.0	4.0	4.0	$1.65 \cdot 10^{-5}$	$2.56 \cdot 10^{-7}$	0	0	0	0

Table 5.3.: Errors and their ratios for different sub–cyclic remaps of $\exp(x)$ on $x \in [0, 1]$ for the pseudo–time $t \in [-1/8, 1/8]$ on grids with $N = 64,\ 128,\ 256$ and 512 cells.

5.3 shows the convergence of the selected remapping methods for $t \in [-1/8, 1/8]$ for the function $\exp(x)$. The first–order is reached by the piecewise constant and the second–order for the piecewise linear methods. For the most of the piecewise parabolic methods, i.e. pp unl, pp KBJ, pp MM, pp FCR and PPM, the fraction 8 indicating the third–order of convergence is reached. The poor convergence (just second order) of the Nejat limiter can be related to the selected constants in the Nejat limiter.

Sub–cyclic remap of a discontinuous function

Table 5.4 and Figure 5.2 show results for the step function $f(x) = 4.6$ for $x \in [0, 1/2]$, $f(x) = 1.4$ for $x \in [1/2, 1]$. The convergence is very similar for all methods as expected, i.e. less than first order for the discontinuous function, but the value of errors are different. The best method is PPM followed by FCR with the piecewise parabolic, respective linear high–order reconstruction. The donor, piecewise linear limited (BJ,MM,FCR) and piecewise parabolic FCR and MM methods preserve bounds as for the non monotone sin test case. The minmod limiter for the piecewise parabolic reconstruction disturbs the bounds much less than the unlimited reconstruction and the method is third–order accurate on a smooth solution.

Remap	$\frac{64}{128}$	$\frac{128}{256}$	$\frac{256}{512}$	E^c_{64}	E^c_{512}	E^b_{64}	E^b_{512}	E^g_{64}	E^g_{512}
donor	1.4	1.4	1.4	$1.41 \cdot 10^{-1}$	$5.38 \cdot 10^{-2}$	0	0	0	0
lin. unl.	1.5	1.6	1.5	$5.03 \cdot 10^{-2}$	$1.32 \cdot 10^{-2}$	$7.7 \cdot 10^{-5}$	$3.5 \cdot 10^{-6}$	$6.6 \cdot 10^{-3}$	$1.3 \cdot 10^{-3}$
lin. BJ	1.5	1.6	1.6	$3.85 \cdot 10^{-2}$	$9.65 \cdot 10^{-3}$	0	0	0	0
lin. MM	1.6	1.6	1.6	$4.33 \cdot 10^{-2}$	$1.04 \cdot 10^{-2}$	0	0	0	0
lin. FCR	1.5	1.6	1.6	$3.60 \cdot 10^{-2}$	$9.32 \cdot 10^{-3}$	0	0	0	0
pp unl.	1.6	1.6	1.6	$4.97 \cdot 10^{-2}$	$1.19 \cdot 10^{-2}$	$9.1 \cdot 10^{-5}$	$4.0 \cdot 10^{-6}$	$7.9 \cdot 10^{-3}$	$1.7 \cdot 10^{-3}$
pp KBJ	1.6	1.6	1.7	$5.05 \cdot 10^{-2}$	$1.20 \cdot 10^{-2}$	$6.5 \cdot 10^{-5}$	$3.2 \cdot 10^{-6}$	$7.6 \cdot 10^{-3}$	$1.7 \cdot 10^{-3}$
pp MM	1.6	1.6	1.7	$4.22 \cdot 10^{-2}$	$9.71 \cdot 10^{-3}$	$2.7 \cdot 10^{-6}$	$1.7 \cdot 10^{-8}$	$2.3 \cdot 10^{-5}$	$2.7 \cdot 10^{-6}$
pp FCR	1.6	1.6	1.6	$3.60 \cdot 10^{-2}$	$8.88 \cdot 10^{-3}$	0	0	0	0
PPM	1.7	1.6	1.7	$2.45 \cdot 10^{-2}$	$5.32 \cdot 10^{-3}$	0	0	0	0
pp Nejat	1.6	1.6	1.6	$4.14 \cdot 10^{-2}$	$1.03 \cdot 10^{-2}$	$3.7 \cdot 10^{-5}$	$1.5 \cdot 10^{-6}$	$3.8 \cdot 10^{-3}$	$1.1 \cdot 10^{-3}$

Table 5.4.: Errors and their ratios for different sub–cyclic remaps of the step function on $x \in [0, 1]$ for the pseudo–time $t \in [-1/8, 1/8]$ on grids with $N = 64,\ 128,\ 256$ and 512 cells.

To conclude, we have shown that from the piecewise parabolic methods, only PPM and FCR preserve bounds. A sub–cyclic or a random mesh movement [a3] are required to obtain relevant orders of convergence, i.e. to avoid a super–convergence for piecewise linear methods.

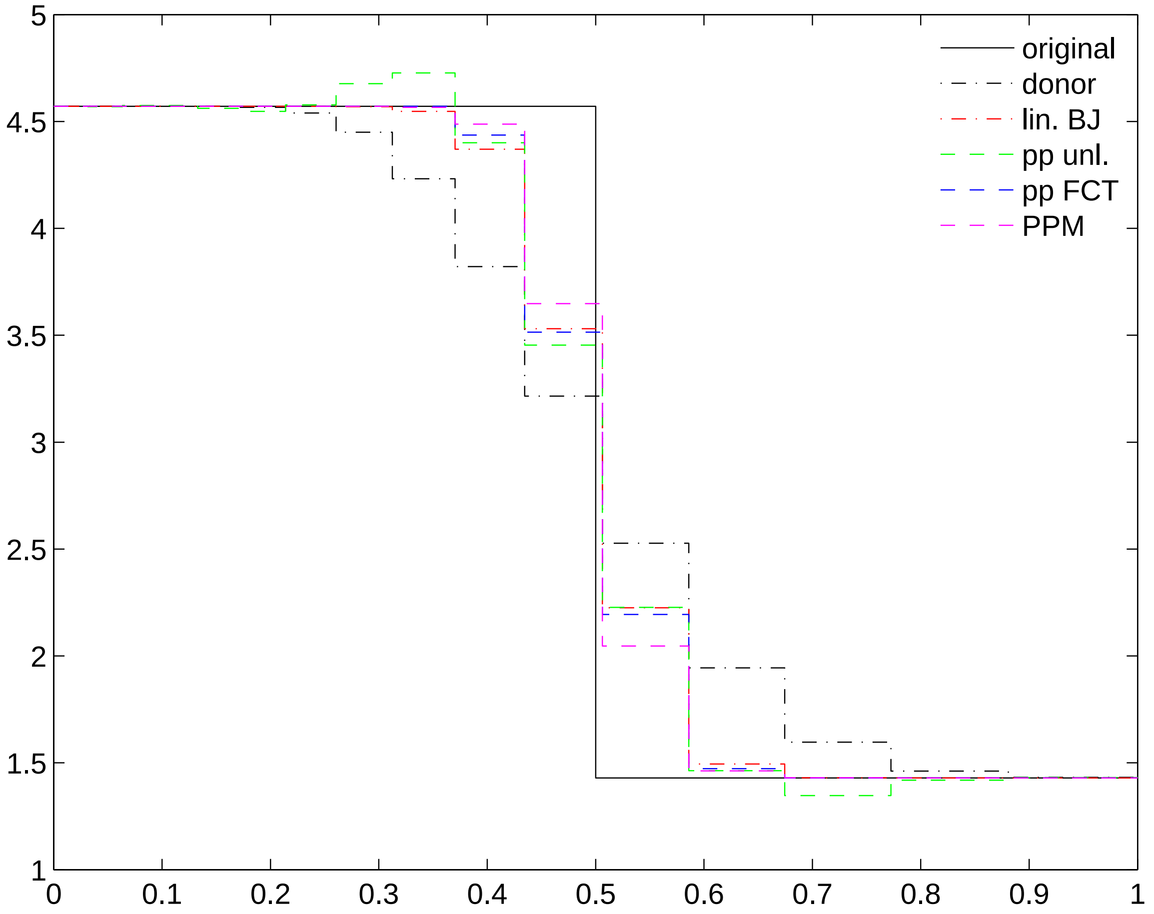

Figure 5.2.: Sub–cyclic remapping for the selected remapping methods. The step function for the pseudo–time $t \in [-1/8, 1/8]$ on 16 cells. The initial (exact) function marked by the black line.

5.1.2. 2D remapping methods for a scalar

In this section, we focus on the preservation of the order of convergence for the two particular numerical flux computation methods from section 3.5, namely: the swept–based approximate method and the exact integration method with piecewise linear and piecewise quadratic reconstructions. We demonstrate that both methods preserve the third–order of accuracy for the unlimited piecewise quadratic reconstruction. Presented errors of the sub–cyclic remap E^c are defined analogically to (5.1).

Pseudo 1D standard advection test analog

As the very first test of this section, we chose an analogue of the standard 1D advection test [19] performed on a 2D computational domain, to check the validity of our methods. The initial condition consists of a Gaussian, rectangular, triangular and parabolic shaped initial function shown from left to right in Fig. 5.3. The function is discretized on the initial domain $(x, y) \in [0, 2] \times [0, 0.1]$ with 400 × 1 equidistantly spaced cells (2D domain

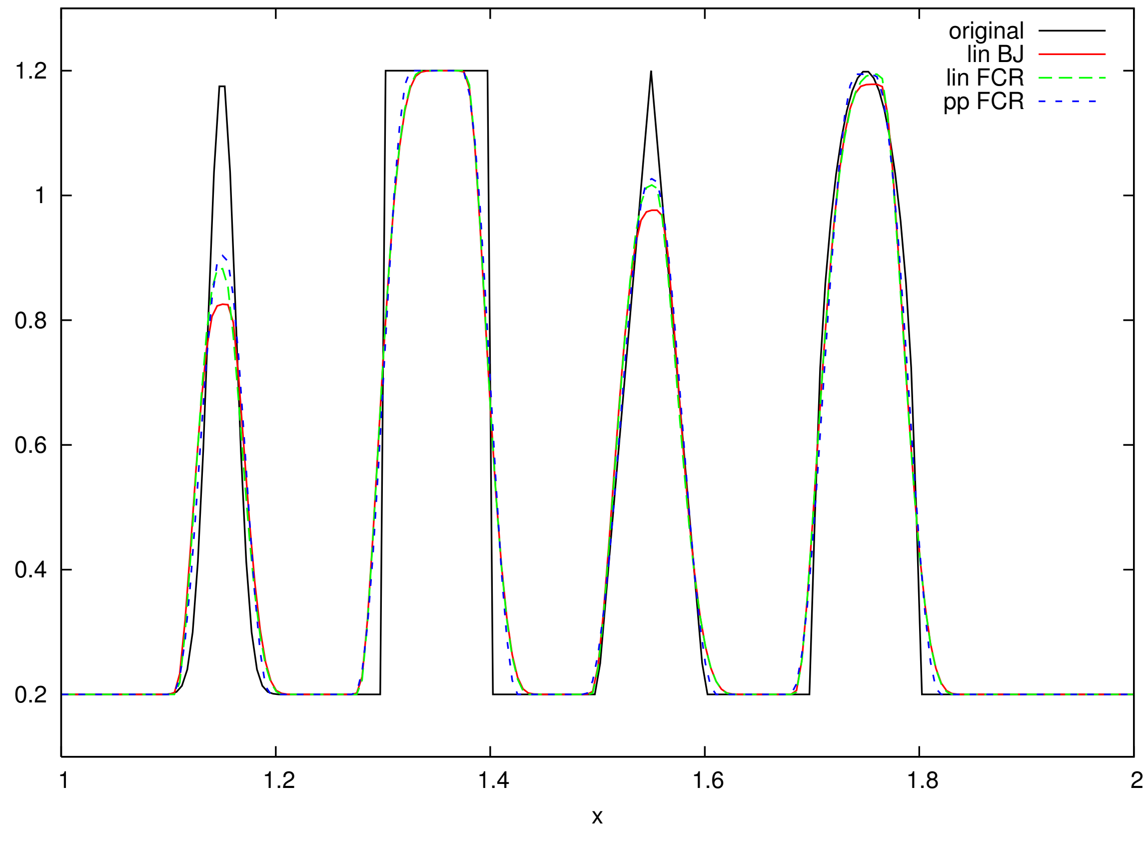

Figure 5.3.: Advection–like remap test case for a scalar.

with one cell in the y direction is used). The function is initially non–zero only in the right part $x \in [1, 2]$ of the domain. The grid movement is represented by a set of 1000 small translations to the final domain $[1, 3] \times [0, 0.1]$. All the translations are the same, i.e. each step the grid is moved by $1/1000 < \Delta x = 1/200$. This is an analog of an advection test case with a CFL number equal to 0.2, where the grid is static and the solution is moved with a constant velocity. Results in Fig. 5.3 show that the flux corrected remapping method with the piecewise quadratic reconstruction (blue) is superior to other methods. The piecewise linear method is more affected by the direction of the mesh movement, see e.g. the difference on the top of the parabolic shape. However, due to our definition of the bounds, the piecewise quadratic method is worse than the other 3rd–order smooth extrema–preserving methods for the Eulerian mesh [19].

Pseudo 1D test of convergence

The loss of the order of convergence for our method in a presence of a local extrema inside the computational domain is also indicated by the results in Tab. 5.5. We applied the same grid movement as in the previous test with a smooth initial Gaussian function $1+\exp(-(7x-10.5)^2)$. For the third–order method, the error ratio should be equal to 2^3, compared to 7.02, which is achieved for pp FCR for the finer grids. Similarly lin. BJ is loosing the convergence with the error ratio 3.72 compared to 2^2. The loss of convergence is due to the strict bounds–preservation requirement.

Method	$\frac{40}{80}$	$\frac{80}{160}$	$E^c_{40\times 3}$	$E^c_{80\times 3}$	$E^c_{160\times 3}$
lin. BJ	3.96	3.72	$1.08{\cdot}10^{-2}$	$2.73{\cdot}10^{-3}$	$7.33{\cdot}10^{-4}$
pp FCR	7.84	7.02	$6.44{\cdot}10^{-3}$	$8.21{\cdot}10^{-4}$	$1.17{\cdot}10^{-4}$

Table 5.5.: Convergence for a 1D smooth problem with a local extrema.

2D test of numerical flux methods

The next 2D remapping test is chosen to verify the order of the remapping method for both, the swept flux [40] and the exact intersection–based computation of numerical fluxes. Note that both methods are equivalent for previous pseudo 1D configurations. We choose the initially equidistant mesh on a rectangular domain $[0, 0.5] \times [0, 0.5]$ and we remap a smooth Gaussian function $1+\exp\left(-10[(x-0.25)^2+(y-0.25)^2]\right)$. The positions of mesh

Method	$\frac{20}{40}$	$\frac{40}{80}$	$E^c_{20\times20}$	$E^c_{40\times40}$	$E^c_{80\times80}$
Linear & exact intersections	3.72	3.81	$8.01{\cdot}10^{-5}$	$2.15{\cdot}10^{-5}$	$5.64{\cdot}10^{-6}$
Parabolic & exact intersections	7.46	7.67	$3.25{\cdot}10^{-5}$	$4.36{\cdot}10^{-6}$	$5.69{\cdot}10^{-7}$
Linear & swept fluxes	3.73	3.82	$7.96{\cdot}10^{-5}$	$2.13{\cdot}10^{-5}$	$5.59{\cdot}10^{-6}$
Parabolic & swept fluxes	7.46	7.67	$3.23{\cdot}10^{-5}$	$4.34{\cdot}10^{-6}$	$5.65{\cdot}10^{-7}$

Table 5.6.: 2D cyclic remap of a smooth function. Unlimited piecewise polynomial reconstruction with different methods of numerical flux computation.

nodes are given by

$$
\begin{aligned}
x^n_{i-1/2,j-1/2} &= x^0_{i-1/2,j-1/2} + t\sin(2\pi x^0_{i-1/2,j-1/2})\sin(2\pi y^0_{i-1/2,j-1/2})\\
y^n_{i-1/2,j-1/2} &= y^0_{i-1/2,j-1/2} + t\sin(2\pi x^0_{i-1/2,j-1/2})\sin(2\pi y^0_{i-1/2,j-1/2})\\
t &= \frac{n}{10n_t},\ n = 1,\ldots,n_t,\ i,j = 1,\ldots,M.
\end{aligned}
$$

Figure 5.4 shows an example of the initial and final mesh for this mesh movement (on a computational domain $[0,1]\times[0,1]$), where the corresponding cells on two meshes are plotted with the same color. The initial grid is indicated by a superscript 0, $n_t = \{100, 200, 400\}$ stands for the total number of remapping steps and $M = \{21, 41, 81\}$ for the number of grid points in each direction. Results in Tab. 5.6 show the expected order of convergence for both the swept flux and exact intersection–based methods with corresponding unlimited piecewise polynomial (linear and parabolic) reconstructions. The FCR option (as well as the BJ limiter) was switched off in this test to keep the order of

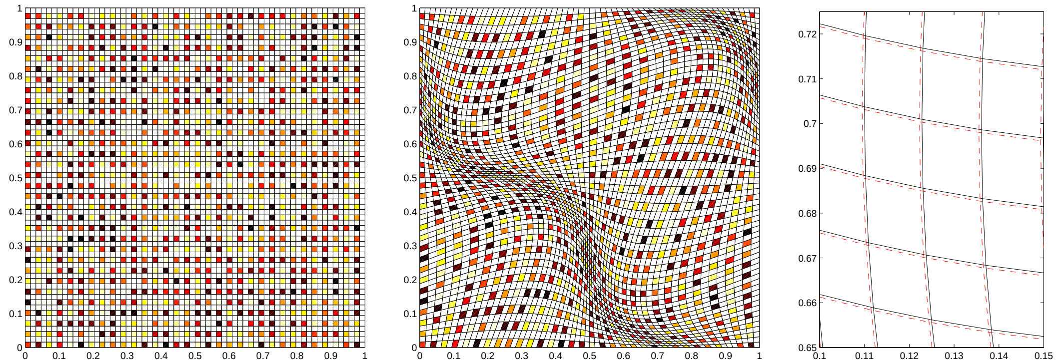

(a) (b) (c)

Figure 5.4.: 2D cyclic remap: an example of the initial– (a) and final (b) quadrilateral grid and the particular mesh displacement (c) for a Cartesian grid. Colors in (a) and (b) are used for visualization purposes.

convergence at the smooth extremum. We would like to point out, that the initial and the final grids are not the same. Consequently, it is important to discretize the smooth function as an integral mean value over the cells of the initial and the final grid, not just to use a function value e.g. at the centroid of the cell.

The bound–preservation of the FCR method is a direct consequence of the method construction under conditions described in subsection 3.5.1. We do not demonstrate this property for a 2D cyclic remap. However, we checked the bound–preservation in hydrodynamical calculations and our FCR method preserved the bounds in all presented tests during the remap.

5.1.3. 2D remapping methods for a vector

In this subsection, we focus on the preservation of the radial symmetry for radial fields of various momentum remapping methods with piecewise linear velocity reconstructions on a dual mesh for a staggered discretization. We describe these methods for the staggered discretization is [a2, a5]. For the cyclic remap on a polar quadrilateral computational domain $(r, \varphi) \in [0.01, 0.51] \times [0, 2\pi]$, we apply the grid movement (5.5) for the radial coordinate $r(\xi, t)$, whereas we keep the grid static in the angular direction φ

$$
\begin{aligned}
x^n_{i-1/2,j-1/2} &= r(\xi_i/2 + 0.01, t^n)\cos\varphi_j \\
y^n_{i-1/2,j-1/2} &= r(\xi_i/2 + 0.01, t^n)\sin\varphi_j, \qquad\qquad \varphi_j = \frac{2\pi j}{n_j}, j = 1, \dots, n_j\,,
\end{aligned}
$$

with the n_j cells in the angular direction. This grid movement in illustrated in Fig. 5.5.

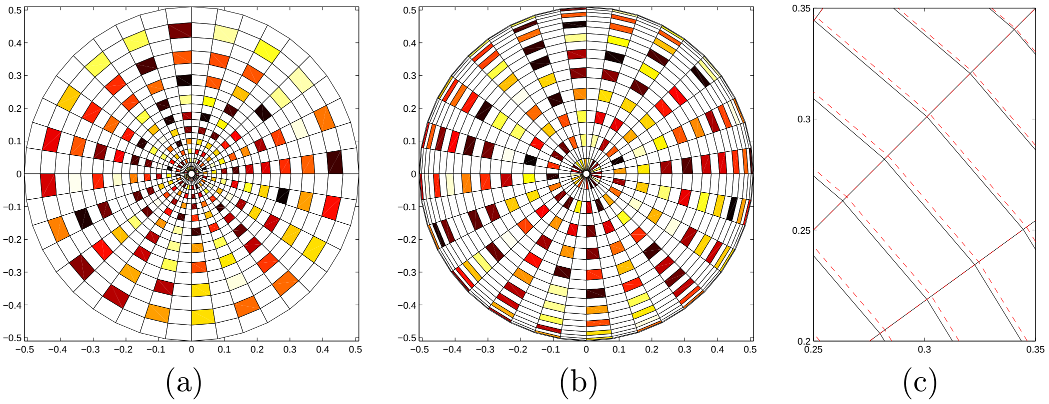

Figure 5.5.: 2D cyclic remap: an example of the initial– (a) and final (b) quadrilateral grid and the particular mesh displacement (c) for a polar grid. Colors in (a) and (b) are used for visualization purposes.

For this test, we choose a radial initial function with the discontinuity in magnitude

$$|\vec{w}| = \begin{cases} 3 & \text{for} \quad r < 0.25 \\ 1 & \text{for} \quad r \geq 0.25 \end{cases} .$$

From the contours of the remapped velocity magnitude in Fig. 5.1.3, we observe that the BJ limiter (3.43) for Cartesian velocity components as well as an independent FCR for Cartesian components (3.71) (denoted FCRxy) clearly break the symmetry and violate the bounds. Corresponding scatter plots of the velocity magnitude over the radial direction in Fig. 5.7 show the symmetry of our FCR method for the staggered discretization [a2] (FCRs) with the min/max constraints projected into the velocity direction. Our FCRs method removes only the overshoot (upper out–of–bounce value) in the velocity magnitude. The undershoot is a natural consequence of the bounds definition (3.79), where a neighboring node in the polar direction with the same velocity magnitude has certainly a smaller velocity component (in the direction of the velocity at the central node) than the radial component at the central node. This undershoot may be removed by an application of the MVIP limiter [a5] (or (3.65) for a cell–centered discretization), as we observe in Fig. (d). More examples of these symmetry–preserving momentum remapping methods for a staggered discretization may be found in [a2, a5].

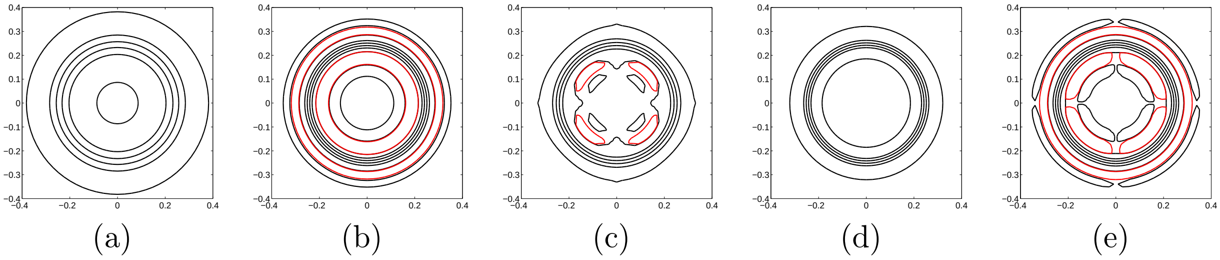

(a) (b) (c) (d) (e)

Figure 5.6.: Contour plots of the velocity magnitude for the cyclic remap of the step function in the radial velocity field on a polar grid. The low–order (a), unlimited (b), BJ– (c) and MVIP–limited (d), and FCRxy (e) method. Out–of–bound values in red.

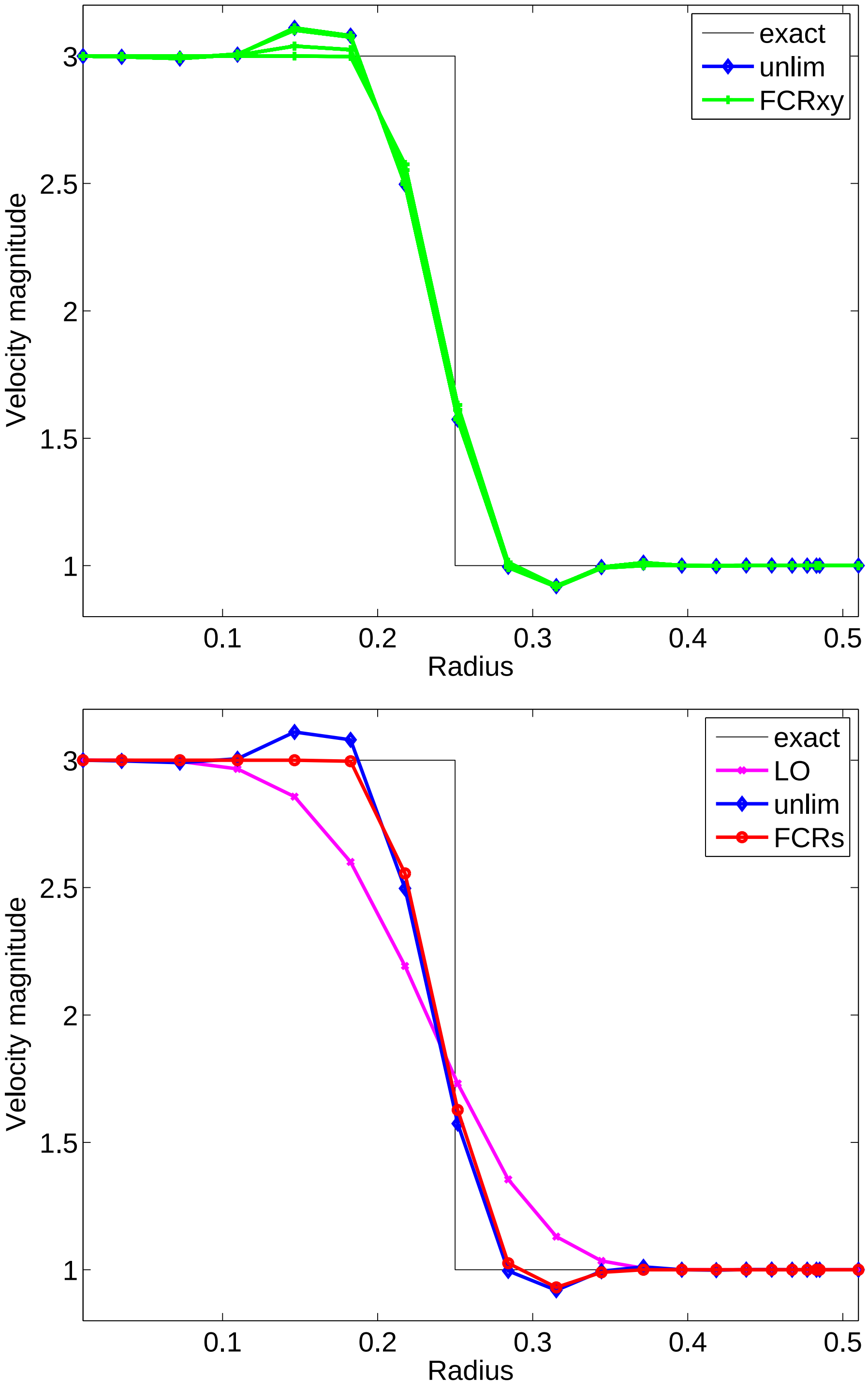

Figure 5.7.: Scatter plots of the velocity magnitude over radius for all angular indices for the unlimited piecewise linear (blue diamonds) and FCRxy (green lines) method (top), respective for the low–order (magenta), unlimited (blue), and symmetric FCRs (red) method (bottom).

5.2. Hydrodynamic test cases

We start the section with the 2D Sedov blast wave test case showing the importance of the symmetry–preserving remap of vectors. In this case, the symmetric FCR method with a piecewise linear reconstruction is applied to the momentum remap in a staggered code. The complete FCR with the piecewise quadratic high–order reconstruction for the all conservative quantities is performed in remaining hydrodynamic test cases of this subsection. Remaining tests demonstrate the properties of the complete remapping method from section 3.6.1. These tests were run in the cell–centered hydrodynamic code CHLER [10] and some of them were presented in [a1]. Two rezone strategies were applied. We refer a mesh smoothing after each Lagrangian time–step as the ALE mode, whereas the rezone back to the original grid after each time–step as the Euler mode. For the first strategy, the particular rezoning method consists of a local minimization problem for the node–based objective functions that define the criteria for grid quality [10]. Note that the Lagrangian step remains the same when we switch the tested remapping methods.

5.2.1. 2D Sedov blast wave on quadrilateral polar mesh

Here, we demonstrate the properties of the symmetry–preserving FCR method (FCRs) applied for the momentum remap for a full hydrodynamic example – the Sedov point explosion test [76]. These results have been already presented in [a2]. We compare the FCRs method to a standard FCR method applied to both momentum components independently (refereed as FCRxy). This FCRxy method may be obtained by setting the local rotation matrix (3.59) to the identity matrix.

The computational domain $(\mathrm{r},\varphi) \in (0.01,\ 1.2) \times (0,\ 2\pi)$ is covered by an equidistant 100×40 polar mesh. At the initial time $t = 0$, the fluid (ideal gas with $\gamma = 1.4$) is static everywhere $\vec{w} = \vec{0}$ and has an uniform density $\rho = 1$. The specific internal energy is $\varepsilon = 10^{-8}$ everywhere except the innermost layer of cells in the center of the domain, where $\varepsilon = 821.105$, which corresponds to the amount of energy in the definition of the Sedov problem presented in [77], transformed to the given polar mesh. The high-energy cells represent a point initial energy generating a circular shock wave spreading from the center. In the final time $t = 1$, the shock wave reaches the radius $r = 1$.

This simulation was run in the framework of the staggered research multimaterial ALE (rmALE) code [78], employing the compatible discretization of the Euler equations as presented in [23], and the edge artificial viscosity model from [22]. For remapping, the

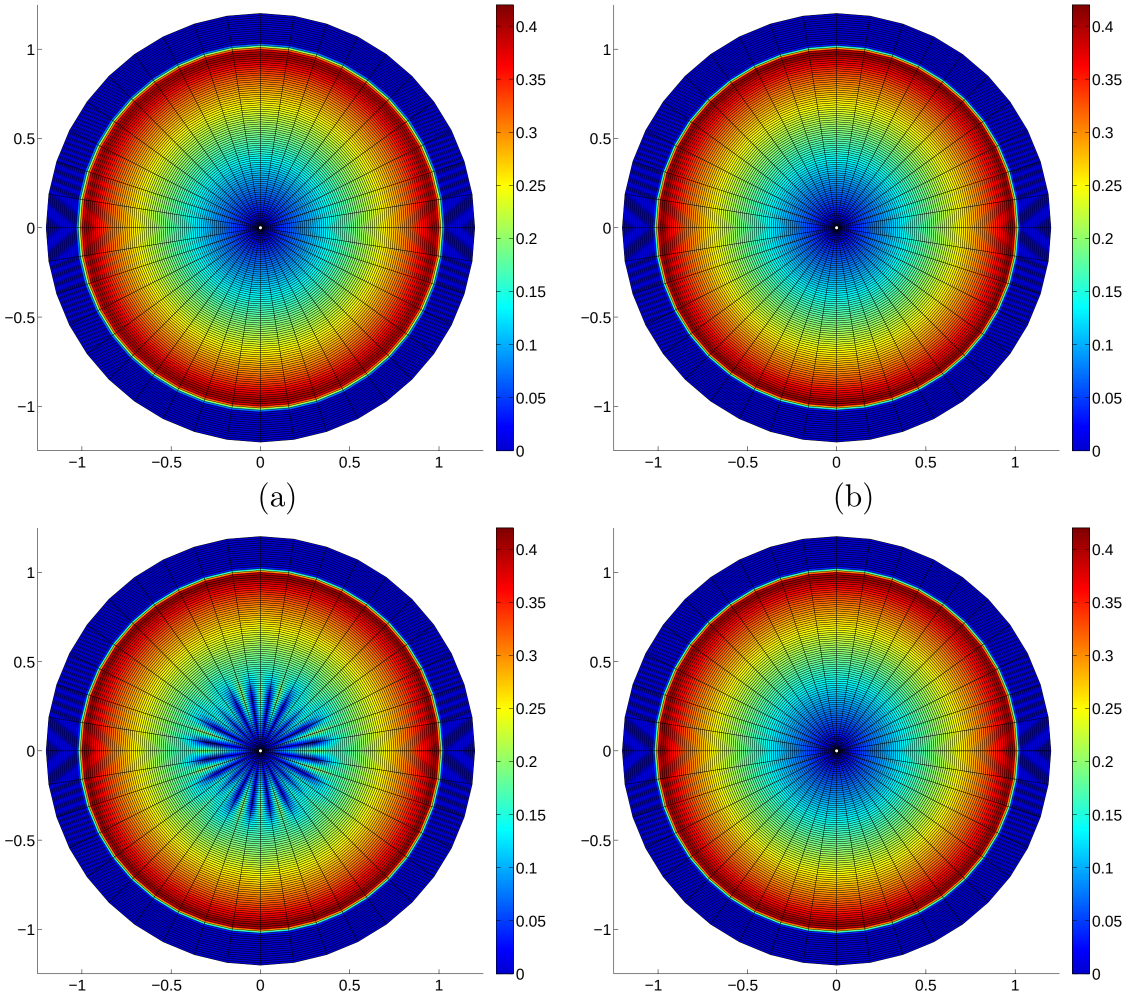

(a) (b)

(c) (d)

Figure 5.8.: Velocity magnitude distribution for the Sedov problem at time $t = 1$ using the low–order (a), unlimited (b), component FCRxy (c), and symmetric FCRs (d) method for velocity reconstruction.

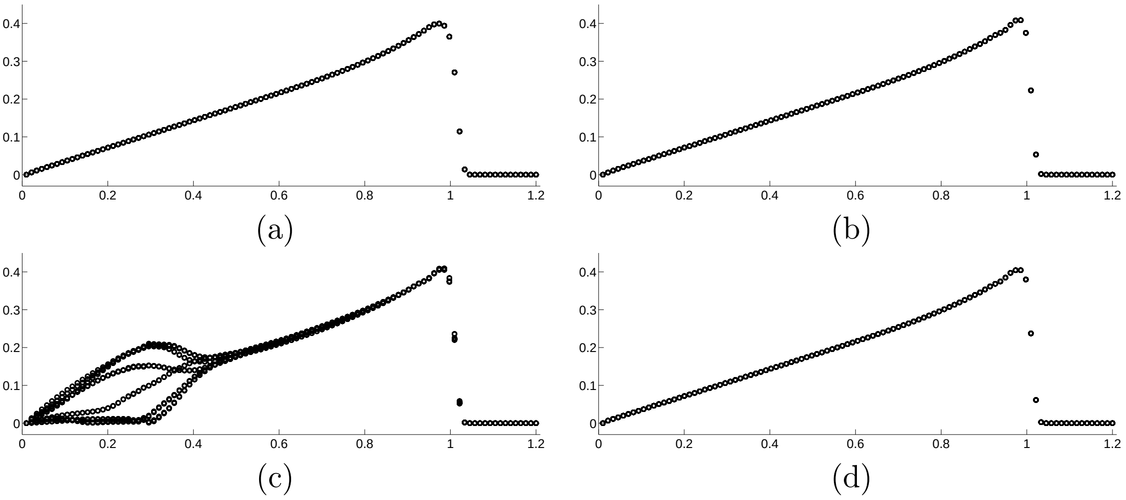

Figure 5.9.: Scatter plot of velocity magnitude for the Sedov problem at time $t = 1$ using the low–order (a), unlimited (b), FCRxy (c), and FCRs (d) method for velocity reconstruction.

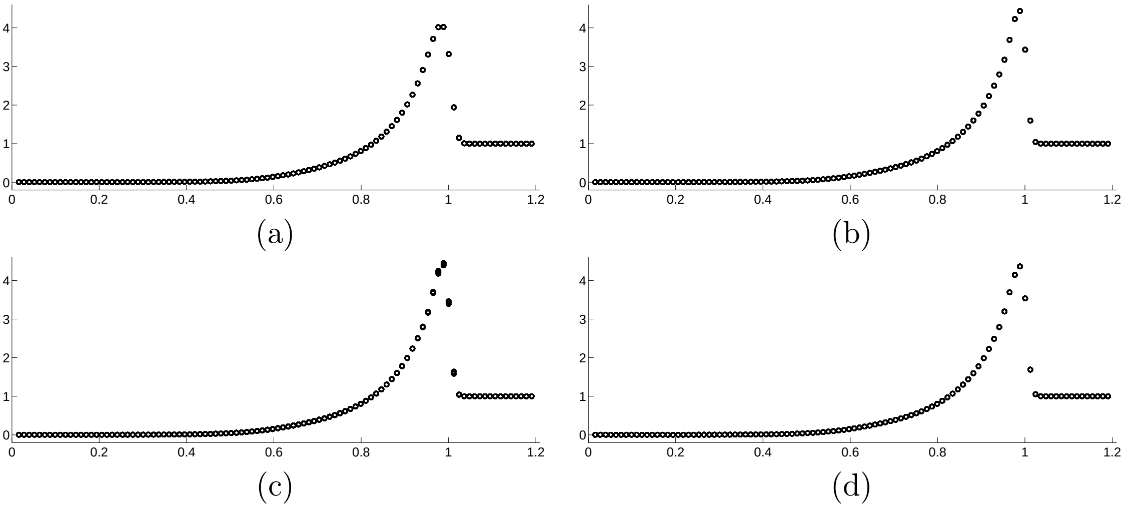

Figure 5.10.: Scatter plot of fluid density for the Sedov problem at time $t = 1$ using the low–order (a), unlimited (b), FCRxy (c), and FCRs (d) method for velocity reconstruction.

flux-based method described in [71, 78] is used – all quantities are remapped in a flux form, the remap of fluid momentum is similar to the approach described in section 3.6.1, where the particular application of the method to staggered discretization is described in [a2]. To enhance the effects of remapping, this simulation was run in the Euler mode, where all fluid quantities are remapped back to the initial computational mesh after each Lagrangian step. We present results of four different runs using four velocity reconstruction methods – the low–order, unlimited, component FCRxy in x, y directions, and the symmetric FCRs approach.

Velocity magnitude 2D distributions at the final time moment are shown in Fig. 5.8 for each reconstruction method. In Fig. 5.9, the final velocity distribution in the entire problem is shown as a function of radius. For this particular problem, we can see only a small difference between the low– and high–order approaches at the maximum velocity. The FCRxy by components causes a severe symmetry violation at the domain center, making this method inapplicable for realistic simulations. After switching to the new symmetric FCR approach, the solution is perfectly symmetric and the velocity profile is very close to the high–order approach.

In Fig. 5.10, we show the final density distribution in the entire problem for the same runs. The differences between the low– and high–order velocity reconstructions is more apparent here. We can observe blurring of the density profile for the component FCRxy approach due to the loss of symmetry in velocity, which propagates to all fluid quantities. The new method produces a perfectly symmetric solution.

5.2.2. 1D Sod shock tube

To demonstrate the bounds preservation of the complete FCR method as it is described in section 3.7, we start with the standard Sod shock tube [79] test shown in Fig. 5.11. For this Riemann problem, the initial condition values of density, velocity and pressure are $\{1,0,1\}$ for $x < 0.5$ and $\{0.125,0,0.1\}$ for $x > 0.5$ with a gas constant $\gamma = 1.4$. The solution of the Sod test case consists of three type of waves, namely the shock, contact discontinuity and rarefaction wave. We use the Eulerian mode, i.e. the remapping at every time step to the initial grid to emphasize the properties of the remap. The final density, velocity and specific internal energy are shown in Fig. 5.11 at the time 0.2. The piecewise quadratic FCR method is slightly more diffusive on the contact discontinuity than the BJ-limited method. This is probably due to fact that the restrictions to numerical fluxes are applied to all fluid quantities simultaneously. The piecewise quadratic FCR method preserves the

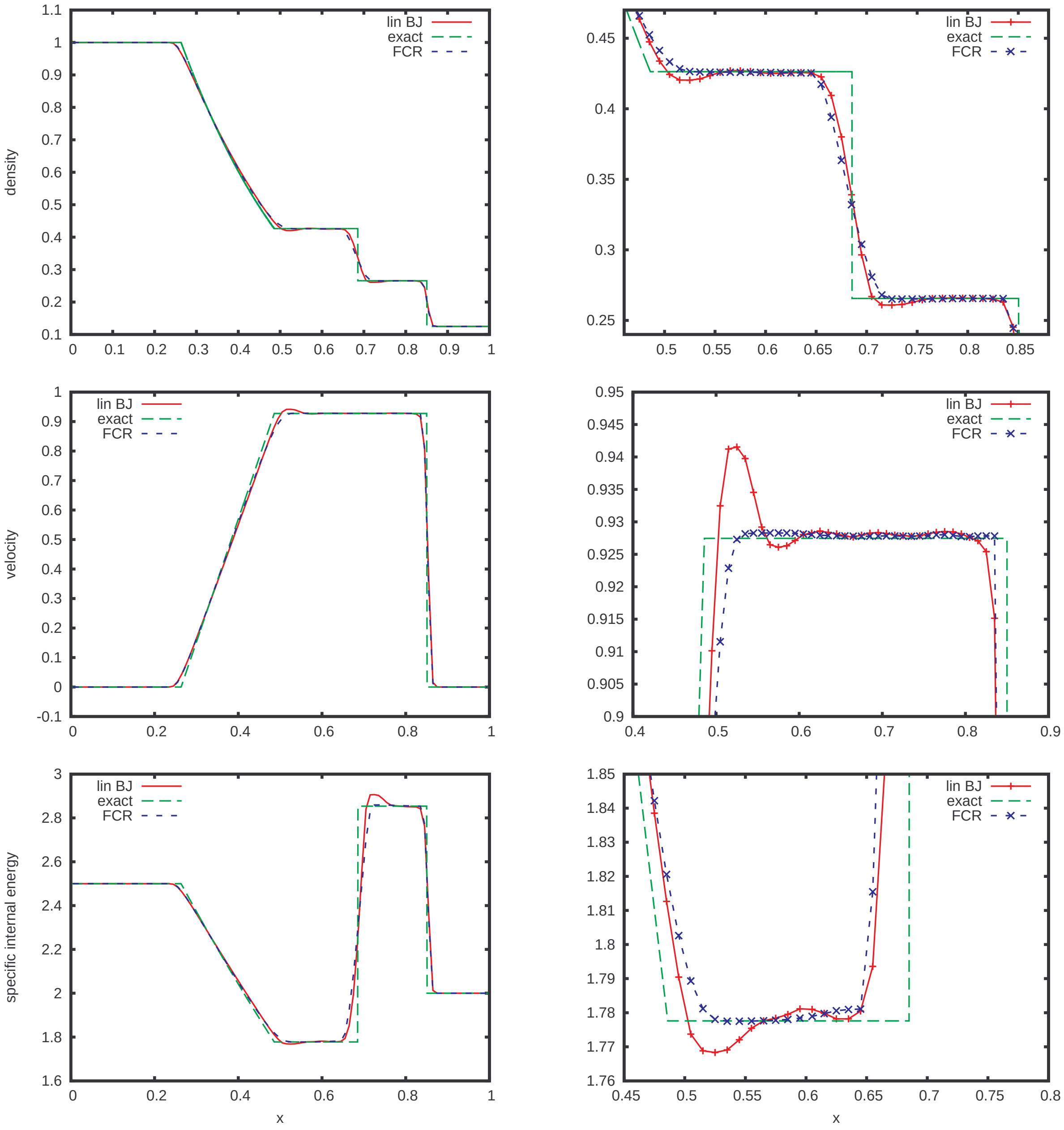

(a) (b)

Figure 5.11.: 1D Sod shock tube, Eulerian mode, 3 × 100 cells. Density, velocity and specific internal energy for the whole domain (a) and in details (b) for the piecewise linear BJ limited method (red) and for the piecewise quadratic FCR method (blue).

bounds on density, velocity and specific internal energy during the remapping stage of the calculation, whereas the standard BJ limiter does not kill all numerical (dispersion) oscillations.

5.2.3. 2D Sod shock tube

The 2D extension of the Sod test addresses the issue of a poor linear approximation on polar meshes by the piecewise linear reconstruction method, i.e. the method with the slope (3.8, 3.24). The computational domain approximating a full circle with a radius 1 is discretized by a polar quadrilateral mesh with 7 cells in the angular direction and 100 cells in the radial one. The initial values of density, velocity and pressure are $\{1,\vec{0},1\}$ for the cell center radius $r < 0.5$ and $\{0.125,\vec{0},0.1\}$ for $r > 0.5$ with a gas constant $\gamma = 1.4$. The results of the calculations in the pure Lagrangian and Eulerian modes are presented in Fig. 5.12 and in Fig. 5.13 at the final time 0.2.

The piecewise linear remapping method suffers from a strong diffusion caused by very low angular mesh resolution, whereas the piecewise quadratic FCR method is close to the Lagrangian (reference) solution. Note that for the 2D polar Sod test case, the reference density between the tail of the rarefaction wave and the contact discontinuity as well as between the contact and the shock is no longer constant.

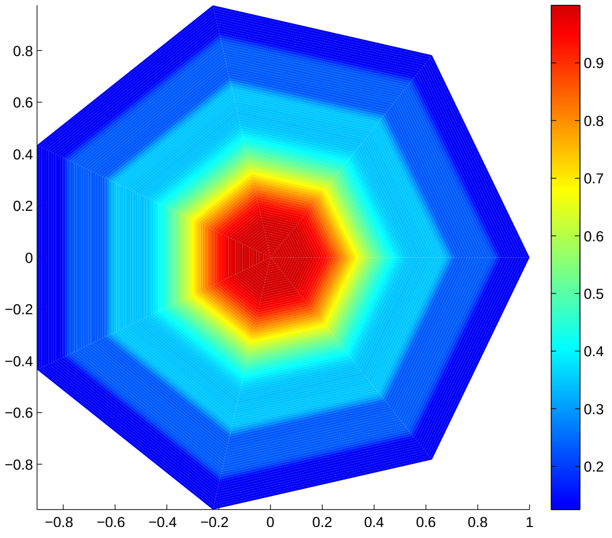

Figure 5.12.: Density colormap for the 2D polar Sod shock test case in the Eulerian mode for 7 × 100 cells.

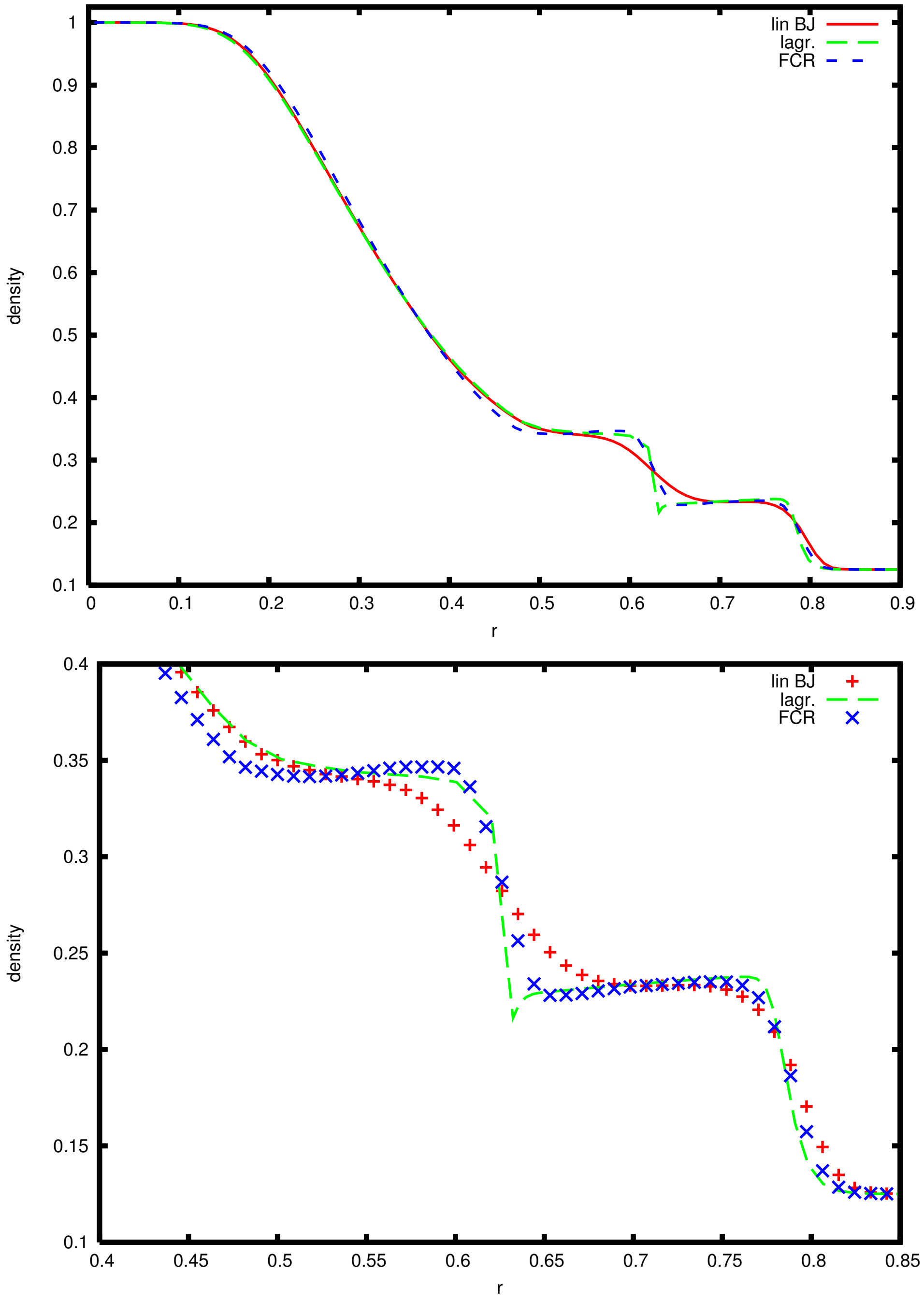

Figure 5.13.: Density scatter plot of the whole computational domain (top) and a zoom (bottom) for the 2D polar Sod shock test case in the Eulerian mode for 7 × 100 cells. Piecewise linear BJ limited method in red, piecewise quadratic FCR in blue and a reference Lagrangian solution in green.

5.2.4. 2D Sedov blast wave on polygonal meshes

To demonstrate the applicability of the remapping method for more complex grids, we run the Sedov blast wave similar to conditions described in section 5.2.1. Because of the different computational domain, the initial internal energy of a central cell is modified to maintain the same amount of the total deposited energy. The first case in the Euler mode on the equidistant hexagonal grids with 20/40/80 cells on the edge [-1.2,1.2] of the computational domain. The errors and convergence ratios for the density error (computed from a comparison with 1D solution on 1000 cells given by [80]) in a L1 norm are given

Method	$\frac{10}{20}$	$\frac{20}{40}$	E^c_{10}	E^c_{20}	E^c_{40}
donor	1.34	1.43	$4.94{\cdot}10^{-1}$	$3.68{\cdot}10^{-1}$	$2.58{\cdot}10^{-1}$
lin FCR	1.35	1.51	$4.43{\cdot}10^{-1}$	$3.28{\cdot}10^{-1}$	$2.17{\cdot}10^{-1}$
pp FCR	1.51	1.56	$4.13{\cdot}10^{-1}$	$2.73{\cdot}10^{-1}$	$1.75{\cdot}10^{-1}$

Table 5.7.: Convergence in density errors for the Sedov problem on a hexagonal grid with 10/20/40 cells per edge [-1.2,1.2]. Three different remapping methods. Eulerian mode.

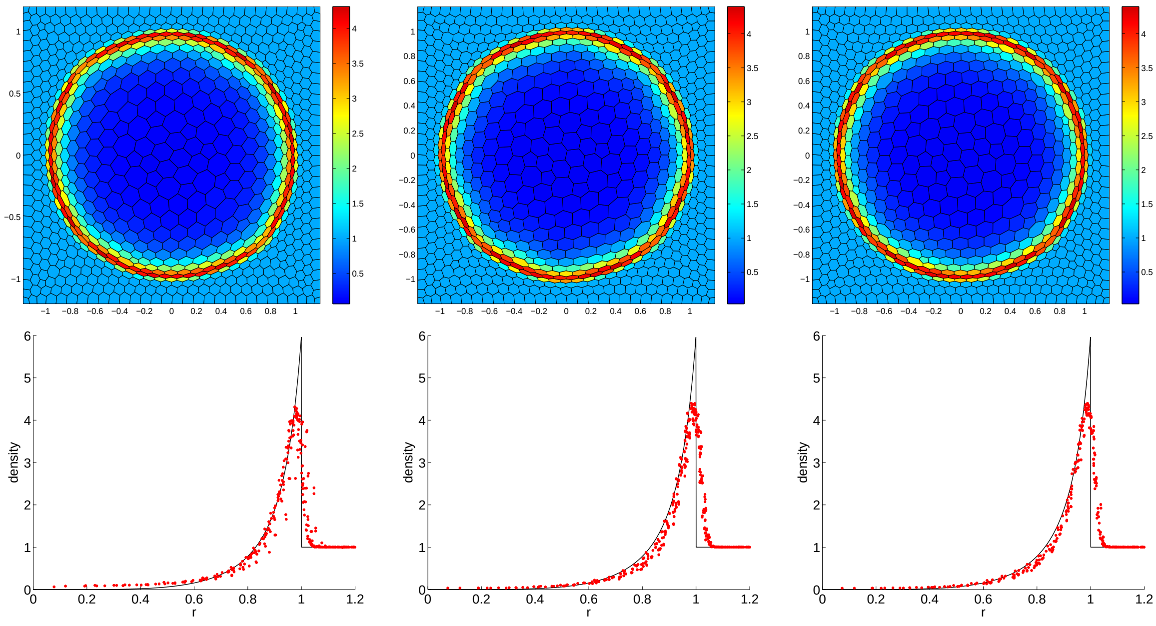

(a) (b) (c)

Figure 5.14.: Scatter plot of density versus radius for unstructured Sedov test case, remapping method with a piecewise constant (a), FCR with a piecewise linear (b) and a piecewise parabolic (c) reconstructions. ALE mode.

in Tab. 5.7. It shows the benefits of the high–order reconstruction, where the piecewise quadratic method provides the error rations bigger than 1.5 compared to 1.3 – 1.4 for two other methods.

Results of the remapping method with a piecewise constant (i.e. the donor method), the FCR with a piecewise linear and the FCR with a piecewise quadratic reconstructions in the ALE mode with a standard rezoning [10] for an unstructured grid are presented in Fig. 5.14. The figure shows a better preservation of the polar symmetry and a reduction of the mesh imprint by the higher–order reconstruction during the remapping stage.

5.2.5. 2D Noh implosion

The better preservation of the symmetry is further demonstrated by results of the Noh implosion test shown in Fig. 5.15 at the final time 0.6. We run the test in the Euler mode. The computation is initialized with the constant initial density 1 and the radial velocity -1 directed towards the origin on the square domain [-0.3,0.3] × [-0.3,0.3] covered by the equidistant rectangular grid with 100 × 100 cells. The initial and boundary pressure is set to $1 \cdot 10^{-6}$ and we apply the exact density condition on the computational domain boundary $\rho(r) = (1 - (0.6/r))^2$. The mesh imprint in Fig. 5.15 is reduced and the shock is better captured by the higher–order methods.

The last two hydrodynamic tests demonstrate an advantage of the high–order piecewise quadratic reconstruction being used in the remapping method. An application of the high–order reconstruction improves both the accuracy and the symmetry of the results. The BJ–limited remapping method with a piecewise linear reconstruction for the density, components of momentum and total energy (without any repair method) fails to pass both these tests (Sedov and Noh) because the negative internal energy is generated.

Our FCR method using the piecewise quadratic reconstruction for the system of Eulerian hydrodynamic equations is bounds–preserving by construction of the constraints. No repair techniques are needed to maintain the positivity of the internal energy. The performed numerical tests verify the preservation of the radial symmetry and demonstrate the benefits of the piecewise quadratic reconstruction. The numerical results of our piecewise quadratic FCR method are comparable or superior to existing methods based on the limited piecewise linear reconstruction.

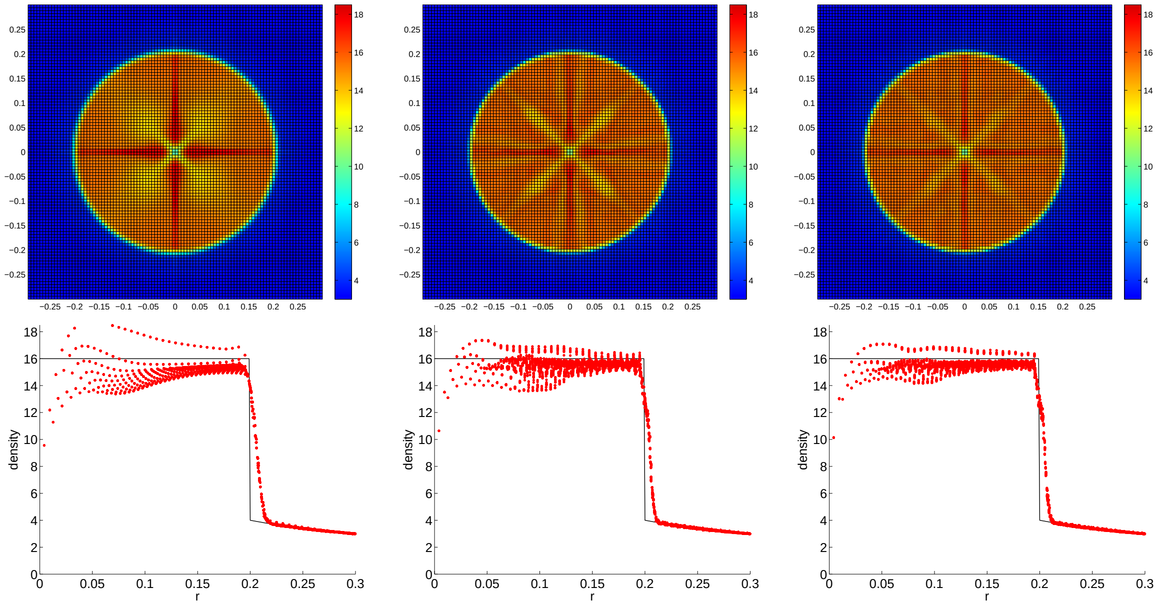

(a) (b) (c)

Figure 5.15.: Scatter plot of density versus radius for Noh test case, remapping method with a piecewise constant (a), FCR with a piecewise linear (b) and a piecewise parabolic (c) reconstructions. Eulerian mode. Exact solution $\rho = 16$ for $r < 0.2$ and $\rho = 1 - ((0.6/r))^2$ for $r > 0.2$ plotted by a black line.

5.3. Laser–foam interaction modeling

In this section, we compare different methods of the laser absorption modeling with the aim to evaluate their applicability for the laser–foam interaction simulation. We start the modeling for the GEKKO [4] laser system parameters [75]. The target is a 500 μm thick foam with the average density of 10 mg/cm^3. Its chemical composition is $C_{15}H_{20}O_6$, corresponding to the total electron density $3.2{\cdot}10^{21}$ cm^{-3}, the effective charge number Z and the mass A of an average ion are 3.85 and 7.22.

The target is illuminated by three overlapping laser beams of the total energy of 300 J at the 350 nm wavelength. A single laser beam is approximated by a set of rays parallel to the beam axis and each beam has the inclination of 4 degrees from the symmetry axis (Fig. 5.16) according to the experimental setup of the GEKKO laser facility. The focal plane is located at the front foam surface (i.e. the foam vacuum boundary). The laser beams are is incident from the right hand side. They have a triangular temporal shape and the 6th-order super Gaussian spatial profile with the 200 μm focal spot diameter. The maximum laser intensity of $3.5 \cdot 10^{14}$ W/cm^2 is reached at 400 ps after the simulation start and falls to 0 at the time 3400 ps.

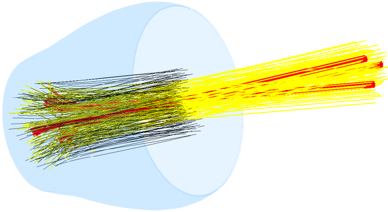

Figure 5.16.: Laser penetration through the foam target. The ionization front surface is shown in blue. Central parts of the three laser beams are emphasized. 3D ray-tracing at 700 ps.

The 2D cylindrically symmetric ALE modeling was performed on an initially square mesh with 200 × 250 cells. The ideal–gas equation of state with a fully ionized plasma was used. It was verified that the QEOS [81] with a more sophisticated ionization model provides quantitatively similar results. Radiation transport in not included in this modeling. The main goal is to explain the measured time of the foam burn–through in experiments. The measured time is significantly longer than the standard hydrodynamic simulations predict [75]. This is explained by a microscopic foam structure that delays the ionization process. We will demonstrate that an improved model of laser energy absorption in a foam introduced in the chapter 4 allows to significantly improve the quality of simulations, moving the predicted burn–through time closer to the experiment.

5.3.1. Laser absorption models

Laser absorption at critical surface

In this crude model the ray trajectories are straight lines and the absorption takes place in a over–critical plasma. Therefore, the rays penetrate through the sub–critical plasma without any refraction. Once the ray hits a computational cell with the electron density larger that the critical value (4.3), all the energy carried with this ray is absorbed in this super–critical cell. For this modeling of the sub–critical foam, we artificially set the critical electron density to $3{\cdot}10^{21}$ cm^{-3} below the average electron density of a fully ionized foam (because for this particular method, the foam has to have at least critical density in order to absorb any laser radiation). Therefore, in this crude model, all the laser energy is absorbed near the ionization front (just in the one layer of computational cells). This results in a formation of a weak shock, as illustrated in the first row of Fig. 5.17 for the time 700 ps. This is not what one would expect in an experiment.

For the sub–critical foam modeling, such a model of laser energy absorption on the critical surface is clearly not applicable. The laser energy absorption is strongly localized at the ionization front resulting in a steep increase of the plasma temperature, see Fig. 5.17. Finally, the calculated propagation time of the ionization front through the foam does not agree with the experiment, as indicated in Tab. 5.8.

Inverse bremsstrahlung with parallel straight rays

The laser energy deposition along each ray is calculated according to the local plasma parameters by using the relation (4.16) for the inverse bremsstrahlung absorption. The refraction is neglected, and the rays propagate through the plasma along the straight lines, until they are fully absorbed. We refer this model as *parallel rays*. The result of this simulation is plotted in the second row of Fig. 5.17. for the time 700 ps.

This method shows a better quantitative agreement with the more sophisticated numerical simulation in [75], where the parallel ray model has been used. However, it was concluded that it overestimates the ionization wave speed. In the second row in Tab. 5.8, we show the very similar results to [75], indicationg that a direct simulation of the foam as a homogeneous gas target is not applicable.

Inverse bremsstrahlung with a 3D ray–tracing

The inverse bremsstrahlung absorption is complemented by the 3D ray–tracing according to (4.14). We refer this method as *(3D RT) gas.*

The ray–tracing method introduces an additional laser beam filamentatiton. However, the filamentation predicted by ray–tracing methods is a numerical artifact, which is due to the finite distance between the rays. It does not capture such important physical phenomena as the laser beam diffraction and the ponderomotive force. With respect to the ionization front propagation speed, this method (see Tab. 5.8) provides the same inaccurate result as the previous straight ray model.

3D ray–tracing with a foam model

According to the laser absorption model [60], the two states of computational cells are defined. The initialization of this homogenization state of the cells follows the logic introduced in subsection 4.3.3, where except of the first layer of cells on the laser–irradiated target side, all other cells are supposed to be non–homogenized at the time $t = 0$. Concerning the non–homogenized structured cells, the laser rays are fully reflected in a random direction into the half–space defined by the cell position and the direction of incoming laser ray. The cold cell heating in this model is achieved by the electron heat conduction only.

A non–homogenized cold computational cell of the foam is heated up by the electron heat flux. The incoming energy is deposited in the solid layer thus inducing its expansion. Any absorption of the laser light in the structured cell (as in the original 1D model [60]) would result in the even faster propagation of the ionization front. According to the section 4.3.1 as in [60], the thin layer in each structured cell is initiated the solid state density of 1 g/cm^3. Once the layer expands to the sub–critical density level according to (4.18), the cell is switched to the homogenized plasma state. Then the laser rays can penetrate the cell and deposit the corresponding amount of their energy inside according to the inverse bremsstrahlung 3D ray–tracing model.

This method shows the strongest reduction of the ionization front propagation in the foam (see the fourth row in Tab. 5.8). This reduction is more significant than the one obtained with the original numerical 1D model [60], which not provide a sufficient reduction of the propagation speed compared to the models presented above in this subsection. The latter model is referred as *(3D RT) foam.*

5.3.2. Modeling results

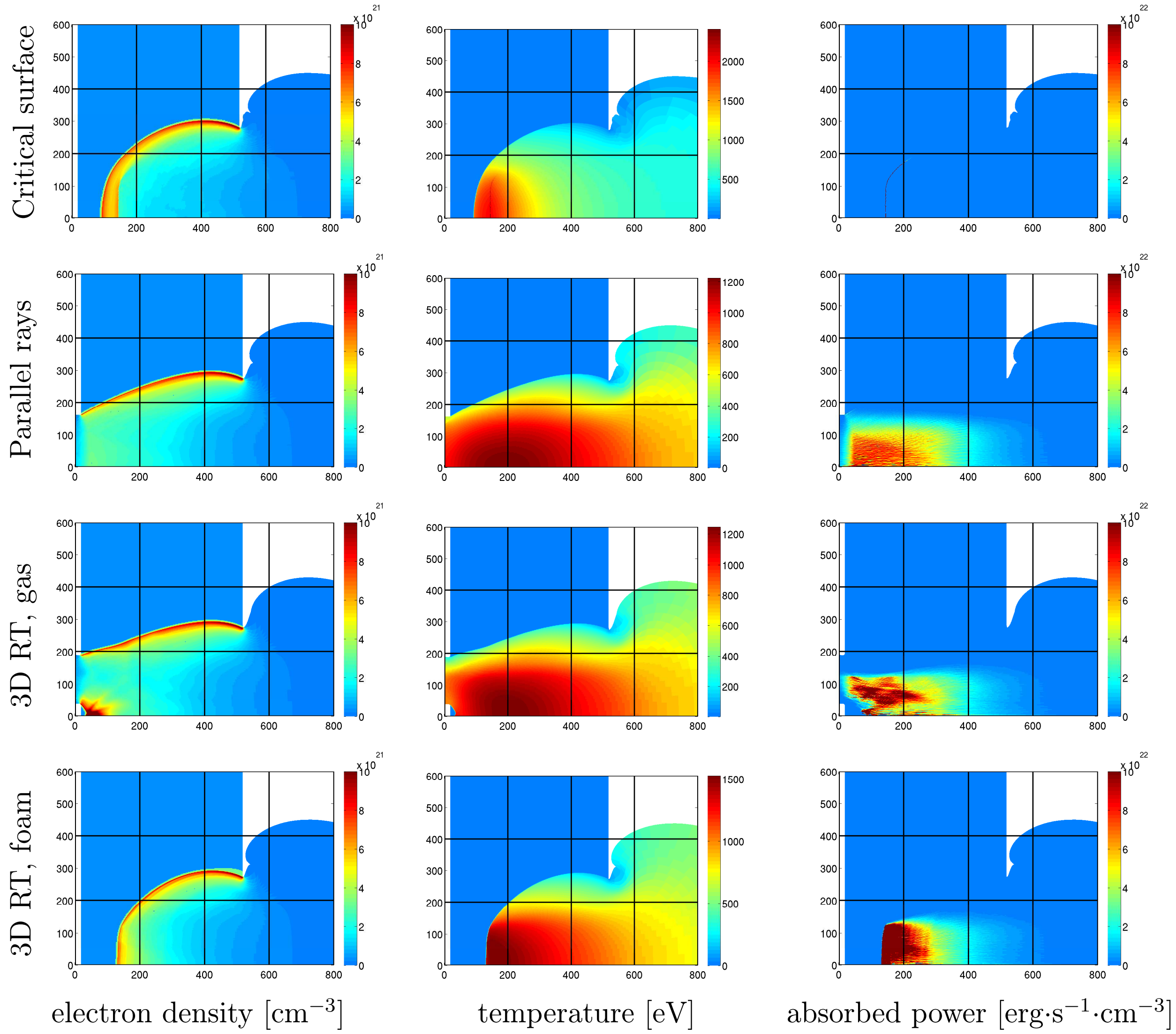

Figure 5.17.: Simulated spatial distributions of the foam plasma at 700 ps according to the different laser absorption models. The laser propagates from the right to the left.

Numerical simulations for a set of four models of laser absorption were performed. The calculated electron density, temperature and absorbed power are shown in Fig. 5.17 at the time of 700 ps. Table 5.8 presents the calculated time needed to burn through the foam according to each model. We associate the ionization front position with the cell having the temperature of 100 eV and we follow these cells up to the moment when the front reaches the rear side of the foam.

Comparing to the experimental data [75], the ionization front propagation speed is still too high for all laser absorption models. In the experiment, the propagation time of about 1.7 ns was observed with a X-ray streak camera.

For the model of parallel rays (Fig. 5.17), our density and temperature profiles match quite reasonably the results of the advanced laser–plasma code [75] at the time 500 ps. For the more detailed absorption models with the ray–tracing, we observe an artificial filamentation in the simulated plasma, which affects the plasma hydrodynamics. Our calculated propagation time of 550 ps with the parallel rays model differs from 700 ps calculated in the advanced code. This difference may be due to the difference in the definition of the ionization front position. We use the temperature–defined position in contrast to a simulated X-ray emission in the advanced code. Moreover, our target contains only a foam while the target in [75] contains also a plastic foil behind the foam. In order to explore the cause of the difference, we have performed an additional simulation with the foil attached to the rear side of the target (presented below) and calculated the foam X–ray emission.

laser absorption method	ionization front propagation time
critical surface method	800 ps
Inverse bremsstrahlung with parallel rays	550 ps
3D ray tracing with a gas target	550 ps
3D ray tracing with a foam model	900 ps

Table 5.8.: Simulated ionization front propagation time through the 500 μm foam (with respect to the 100 eV temperature). The measured propagation time is 1.7 ns.

The proposed 3D ray–tracing foam absorption model demonstrate a certain reduction of the ionization propagation speed moving it closer to the experimental measurement. However, the model fails to reproduce the experimental data for the foam with even lower–density [59]. We observe a precompression of the target, which causes a significant reduction of the front propagation speed. This effect was not observed experimentally [82]. This controversy indicates the necessity of the further improvement of the foam laser absorption model. The physical parameters could be the speed of the expansion of the foil solid elements and the thickness of the homogenization layer.

Concerning the hydrodynamic simulation with the original time–dependent absorption coefficient (4.18) 1D model [60], we observe that the plasma density and temperature profiles are similar to the simulation with the critical surface absorption model along the symmetry axis (Fig. 5.17 top). In both simulations, a shock wave is generated, thus pre–compressing the target and modifying its properties before the homogenization occurs. Thus these models are not describing correctly the real homogenization process in the foam. It should rather be driven by the laser itself or by the electron heat conductivity. The main advantage of our new multiscale model is that is includes a detailed microscopic simulation of each foam layer expansion thus providing a more realistic microscopic model compatible with the overall macroscopic simulation.

With the aim of a better comparison with the simulation results presented in [75], we conducted an additional simulation of the laser foam interaction with a 18 μm polystyrene foil attached to the rear side of the foam. A simple model of the lateral X-ray emission of the foam was included in the PALE code. We calculate the contributions to the X–ray emission of the all computational cells under the assumption of a optically thin plasma. The simulated X–ray streak camera images are presented in Fig. 5.18. Table 5.9 shows estimated light propagation time in the foam. The calculated electron density, temperature and absorbed power at the time of 1.2 ns are shown in Fig. 5.19.

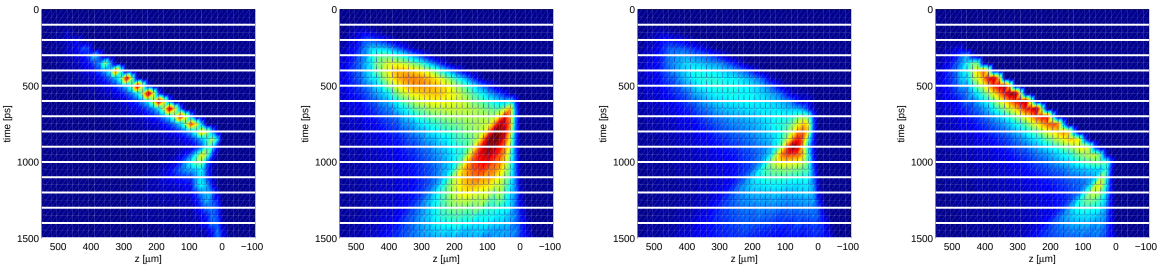

Critical surface   Parallel rays   3D RT, gas   3D RT, foam

Figure 5.18.: Modeled X-ray streak camera image of lateral foam self-emission for different laser absorption models. The laser is incident from the left.

laser absorption method	ionzation front propagation time
critical surface (600 nm wavelength)	850 ps
Inverse bremsstrahlung with parallel rays	650 ps
3D ray tracing with a gas target	700 ps
3D ray tracing with a foam model	1050 ps

Table 5.9.: Simulated laser light propagation time in the 500 μm foam with a plastic foil attached to its rear side. The front position is simulated by the X-ray self emission.

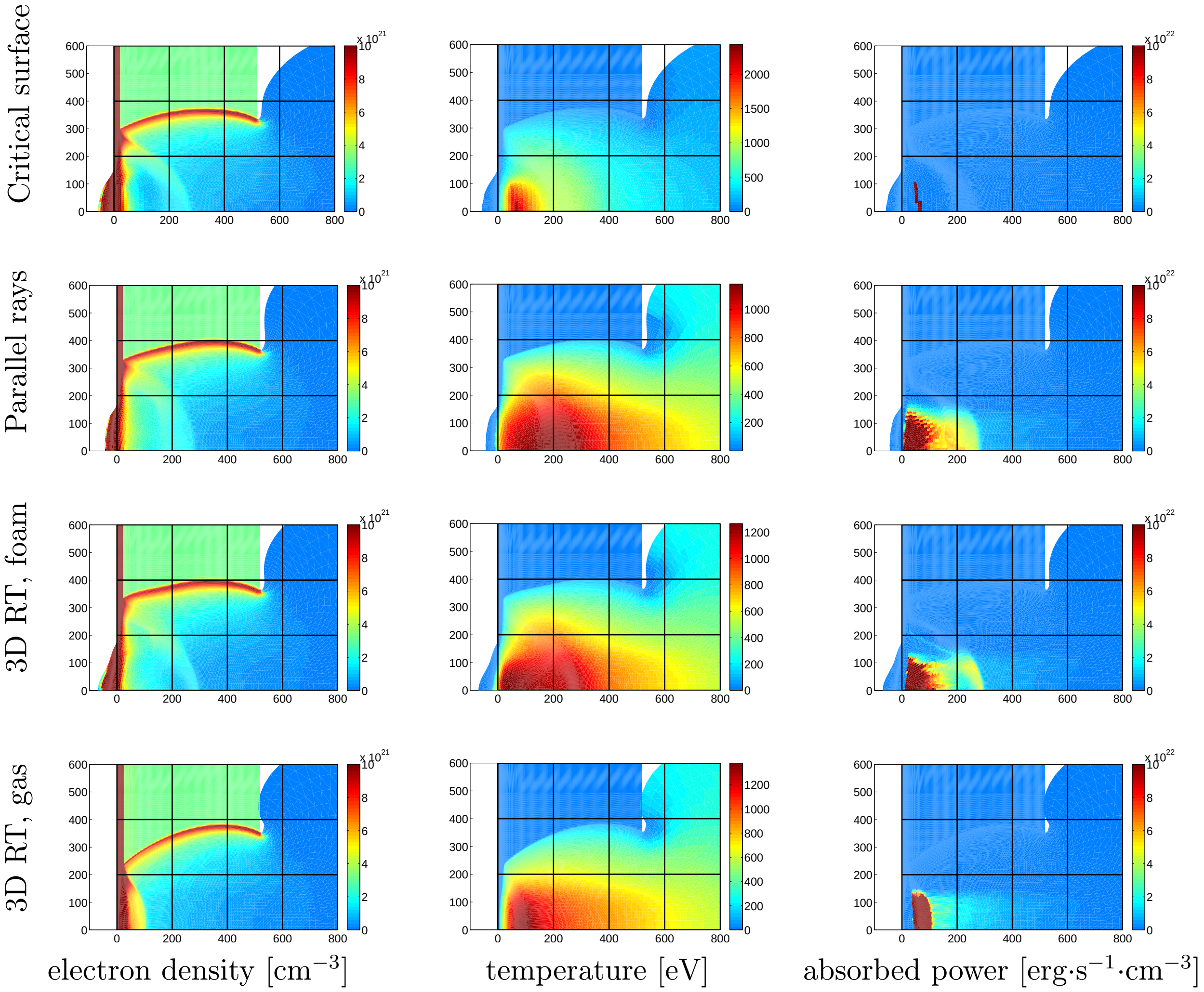

Figure 5.19.: Simulated spatial distributions of the foam plasma at 1.2 ns according to the different laser absorption models. Laser propagates from the right to the left.

A comparison of the ionization front propagation time through the foam with and without the plastic foil attached to its rear side is shown in Tab. 5.8 and Tab. 5.9. There are marginal improvements in the propagation time estimation. The front position was modeled by the foam X–ray self–emission. The propagation time is about 100 – 200 ps longer. The delay is explained by the fact that the self–emission occurs behind the ionization front once the polystyrene foil is sufficiently heated up. The ionization time calculated with the 3D ray tracing foam model is closer to the experimental data.

5.4. Numerical simulations of the PALS and GEKKO experiments

In this section, we present the numerical simulations of the real experiments of laser interaction with foam targets to demonstrate the performance of our proposed multiscale method for modeling of laser absorption in microstructured targets.

5.4.1. Target and laser setup

Three experimental setups are modeled. The first two correspond to the PALS experiments at the laser wavelength 438 nm [82, 83, 84]. The laser pulse with the Gaussian temporal profile and the FWHM (full width at halt maximum) 320 ps delivering energy of 150 – 190 J (for the simulation, we use the average value of 170 J). The focal spot has a Gaussian profile with the FWHM 300 μm. Two targets have been modeled: one is the 380 μm TAC foam with the average density 4.5 mg/cm^3 and the second – 400 μm TAC with the density 9 mg/cm^3. The different thickness of the foams is a consequence of a foam fabrication process. The chemical content of the TAC corresponds to the effective charge and mass numbers $Z = 4.54$ and $A = 8.73$. The denser foam was supplemented by the 5 μm thick Aluminum foil at the rear foam side. For the comparison with the simulation, we choose the shots no. 28193 and 28205 presented in [83].

The third setup presented in [75] consists of a 500 μm plastic foam with the mean density 10 mg/cm^3 and 18 μm polystyrene foil attached to the rear side. It was already discussed in the previous section when comparing different models of laser absorption. The foam with the effective charge/mass number $Z/A = 3.85/7.22$ was heated up by the 350 nm GEKKO laser radiation. The 300 J pulse has a triangular temporal shape with 400 ps rise and 3 ns down time. The spatial profile is described by a 6th order super–Gaussian function with a 100 μm radius.

5.4.2. Results

The numerical simulation is performed with the PALE [5] code. The electron density, temperature and absorbed–energy distributions are shown in Fig. 5.22 for the time 450 ps. The simulated X-ray streak camera images of a lateral foam self-emission are presented in Fig. 5.20. Experimental images are presented in Fig. 5.21. These numerical simulations for the three different parameters show good scaling and qualitative agreement with the experiments [75, 83]. The lowest–density foam in Fig. 5.20 (left) is ionized during the laser pulse duration. The laser penetration through the higher-density foam (center) is slower and the rear-side foil self-emission occurs at around 1.3 ns, after the end of the laser pulse.

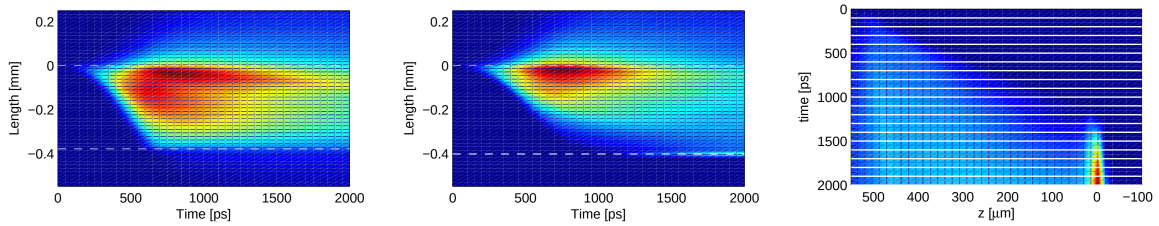

PALS 4.5 mg/cm^3 PALS 9 mg/cm^3 GEKKO 10 mg/cm^3

Figure 5.20.: Simulated X–ray streak camera image of the lateral foam self–emission.

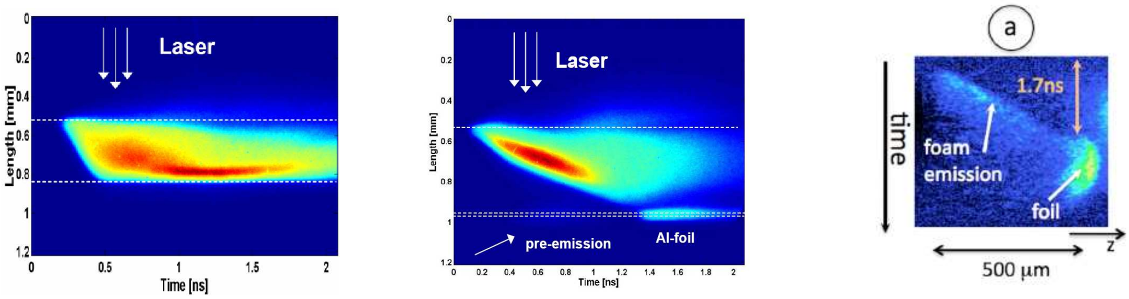

PALS 4.5 mg/cm^3 PALS 9 mg/cm^3 GEKKO 10 mg/cm^3

Figure 5.21.: Observed X–ray streak camera image of the lateral foam self–emission [75, 83].

Proposed in section 4.3 modifications of the hydrodynamic model describe the microscopic foam homogenization and allows to avoid the foam pre–compression. These modifications are crucial allowing for the first time to reproduce a correct speed of laser penetration for the lightest foam (4.5 mg/cm^3). Previous models fail to reproduce this

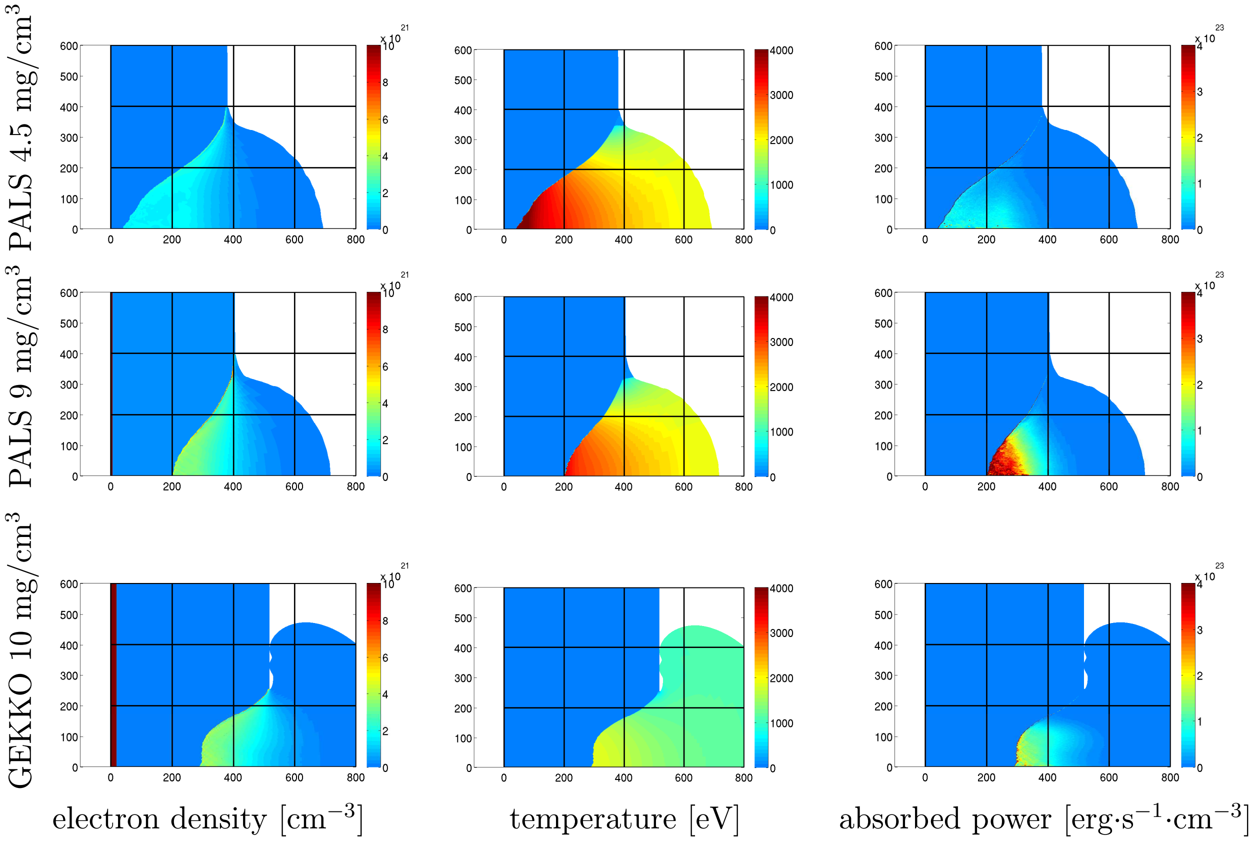

Figure 5.22.: Simulated spatial distributions of the foam plasma at 450 ps according to the different laser absorption models. Laser propagates from the right to the left.

case because of a strong shock generated upstream the ionization front resulting in an incorrect microscopic layer expansion speed.

The suggested multiscale model reproduces the laser–front propagation as well as the detailed hydrodynamic simulation directly resolving the microscopic foam structure [59]. One dimensional structural representation of a foam with several cells in each microscopic dense layer and a low–density pore provides a detail description of the homogenization process. However, this model is numerically expensive and cannot be extended to a real experimental case. On the contrary, our multiscale model needs much less computational cells to reproduce a correct homogenization time and it is more robust providing possibility to run simulations in a realistic nanosecond regime.

A smoothing of large scale inhomogenities in the laser beam intensity distribution during its propagation through sub–critical foam layers can be explained by both the laser–ray refraction and the heat conductivity effects. These effects need to be studied in future research.

6. Summary

In the main part of this thesis, we have presented the high–order remapping method for the system of Euler equations describing the behavior of an inviscid compressible fluid, applicable e.g. for the laser–produced plasma. Issues related to the symmetry– and bound–preservation of the method as well as the high–order of accuracy are investigated. The method is tested on standard cyclic–remapping problems. Incorporated in the complete Arbitrary Lagrangian–Eulerian (ALE) method, the performance of the remap is further demonstrated in the cell–centered code CHLER [10] for the standard hydrodynamic test cases. Our remapping method using a piecewise quadratic reconstruction and a Symmetric Flux–Corrected Transport ideas is directly applicable to unstructured two–dimensional computational meshes with the fixed mesh topology. Vector limiters preserving a radial symmetry of the radial fields on polar meshes are described in detail in the context of the reconstruction limiting during the remapping step of the ALE method. Symmetry– and bound–preserving modifications of the limiters are numerically tested in the staggered hydrodynamic code PALE [5].

Particular aspects of the laser interaction with low–density foam targets are addressed in the remaining part of the thesis. Hydrodynamic simulations of the microstructured target materials require a specific treatment of the laser absorption and the material response. The method of a local time–dependent absorption coefficient [60] is generalized to be applicable in the two–dimensional cylindrically–symmetric hydrodynamic codes, as e.g. PALE [5]. The generalization includes implementation of the 3D ray–tracing algorithm and a sub–cycled simulation of the expansion of solid foam elements induced by the laser and electron energy fluxes. This new model is tested in the numerical simulations of the laser–foam interaction experiments performed at the PALS [6] and GEKKO [4] laser facilities. These simulations demonstrate the practical interest of the model and of the application part of this thesis. Contrary to the standard hydrodynamic simulations of a foam as a homogeneous material, presented results open a new approach of efficient modeling of microstructured materials. They show a good agreement of the ionization front speed in the sub–critical foam with the experiments.

The detailed numerical simulations of the laser–generated plasmas are out of scope of this thesis. Instead of this, we address the key elements of the particular numerical methods required to perform more efficient and accurate simulations.

The main contribution and the new ideas of the thesis can be summarized to:

- Comparative study of the 1D slope limiters for a piecewise parabolic reconstruction in the remapping context.
- Investigation and development of the slope limiters for vectors and their application in the remapping step of the ALE method.
- Development of a new high–order symmetry–preserving remapping algorithm for the Euler equations enforcing the bounds preservation without artificial repair techniques.
- Development and implementation of the laser–absorption methods in the hydrodynamic code PALE.
- Development of a new reliable numerical method for modeling of the laser interaction with low–density foams.

These particular results are achieved in the context of the research programs of the Department of Physical Electronics of the Czech Technical University in Prague and the Center for Intense Lasers and Applications of the Bordeaux University. They contribute to the development of reliable numerical methods for laser plasma modeling.

6.1. Conclusions for further research

In the future research, the symmerty– and bound–preserving high–order remapping method could be extended in 3D and to the computational meshes with changing topology. Thanks to the construction of the method, these extensions are rather straightforward. In particular, the application of the remapping method in the Reconnection ALE (ReALE) scheme [31], has a potential to improve the ReALE performance.

The slope limiters for vectors are widely applied in non–linear high–order hydrodynamic methods. The described symmetry– and bounds–preserving modifications of the limiters may find application whenever possible outside the remapping methods.

The new laser–absorption model for low–density foams can be applied in future studies of the laser–beam smoothing and hydrodynamic modeling of other microstructured materials. This opens a way for new more efficient numerical models for the future ICF research.

Bibliography

[1] I. Štoll. *Dějiny fyziky*. Prometeus, Praha, 2009.

[2] E. I. Moses. Ignition on the National Ignition Facility. volume 112 of *Journal of Physics Conference Series*, page 012003, 2008.

[3] K. Mima, V. Tikhonchuk, and M. Perlado. Inertial fusion experiments and theory. *Nucleal Fusion*, 51:094004, 2011.

[4] N. Miyanaga at al. The GEKKO XII - HIPER (High Intensity Plasma Experimental Research) System Relevant to Ignition Target. Sorrento, 2000.

[5] R. Liska, J. Limpouch, M. Kuchařík, and O. Renner. Selected laser plasma simulations by ALE method. *Journal of Physics: Conference Series*, 112(2):022009, 2008.

[6] Jungwirth at al. The Prague Asterix Laser System. *Physics of Plasmas*, 8(5):2495–2501, 2001.

[7] O. Klimo and V.T. Tikhonchuk. Laser–plasma interaction studies in the context of shock ignition: the regime dominated by parametric instabilities. *Plasma Physics and Controlled Fusion*, 55(9):095002, 2013.

[8] M. Kuchařík. *Arbitrary Lagrangian–Eulerian (ALE) methods in plasma physics.* Ph.D. Disertation thesis, Czech Technical University in Prague, 2006.

[9] S. Clain, S. Diot, and R. Loubere. A high-order finite volume method for systems of conservation laws–multi-dim. optimal order detection (MOOD). *Journal of Computational Physics*, 230(10):4028–4050, 2011.

[10] P.-H. Maire, J. Breil, and S. Galera. A cell-centred arbitrary lagrangian–eulerian (ALE) method. *International Journal for Numerical Methods in Fluids*, 56(8):1161–1166, 2008.

[11] P.-H. Maire, R. Abgrall, J. Breil, and J. Ovadia. A cell-centred Lagrangian scheme for two-dimensional compressible flow problems. *SIAM Journal on Scientific Computing*, 29:1781–1824, 2007.

[12] T. J. Barth and D. Jespersen. The design and application of upwind schemes on unstructured meshes. Technical Report AIAA-89-0366, NASA Ames Research Center, 1989.

[13] J. Falcovitz M. Ben-Artzi. *Generalized Riemann Problems in Computational Fluid Dynamics*. Cambridge university press, 2003.

[14] P.-H. Maire. A high-order cell-centered Lagrangian scheme for two-dimensional compressible fluid flows on unstructured meshes. *Journal of Computational Physics*, 228: 2391–2425, 2009.

[15] P.-H. Maire. A high-order cell-centered Lagrangian scheme for compressible fluid flows in two-dimensional cylindrical geometry. *Journal of Computational Physics*, 228:6882–6915, 2009.

[16] P.-H. Maire and B. Nkonga. Multi-scale Godunov-type method for cell-centered discrete Lagrangian hydrodynamics. *Journal of Computational Physics*, 228:799–821, 2009.

[17] G. Carre, S. Del Pino, B. Despres, and E. Labourasse. A cell-centered Lagrangian hydrodynamics scheme on general unstructured meshes in arbitrary dimension. *Journal of Computational Physics*, 228:5160–5183, 2009.

[18] F. Vilar, P.H. Maire, and R. Abgrall. Cell-centered discontinous Galerkin discretizations for two-dimensional scalar conservation laws on unstructured grids and for one-dimensional Lagrangian hydrodynamics. *Computers & Fluids*, 46:498–504, 2011.

[19] F. Vilar. *A high-order Discontinuous Galerking discretization for solving two-dimenzional Lagrangian hydrodynamics*. Ph.D. thesis, Université Bordeaux I, 2012.

[20] J. Velechovský. *Numerické metody modelování laserového plazmatu*. Diploma thesis, Czech Technical University in Prague, 2011.

[21] R. Liska, M. Kucharik, J. Limpouch, O. Renner, P. Vachal, L. Bednarik, and J. Velechovsky. ALE Method for Simulations of Laser-Produced Plasmas. In Fort, J and

Furst, J and Halama, J and Herbin, R and Hubert, F, editor, *Finite Volumes for Complex Applications VI - Problems & Perspectives, Vol. 1 and 2*, Springer Proceedings in Mathematics, pages 857–873, 2011.

[22] E. J. Caramana, M. J. Shashkov, and P. P. Whalen. Formulations of artificial viscosity for muti-dimensional shock wave computations. *Journal of Computational Physics*, 144(2):70–97, 1998.

[23] E. J. Caramana, D. E. Burton, M. J. Shashkov, and P. P. Whalen. The construction of compatible hydrodynamics algorithms utilizing conservation of total energy. *Journal of Computational Physics*, 146(1):227–262, 1998.

[24] P. Váchal. *Rezoning and remapping for ALE simulations in fluid dynamics and plasma physics.* Ph.D. Disertation thesis, Czech Technical University in Prague, 2008.

[25] V.A. Dobrev, T.V. Kolev, and R.N. Rieben. High-order curvilinear finite element methods for lagrangian hydrodynamics. *SIAM Journal on Scientific Computing*, 34: B606–B641, 2012.

[26] D. J. Benson. Computational methods in Lagrangian and Eulerian hydrocodes. *Computer Methods in Applied Mechanics and Engineering*, 99(2-3):235–394, 1992.

[27] L. G. Margolin. Introduction to "An arbitrary Lagrangian-Eulerian computing method for all flow speeds". *Journal of Computational Physics*, 135(2):198–202, 1997.

[28] J. S. Peery and D. E. Carroll. Multi-material ALE methods in unstructured grids. *Computer Methods in Applied Mechanics and Engineering*, 187(3-4):591–619, 2000.

[29] R. W. Anderson, N. S. Elliott, and R. B. Pember. An arbitrary Lagrangian-Eulerian method with adaptive mesh refinement for the solution of the Euler equations. *Journal of Computational Physics*, 199(2):598–617, 2004.

[30] J. M. Morrell, P. K. Sweby, and A. Barlow. A cell by cell anisotropic adaptive mesh ALE scheme for the numerical solution of the Euler equations. *Journal of Computational Physics*, 226(1):1152–1180, 2007.

[31] R. Loubere, P.-H. Maire, M. Shashkov, J. Breil, and S. Galera. ReALE: A reconnection-based arbitrary-Lagrangian-Eulerian method. *Journal of Computational Physics*, 229(12):4724–4761, 2010.

[32] S. Galera, P.-H. Maire, and J. Breil. A two-dimensional unstructured cell-centered multi-material ALE scheme using VOF interface reconstruction. *Journal of Computational Physics*, 229(16):5755–5787, 2010.

[33] O. Renner at al. Environmental conditions in near-wall plasmas generated by impact of energetic particle fluxes. *High Energy Density Physics*, 9:568–572, 2013.

[34] C. W. Hirt, A. A. Amsden, and J. L. Cook. An arbitrary Lagrangian-Eulerian computing method for all flow speeds. *Journal of Computational Physics*, 14(3): 227–253, 1974. Reprinted in JCP, 135:203-216, 1997.

[35] R. Liska, M. Shashkov, P. Váchal, and B. Wendroff. Synchronized flux corrected remapping for ALE methods. *Computers & Fluids*, 46(1):312–317, 2011.

[36] M. Berndt, J. Breil, S. Galera, M. Kucharik, P.-H. Maire, and M. Shashkov. Two step hybrid remapping (conservative interpolation) for multimaterial arbitrary Lagrangian-Eulerian methods. *Journal of Computational Physics*, 230(17):6664–6687, 2010.

[37] P. Colella and M.D. Sekora. A limiter for PPM that preserves accuracy at smooth extrema. *Journal of Computational Physics*, 227:7069–7076, 2008.

[38] L. G. Margolin and M. Shashkov. Second-order sign-preserving conservative interpolation (remapping) on general grids. *Journal of Computational Physics*, 184(1): 266–298, 2003.

[39] B. van Leer. Towards the ultimate conservative difference scheme I. The quest of monotonicity. *Springer lecture notes in Physics*, 18:163–168, 1973.

[40] M. Kucharik, M. Shashkov, and B. Wendroff. An efficient linearity-and-bound-preserving remapping method. *Journal of Computational Physics*, 188:462–471, 2003.

[41] T. J. Barth. Numerical methods for gasdynamic systems on unstructured meshes. In C. Rohde D. Kroner, M. Ohlberger, editor, *An introduction to Recent Developments in Theory and Numerics for Conservation Laws, Proceedings of the International*

School on Theory and Numerics for Conservation Laws, Berlin, 1997. Lecture Notes in Computational Science and Engineering, Springer. ISBN 3-540-65081-4.

[42] G. Luttwak and J. Falcovitz. Slope limiting for vectors: A novel vector limiting algorithm. *International Journal for Numerical Methods in Fluids*, 65(11-12):1365–1375, 2011.

[43] G. Luttwak and J. Falcovitz. Vector image polygon (VIP) limiters in ale hydrodynamics. *European Physical Journal Web of Conferences*, 10:00020, 2010.

[44] G. Luttwak and J. Falcovitz. VIP (vector image polygon) multi-dimensional slope limiters for scalar variables. *Computers & Fluids*, 83:90–97, 2013.

[45] P.-H. Maire. *Contribution to the numerical modeling of Inertial Confinement Fusion.* Habilitation thesis, Université Bordeaux I, 2011. http://tel.archives-ouvertes.fr/docs/00/58/97/58/PDF/hdr_main.pdf.

[46] P.-H. Maire. A high-order one-step sub-cell force-based discretization for cell-centered Lagrangian hydrodynamics on polygonal grids. *Computers & Fluids*, 46(1):341–347, 2011.

[47] P.-H. Maire, R. Loubère, and P. Váchal. Staggered Lagrangian discretization based on cell-centered Riemann solver and associated hydrodynamics scheme. *Communications in Computational Physics*, 10(4):940–978, 2011.

[48] J. Boris and D. Book. Flux-corrected transport I: SHASTA, a fluid transport algorithm that works. *Journal of Computational Physics*, 11(1):38–69, 1973. Reprinted in JCP, 135:172-186, 1997.

[49] S. T. Zalesak. Fully multidimensional flux-corrected transport algorithms for fluids. *Journal of Computational Physics*, 31(3):335–362, 1979.

[50] D. Kuzmin, R. Löhner, and S. Turek, editors. *Flux-Corrected Transport. Principles, Algorithms and Applications.* Springer Verlag, Berlin, Heidelberg, 2nd edition, 2012.

[51] P. Váchal and R. Liska. Sequential flux-corrected remapping for ALE methods. In A. Bermúdez de Castro, D. Gómez, P. Quintela, and P. Salgado, editors, *Numerical Mathematics and Advanced Applications. ENUMATH 2005.* Springer Berlin, 671-679, 2006.

[52] R. Liska, M. Shashkov, P. Váchal, and B. Wendroff. Optimization-based synchronized flux-corrected conservative interpolation (remapping) of mass and momentum for arbitrary Lagrangian-Eulerian methods. *Journal of Computational Physics*, 229(5): 1467–1497, 2010.

[53] P. Bochev and D. Ridzal nad M. Shashkov. Fast optimization-based conservative remap of scalar fields through aggregate mass transfer. *Journal of Computational Physics*, 246:37–57, 2013.

[54] P. Bochev and D. Ridzal nad K. Peterson. Optimization-based remap and transport: A divide and conquer strategy for feature-preserving discretizations. *Journal of Computational Physics*, 257:1113–1139, 2014.

[55] T. B. Kaiser. Laser ray tracing and power deposition on an unstructured three-dimensional grid. *Physical Revue E*, 61:895–905, 2000.

[56] A. Colaitis, G. Duchateau, P. Nicolai, and V. Tikhonchuk. Towards modeling of non-linear laser-plasma interactions with hydrocodes: The thick-ray approach. *Physical Review E*, 89(033101), 2014.

[57] M. Desselberger, M.W. Jones, and J. Edwards et al. Use of X-ray preheated foam layers to reduce beam structure imprint in laser-driven targets. *Physical Review Letters*, 74:2961–2964, 1995.

[58] M. Kalal, J. Limpouch, and E. Krousky et al. Thermal smoothing by laser-produced plasma of porous matter. *Fusion science and technology*, 43:275–281, 2003.

[59] T. Kapin, M. Kucharik, J. Limpouch, and R. Liska. Hydrodynamic simulations of laser interactions with low-density foams. *Czechoslovak Journal of Physics*, 56: B4593–B4598, 2006.

[60] S. Guskov, J. Limpouch, Ph. Nicolai, and V. Tikhonchuk. Laser-supported ionization wave in under-dense gases and foams. *Physics of plasmas*, 18:103114, 2011.

[61] C. B. Laney. *Computational gasdynamics.* Cambridge university press, New York, 1998.

[62] V. Venkatakrishnan. Convergence to steady state solutions of the Euler equations on unstructured grids with limiters. *Journal of Computational Physics*, 118:120–130, 1995.

[63] Ch. Michalak and C. Ollivier-Gooch. Accuracy preserving limiter for the high-order accurate solution of the Euler equations. *Journal of Computational Physics*, 228: 8693–8711, 2009.

[64] M. Yang and Z.J. Wang. A parameter-free generalized moment limiter for high- order methods on unstructured grids. In *47th AIAA Aerospace Sciences Meeting Including The New Horizons Forum and Aerospace Exposition*, AIAA, 1-22. AIAA, 2009.

[65] D. Kuzmin. A vertex-based hierarchical slope limiter for p-adaptive discontinuous Galerkin methods. *Journal of Computational and Applied Mathematics*, 233(12): 3077–3085, 2010.

[66] A. Nejat. *A Higher-Order Accurate Unstructured Finite Volume Newton-Krylov Algorithm for Inviscid Compressible Flows.* PhD thesis, University of British Columbia, 2007.

[67] P. Colella and P.R. Woodward. The piecewise parabolic method (PPM) for gas-dynamical simulations. *Journal of Computational Physics*, 54:174–201, 1984.

[68] L. White and A. Adcroft. A high-order finite volume remapping scheme for nonuniform grids: The piecewise quartic method (PQM). *Journal of Computational Physics*, 227:7394–7422, 2008.

[69] R. Loubere and M. Shashkov. A subcell remapping method on staggered polygonal grids for arbitrary-Lagrangian-Eulerian methods. *Journal of Computational Physics*, 209(1):105–138, 2005.

[70] M. Shashkov and B. Wendroff. The repair paradigm and application to conservation laws. *Journal of Computational Physics*, 198(1):265–277, 2004.

[71] M. Kucharik and M. Shashkov. Flux-based approach for conservative remap of multi-material quantities in 2D arbitrary Lagrangian-Eulerian simulations. In J. Fořt, J. Fürst, J. Halama, R. Herbin, and F. Hubert, editors, *Finite Volumes for Complex Applications VI - Problems & Perspectives, Vol. 1*, Springer Proceedings in Mathematics, pages 623–631. Springer, 2011.

[72] P. Vachal. *2D Flux-Corrected Remapping of Momentum with Velocity Bounds Preserved in General Direction.* private communication, 2011.

[73] I. G. Lebo, N. N. Demchenko, A. B. Iskakov, J. Limpouch, V. B. Rozanov, and V. F. Tishkin. Simulation of high-intensity laser–plasma interactions by use of the 2D Lagrangian code ATLANT-HE. *Laser and Particle Beams*, 22:267–273, 2004.

[74] B. van der Holst at al. Simulating radiative shock with the CRASH laser package. *High Energy Density Physics*, 9:8–16, 2013.

[75] S. Fujioka A. Sunahara N. Borisenko S. Guskov A. Orekov M. Grech G. Riazuelo C. Labaune J. Velechovsky Ph. Nicolai, M. Olazabal-Loume and V. Tikhonchuk. Experimental evidence of foam homogenization. *Physics of Plasmas*, 19:113105, 2012.

[76] L. I. Sedov. *Similarity and Dimensional Methods in Mechanics*. Academic Press, 1959.

[77] G. Scovazzi, E. Love, and M. Shashkov. Multi-scale Lagrangian shock hydrodynamics on Q1/P0 finite elements: Theoretical framework and two-dimensional computations. *Computer Methods in Applied Mechanics and Engineering*, 197(9-12): 1056–1079, 2008.

[78] M. Kucharik and M. Shashkov. Conservative multi-material remap for staggered discretization. *Journal of Computational Physics*, 258:268–304, 2014.

[79] G. A. Sod. A survey of several finite difference methods for systems of nonlinear hyperbolic conservation laws. *Journal of Computational Physics*, 27:1–31, 1978.

[80] J.R. Kamm and F.X. Timmes. On efficient generation of numerically robust sedov solutions. Technical Report LA-UR-07-2849, Los Alamos National Laboratory, 2007.

[81] R. M. More, K. Warren, D. Young, and G. Zimmerman. A new quotidian equation of state (qeos) for hot dense matter. *Physics of Fluids*, 10:3059–3078, 1988.

[82] A. M. Khalenkov, N. G. Borisenko, V. N. Kondrashov, Yu. A. Merkuliev, J .Limpouch, and V. G. Pimenov. Experience of micro-heterogeneous target fabrication to study energy transport in plasma near critical density. *Laser and Particle Beams*, 24:283–290, 2006.

[83] J. Limpouch at al. Laser absorption and energy transfer in foams of various pore structures and chemical compositions. *Journal de Physique IV France*, 133:457–459, 2006.

[84] N. G. Borisenko, I. V. Akimova, A. I. Gromov, A. M. Khalenkov, and Yu. A. Merkuliev. Regular 3-D networks with clusters for controlled energy transport studies in laser plasma near critical density. *Fusion Science and Technology*, 49:676–685, 2006.

A. List of publications

Impacted Journals

[a1] J. Velechovsky, J. Breil, and R. Liska. Flux corrected remapping using piecewise parabolic reconstruction for 2D cell-centered ALE methods. *International Journal for Numerical Methods in Fluids*, **76**:575–586, 2014.

[a2] J. Velechovsky, M. Kucharik, R. Liska, M. Shashkov, and P. Vachal. Symmetry- and essentially-bound-preserving flux-corrected remapping of momentum in staggered ALE hydrodynamics. *Journal of Computational Physics*, **255**:590–611, 2013.

[a3] J. Velechovsky, R. Liska, and M. Shashkov. High-order remapping with piece-wise parabolic reconstruction. *Computers and Fluids*, **83**:164–169, 2013.

→ O. Renner, M. Smid, T. Burian, L. Juha, J. Krasa, E. Krousky, I. Matulkova, J. Skala, A. Velyhan, R. Liska, J. Velechovsky, T. Pisarczyk, T. Chodukowski, O. Larroche, and J. Ullschmied. Environmental conditions in near-wall plasmas generated by impact of energetic particle fluxes. *High Energy Density Physics*, **9**(3):568–572, 2013.

→ Ph. Nicolai, M. Olazabal-Loume, S. Fujioka, A. Sunahara, N. Borisenko, S. Guskov, A. Orekov, M. Grech, G. Riazuelo, C. Labaune, J. Velechovsky, and V. Tikhonchuk. Experimental evidence of foam homogenization. *Physics of Plasmas*, **19**(11):113105, 2012.

Others

[a4] J. Velechovsky, R. Liska, and V. Tikhonchuk. Arbitrary Lagrangian–Eulerian hydrodynamic method for laser plasma modeling. *Kudowa Summer School "Towards Fusion Energy" Programme and Contributions*, 61–62, Institute of Plasma Physics, Warsaw, 2014.

[a5] J. Velechovsky, M. Kucharik, R. Liska, and M. Shashkov. Symmetry-preserving momentum remap for ALE hydrodynamics. *Journal of Physics Conference Series (IUPAP-CCP 2012)*, **454**:012003, 2013.

→ J. Velechovsky, M. Kucharik, R. Liska, M. Shashkov, and P. Vachal. Symmetry-preserving Remap of Vectors for Stagerred ALE Hydrodynamics. *Journee de l'Ecole Doctorale*, Universite de Bordeaux, 118, 2013.

→ O. Renner, J. Cihelka, L. Juha, J. Krasa, E. Krousky, J. Nejdl, J. Skala, A. Velyhan, T. Pisarczyk, T. Chodukowski, Z. Kalinowska, A. Kasperczuk, P. Pisarczyk, R. Liska, M. Šmíd, P. Vachal, J. Velechovsky, and J. Ullschmied. Plasma Jets Production at Laser-Burnt-Through Foils and their Interaction with Secondary Targets. In *Proceedings of the 5th International Conference on Frontiers of Plasma Physics and Technology*, IAEA Vienna, 2013.

→ R. Liska, M. Kucharik, J. Limpouch, O. Renner, P. Vachal, L. Bednarik, and J. Velechovsky. ALE Method for Simulations of Laser-Produced Plasmas. In Fort, J and Furst, J and Halama, J and Herbin, R and Hubert, F, editor, *Finite Volumes for Complex Applications VI: Problems and Perspectives, vols 1 and 2*, volume 4 of *Springer Proceedings in Mathematics*, 857–873, Springer-Verlag Berlin, 2011.

→ H. Jelinkova, L. Bednarik, M. Drahokoupil, M. Duspiva, M. Fibrich, J. Havlik, M. Holec, M. Jelinek, O. Kitzler, J. Kodet, P. Koranda, P. Matlas, V. Michalek, P. Navratil, M. Nemec, D. Vyhlidal, P. Szotkowski, M. Vacek, J. Velechovsky, J. Blazej, M. Cech, V. Kubecek, M. Kucharík, R. Liska, A. Novotny, I. Prochazka, M. Sinor, J. Sulc, and P. Vachal. Lasery a aplikace. In *Workshop 2011*, number SGS10/299/OHK4/3T/14, pages 1–6. Czech Technical University in Prague, 2011.

→ O. Renner, J. Cihelka, L. Juha, E. Krousky, J. Nejdl, J. Skala, A. Velyhan, T. Pisarczyk, T. Chodukowski, P. Pisarczyk, R. Liska, M. Smid, P. Vachal, J. Velechovsky, J. Ullschmied, O. Larroche, and E. Dalimier. Spectroscopic diagnosis of energetic plasma jets interaction with walls. In *14th International Workshop on Radiative Properties of Hot Dense Matter*, Universidad Politechnica de Madrid, 20, 2010.

A.1. Oral presentations

- ECCOMAS 6th European Conference on Computational Fluid Dynamics, July 25, 2014, Barcelona, Spain.
- 12th Kudowa Summer School "Towards Fusion Energy", June 9, 2014, Poland.
- Seminar at Centre Lasers Intenses et Applications, June 20, 2013, Talence, France.

A.2. Poster presentations

- MultiMat 2013, September 4, 2013, San Francisco, USA.
- Journée de l'Ecole Doctorale, March 5, 2013, Talence, France.
- CCP2012, Conference on Computational Physics, October 16, 2012, Kobe, Japan.

B. Résumé substantiel en français

B.1. Contexte de la recherche

Les méthodes numériques, à savoir les procédures de résolution de problèmes mathématiques en général, sont utilisés avec succès pour des milliers d'années. Probablement la plus ancienne preuve connue d'entre elles est la table de Babylone montrant un algorithme pour calculer la racine carrée du nombre deux. Méthodes numériques ordinaires, qui sont enseignées dans les universités techniques, sont datés à la période de 17. à 19. siècle, la période de croissance de la mécanique classique. Leurs noms, par exemple la méthode de Newton, Lagrange polynomiale, élimination de Gauss ou méthode d'Euler, sont la preuve claire de cela. Cependant, le plus grand développement des méthodes numériques a commencé dans les années 1940, lorsque les premiers ordinateurs sont devenus disponibles. Incroyablement rapide et gratuit–de–erreurs ordinateurs ont remplacé le non–facteur humain efficace dans les procédures. Le travail de personnes a été transféré de l'exécution à l'élaboration de nouvelles méthodes. Les méthodes numériques sont devenus largement appliquée dans le large éventail de la science et de la technologie. Gamme applicable des méthodes numériques a été d'élargir encore par l'invention de la haute–classe pour des méthodes. Exigences inférieures du temps de calcul et la mémoire des haut les modes de commande permettent leur application, même pour les systèmes complexes, tels que le plasma produit par de hautes installations laser de puissance.

Ce travail est dédié aux méthodes numériques pour laser–plasma modélisation de l'interaction. Plus précisément, la thèse traite le plasma créé par l'interaction d'une impulsion laser intense avec la matière. Plus précisément, on développe les méthodes pour résoudre les équations hydrodynamiques, compte tenu du plasma comme fluide compressible avec d'autres procédés physiques tels que l'absorption de la lumière laser ou la conduction de chaleur. Le modèle hydrodynamique compromis entre une description physique détaillée et une efficacité de calcul. L'efficacité est cruciale pour les simulations de processus complexes comme le laser–importance des expériences d'interaction.

Expériences d'interaction laser-plasma couvrent généralement une large gamme de paramètres physiques. La densité caractéristique varie d'une limite de vide pour quelques fois la densité à l'état solide et les échelles de température de quelques milliers à centaines de millions de degrés Celsius ou Kelvin. La recherche sur de tels états de densité d'énergie élevée de l'affaire a commencé environ 15 ans avant la découverte d'un laser lui-même lorsque la libération d'une quantité énorme d'énergie dans les réactions nucléaires de fission et de fusion plus tard, a été réalisé dans des explosions. Une réduction supplémentaire des expériences de plasma et un contrôle possible de l'énergie libérée a été activé par la découverte des lasers en tant que source d'énergie à haute puissance. Les densités d'énergie suffisantes pour les modifications de matériau solide et la production de plasma ont été atteints dans les années 1960. Depuis, de nombreuses applications pratiques de la matière d'interaction laser ont été proposés. Le plus difficile parmi eux serait une libération de l'énergie thermonucléaire dans une cible d'hydrogène comprimé par un puissant lasers. Tel est l'objectif pour les laboratoires de recherche haut du monde.

B.2. Objectif de la thèse

L'objectif général de la thèse est de contribuer à l'état de la connaissance de l'art dans les haut–méthodes numériques afin ALE, remappage en particulier, pour les équations d'Euler et de l'application des méthodes de ALE pour la modélisation des processus d'interaction plasma laser.

La diffusion numérique lors de l'étape de reconfiguration nécessaire du procédé ALE est réduite par développés methodes remappage d'ordre eleve. La conservation de la symétrie des méthodes pour les vecteurs limitation est étudiée en détail dans le cas des flux radiaux. Ces questions ont été récemment largement discutés par la communauté de calcul de dynamique des fluides.

Comme une application particulière, une interaction d'un rayonnement laser avec une cible de mousse à faible densité est étudiée. Des expériences avec des mousses microstructurées ayant la densité moyenne de quelques mg/cm^3 montrent une amélioration significative de la qualité d'un faisceau laser et son lissage après propagation à travers une mousse. Ce lissage est essentiel pour les applications fusion par confinement inertiel (ICF), car elle permet de réaliser une bien meilleure qualité de l'implosion. Le mécanisme physique exact de l'ionisation de mousse par la lumière laser est de nature microscopique et codes hydrodynamiques standard, qui envisagent la mousse comme un média en continu d'une densité équivalente, surestimer la vitesse de la pénétration du laser dans les mousses.

Dans cette thèse, nous proposons un nouveau modèle de mousse ionisation et une modification de la méthode d'absorption de l'énergie laser. Il représente la structure de mousse microscopique dans le modèle hydrodynamique continue standard. Ce nouveau modèle correspond aux résultats expérimentaux de l'interaction laser–mousse. Ces modifications ont été atteints par la mise en œuvre d'un algorithme de ray-tracing 3D en 2D cylindrique symétrique code PALE.

B.3. Démarche adoptée

Dans la partie principale de cette thèse, nous avons présenté la méthode de reconfiguration de l'ordre eleve pour le système d'équations d'Euler décrivant le comportement d'un fluide non visqueux compressible, par exemple applicable pour le laser–plasma. Les questions liées à l'symmetry et lié la préservation de la méthode ainsi que la haute ordre de précision sont étudiées. La méthode est testée sur cycliques standards – problèmes remappage. Incorporé dans l'arbitraire complet Lagrange–Euler méthode (ALE), la performance de la reconfiguration est également démontré dans la cellule centrée Code CHLER pour les cas de tests hydrodynamiques standard. Notre méthode de reconfiguration en utilisant une reconstruction quadratique par morceaux et un symétrique Flux de transport corrigés idées est directement applicable aux non structurées deux mailles de calcul dimensions avec la topologie maillée fixe. Limiteurs vectorielles en conservant une symétrie radiale des zones radiales sur mailles polaires sont décrits en détail dans le contexte de la reconstruction de limitation lors de l'étape de remappage de la méthode d'ALE. Symmetry et consolidés modifications préservant des limiteurs sont numériquement testés dans le code hydrodynamique quinconce PALE.

Des aspects particuliers de l'interaction laser de faible cibles en mousse de densité sont abordées dans la partie restante de la thèse. Simulations hydrodynamiques des matériaux cibles microstructurées nécessitent un traitement spécifique de l'absorption du laser et la réponse du matériau. La méthode d'une heure locale dépend coefficient d'absorption est généralisé pour être applicable dans le deux cylindrique dimensions codes hydrodynamiques symétriques, comme par exemple PALE. La généralisation comprend la mise en œuvre du rayon 3D - algorithme de traçage et un sous cyclée simulation de l'expansion des éléments de mousse solides induites par le laser et l'énergie des flux d'électrons. Ce nouveau modèle est testé dans les simulations numériques du laser - expériences d'interaction de mousse effectuées à l'PALS et GEKKO installations laser. Ces simulations montrent l'intérêt pratique du modèle et de la partie de l'application de cette thèse. Contrairement aux simulations hydrodynamiques classiques d'une mousse comme un matériau homogène, les résultats présentés ouvrent une nouvelle approche de la modélisation efficace des matériaux microstructurés. Ils montrent un bon accord de la vitesse du front d'ionisation dans la sous - mousse critique avec les expériences.

Les simulations numériques détaillées du laser généré plasmas sont hors de portée de cette thèse. Au lieu de cela, nous abordons les principaux éléments des méthodes numériques particulières requises pour effectuer des simulations plus efficaces et plus précises.

B.4. Résultats obtenus

La contribution principale et les nouvelles idées de la thèse peuvent se résumer à:

- Etude comparative des limiteurs de pente 1D pour une reconstruction par morceaux parabolique dans le contexte de remappage.
- Recherche et développement des limiteurs de pente pour les vecteurs et leur application dans l'étape de remappage de la méthode ALE.
- Développement d'une nouvelle symétrie–préservation remappage algorithme d'ordre eleve pour les équations d'Euler l'application de la préservation des limites sans les techniques de réparation artificiels.
- Développement et mise en œuvre des laser les méthodes d'absorption dans le code PALE hydrodynamique.
- Développement d'une nouvelle méthode numérique fiable pour la modélisation de l'interaction laser avec de faibles mousses de densité.

Ces résultats sont obtenus notamment dans le cadre des programmes du ministère de la Electronics physiques de l'Université technique tchèque de Prague de recherche et le Center for Lasers et Applications de l'Université de Bordeaux intenses. Ils contribuent au développement de numérique fiable méthodes de modélisation laser–plasma.

B.5. Des recherches supplémentaires

Dans la recherche future, la symmerty et lié haute préserver afin remappage méthode pourrait être étendue en 3D et aux mailles de calcul avec topologie changeante. Merci à la construction de la méthode, ces extensions sont plutôt simples. En particulier, l'application de la méthode de reconfiguration dans le ALE de reconnexion (ReALE) régime, a le potentiel d'améliorer la performance de ReALE.

Les limiteurs de pente pour les vecteurs sont largement appliquées dans non–linéaire méthodes hydrodynamiques ordre eleve. Les symmetry et limites décrites modifications de conservation des limiteurs peuvent trouver une application chaque fois que possible en dehors des méthodes de reconfiguration.

Le nouveau laser modèle d'absorption pour la basse mousses de densité peut être appliqué dans les études futures du laser lissage du faisceau et la modélisation hydrodynamique d'autres matériaux microstructurés. Cela ouvre une voie à de nouveaux modèles numériques plus efficaces pour l'avenir recherche ICF.